AN ABSTRACT OF THE DISSERTATION OF

John M. Lyman for the degree of Doctor of Philosophy in Oceanography presented on September 6, 2002.

Title: The Cross-Equatorial Structure of Tropical Instability Waves in Sea Surface Height.

Redacted for privacy

Abstract approved: _____ ᖳ

/ Dudley B. Chelton

A linearized model with two vertical modes has been developed to understand observed characteristics of monthly variability in the Equatorial Pacific from TOPEX/POSEIDON measurements of Sea Surface Height (SSH). The 2-mode model is obtained from an equatorial beta plane model that has been linearized about a geostrophically balanced mean flow with the state variables projected onto the first 2 baroclinic vertical eigenfunctions. Because in situ measurements of currents in the equatorial Pacific are not available with adequate spatial and temporal resolution, the mean current structure used in the 2-mode model was obtained from the Parallel Ocean Climate Model (POCM). POCM was chosen because the monthly variability in the model SSH fields closely resembles that of TOPEX/POSEIDON in dispersion characteristics and cross-equatorial structure. The sensitivity of the 2-mode projection model to the mean equatorial currents is examined by individually increasing and decreasing the various components of the equatorial current system. The eigenvectors and eigenvalues from this range of cur-

rent structures are able to reproduce many of the characteristics (phase, amplitude, period, wavenumber and meridional structure) observed in TOPEX/POSEIDON and POCM. The most surprising result is that the latitudinal structure of the eigenvector amplitudes south of the equator depends only on the strength of the northern equatorial current system.

The Cross-Equatorial Structure of Tropical Instability Waves in Sea Surface Height

by

John M. Lyman

A DISSERTATION

submitted to

Oregon State University

in partial fulfillment of
the requirements for the
degree of

Doctor of Philosophy

Completed September 6, 2002
Commencement June 2003

Doctor of Philosophy dissertation of John M. Lyman presented on September 6, 2002.

APPROVED:

Redacted for privacy

Major Professor, representing Oceanography

·Redacted for privacy

Dean of the College of Oceanic and Atmospheric Sciences

Redacted for privacy

Dean of the Graduate School

I understand that my dissertation will become part of the permanent collection of Oregon State University libraries. My signature below authorizes release of my dissertation to any reader upon request.

Redacted for privacy

John M. Lyman, Author

ACKNOWLEDGEMENTS

TABLE OF CONTENTS

LIST OF FIGURES

THE CROSS-EQUATORIAL STRUCTURE OF TROPICAL INSTABILITY WAVES IN SEA SURFACE HEIGHT

1 INTRODUCTION

The large-scale structure of Tropical Instability Waves (TIWs) in the Pacific was first characterized by *Legeckis* [1977] from a geostationary satellite measuring sea surface temperature (SST). Cusps in the northern equatorial front a few degrees north of the equator were observed with periods of about 25 days and wavelengths of about 1000 km. TIWs are now known to be a dominant feature in the Equatorial Pacific, influencing the dynamics and biology of the region. The predominately zonal currents, important to the El Niño/Southern Oscillation cycle, provide strong shears and density gradients which act as sources of energy for the TIWs [*Philander*, 1978; *Cox*, 1980; *Hansen and Paul*, 1984; *Luther and Johnson*, 1990; *McCreary and Yu*, 1992; *Proehl*, 1998; *Masina et al.*, 1999b]. Like the currents in the Pacific that spawn them, TIWs are seasonal, occurring primarily from June to February. As TIWs grow they become highly nonlinear [*Kennan and Flament*, 2000] obtaining significant amplitudes. The heat flux associated with these large perturbations are substantial, acting as an important contributor to the heat balance of the equatorial cold tongue [*Swenson and Hansen*, 1999]. TIW-induced perturbations of the SST front interact with the atmospheric boundary layer forming bands of wind stress curl and divergence north and south of the equator [*Chelton et al.*, 2001] that may in turn force the ocean. The fully developed TIWs also form regions of convergence and divergence, introducing nutrients

into the upper ocean, which in turn produce areas of high biological productivity that are evident in measurements of chlorophyll [*Foley et al.*, 1997; *Strutton et al.*, 2001] and zooplankton [*Flament et al.*, 1996] concentrations. These increases in biological activity increase CO_2 uptake that could contribute significantly to the equatorial Pacific carbon cycle [*Strutton et al.*, 2001].

The origins of TIWs have been investigated by examining linear models of the mean circulation in the equatorial Pacific. The simplest of these models, a 1 1/2 layer model [*Philander*, 1978], produced unstable solutions with a wavelength of 1000 km, period of 30 days and no appreciable amplitude in the south. These results were consistent with the observations of *Legeckis* [1977]. A more complicated model, a 2 1/2 layer beta plane model [*McCreary and Yu*, 1992] produced several unstable solutions. Two solutions were antisymmetric about the equator in pressure and one solution had a wavelength of 766km and a period of 22 days that was symmetric in pressure. Most recently, the linear stability of a 20-layer beta plane model was investigated by *Proehl* [1998]. The fastest growing solutions had wavelengths around 800-900 km, periods of about 30-35 days and were laregest within a few degrees north of the equator. The mean fields on which these studies were based included idealized currents derived from either under-sampled in situ estimates [*Philander*, 1978; *Proehl*, 1998] or from the mean flow in a nonlinear 2 1/2-layer model [*McCreary and Yu*, 1992].

A recent in-depth analysis of TOPEX sea surface height (SSH) data by *Chelton et al.* [2003] has revealed an asymmetric latitudinal structure in the amplitude of monthly variability in the equatorial pacific. Their observations can be characterized latitudinally by a SSH structure with approximately constant cross-equatorial

phase and a larger amplitude in the north. The signal has peak amplitudes in SSH at 5°N and 5°S and an approximate wavelength of 1600 km with a period of about 33 days. These characteristics are not shared by the solutions of the previous linear stability analysis (see section 2.2.2). In particular, the latitudinal structure or the dispersion characteristics of the past linear stability analyses are not consistent with these new observations from TOPEX. Either the eigenvector structure is non-existent south of the equator [*Legeckis*, 1977], the wavenumber or period are too small [*Legeckis*, 1977; *McCreary and Yu*, 1992; *Proehl*, 1998], or the maxima in the eigenvectors lie too close to the equator [*Proehl*, 1998].

Because in situ measurements of currents in the equatorial Pacific are not available with adequate spatial and temporal resolution, a mean current structure for investigation of the linear stability and latitudinal structure of the SSH signatures of TIWs was obtained from the Parallel Ocean Climate Model (POCM), which generates TIWs [*Semtner and Chervin*, 1992; *Stammer*, 1997; *McClean et al.*, 1997]. It will be shown in chapter 3 that POCM qualitatively reproduces the SSH features of TIWs that are observed in TOPEX.

The major goal of this study is to gain a better understanding of both the origins and characteristics of monthly variability of SSH in TOPEX and POCM. Rather than investigating a complicated multi-layer model as considered in *Proehl* [1998], the mean current structure of POCM is represented in this analysis by projecting the state variables onto the set of vertical baroclinic eigenfunctions, referred to here as the projection model (see chapter 4). This produces a set of equations that yield a representation of the background mean flow that is less subjective than the 1 1/2- or 2 1/2-layer models. Chapter 2 contains a background of observational and

modeling studies of TIWs. Chapter 3 shows the similarities between TOPEX and POCM SSH, examining in detail the vertical and meridional structure of TIWs in POCM that vary over the 60-day period investigated. Chapter 4 contains a detailed derivation of the one-mode projection model which is expanded to the n-mode projection model in appendix 7.1. The one- and two-mode projection models are then used to investigate the stability of the POCM mean currents at 134°W during a La Niña event in Chapter 5. The two-mode projection model is found to contain instabilities consistent with TIWs in POCM, while the one-mode projection model does not. In chapter 6, reasonable variations of the mean currents in the two-mode projection model can explain the spatial and temporal variability of the meridional structure in POCM. Chapter 7 investigates the different representations of critical layers in the one and two-mode projection models. It is shown that an increase in the maximum allowable phase speed from the one-mode to the two-mode projection model explains the ability of the two-mode projection model to reproduce TIWs.

2 BACKGROUND

An immense amount of literature exists concerning TIWs. Not only have TIWs been observed from satellite measurements of SST and SSH, but they have also been observed in situ from drifters, moorings, ships and planes [*Qiao and Weisberg*, 1995]. This chapter is an attempt to summarize their characteristics in the Pacific. Along with observations, a series of linear and nonlinear models of TIWs have attempted to describe the structure and energetics of TIWs [*Qiao and Weisberg*, 1995]. The first section gives an overview of observations of TIWs. The second section summarizes modeling studies of TIWs. The last section distills points concerning the structure and source of TIWs inferred from the observational and modeling studies.

2.1   Observations

2.1.1   Drifters

Hansen and Paul [1984] deployed 20 satellite-tracked ARGOS drifters in the summer of 1979 in a region from 125°W to 105°W and 10°S to 10°N. From these data, they were able to show that shear between the Equatorial Undercurrent (EUC) and the northern branch of the South Equatorial Current (SECN) was the major source of energy for the instabilities. However, there was also energy transfer from the shear between the North Equatorial Counter Current (NECC) and the SECN, along with a significant amount of baroclinic energy transfer. The amplitude and phase structure of the instabilities resembled the eigenvector structure in *Philander* [1978] (see section 2.2.2). Estimates of meridional heat flux from the drifters

showed that eddy heat flux was an important contributor to the heat balance in the region.

From 1980 to 1994, more than 1900 drifters were released in the equatorial Pacific [*Baturin and Niiler*, 1997]. By separating the data into two regions with dimensions of 20° in longitude by 20° in latitude centered on 0°N, 110°W and 0°N, 140°W and examining the meridional heat flux, momentum flux and energetics, *Baturin and Niiler* [1997] examined the life cycle of TIWs. The long time series allowed for the creation of an index of the amplitudes of TIWs which showed increased TIW activity during La Niña years and decreased TIW activity during El Niño years. Combining the drifter data with TOGA-TAO moorings and AVHRR SST, they found that eddy fluxes associated with TIWs reduce the meridional shear of the currents and warm the equatorial cold tongue. The maximum eddy fluxes occur in October and the maximum kinetic energy production occurs between the NECC and the SECN.

2.1.2 Moorings and Tide Gauges

Some of the earliest observations of monthly variability in the Pacific came from three near-bottom current meter moorings placed near the equator at 95°W [*Harvey and Patzert*, 1976] and were attributed to a first meridional (m=1), first baroclinic (n=1) mode Rossby wave. A period of 25 days and a wavelength of 1000 km were estimated from a two-month period that began near the end of February 1975.

Subsequently, the Pacific Equatorial Ocean Dynamics (PEQUOD) project placed six moorings between 148°W and 138°W within a degree of the equator from Jan-

uary 1981 to March 1983 [*Eriksen*, 1985; *Eriksen and Richman*, 1988]. Velocity measurements in the bottom 500 m to 3000 m were consistent with the dispersion characteristics of first baroclinic (n=1) Rossby-gravity (m=0) and Rossby (m=1) waves. These disturbances were narrow banded in zonal and vertical wavenumber for a given frequency. A combination of Rossby-gravity waves and Rossby (m=1) waves transported energy down and towards the east for periods shorter than 30 days while Rossby (m=1) waves alone transported energy down towards the west for periods longer than 45 days. For periods between 9 and 90 days, 72% of the energy flux was attributed to the Rossby (m=1) wave, and the remaining energy flux was ascribed to Rossby-gravity waves. The authors noted that the variability was consistent with remotely forced waves that originate at the surface.

Seven moorings that recorded velocity and temperature in the upper 250 m of the Pacific were deployed from May 1979 to October 1985 near the equator between 95°W to 152°W [*Halpern et al.*, 1988]. The velocity had spectral peaks at periods of 20 days near the surface. These peaks were attributed to n=1 Rossby-gravity waves that originated from instabilities in the equatorial current system. Beneath the thermocline, spectral peaks were found with periods of 30 days and longer. When a 2-year record from the mooring at 140°W was compared with a similar mooring on the equator in the Atlantic at 28°W, 20-day variability in the Pacific was found to be much more energetic [*Halpern and Weisberg*, 1989].

As a part of the Equatorial Pacific Ocean Climate Studies program (EPOCS), five inverted echo sounders were deployed from the equator to 9°N along 110°W for a 14-month period beginning in August 1980 [*Miller et al.*, 1985]. During the first nine months, there was a dominant spectral peak in dynamic height variability

with a period of 34 days. Monthly variability had a maximum amplitude at 5°N which appeared to be correlated with features in SST with 1000-km wavelengths but was not dependent on the presence of the Equatorial Front (EF). The northern structure of monthly dynamic height was consistent with eigenvectors with monthly periods that *Miller et al.* [1985] computed from the linearized model developed by *Philander* [1978] (see section 2.2.2).

Bryden and Brady [1989] computed eddy momentum and heat flux from six moorings that were centered on the equator at two different locations. Three of the moorings were deployed from April 1979 to June 1980 at 153°W as part of the North Pacific Experiment (NORPAX). The other three moorings were part of an EPOCS array centered on 110°W which recorded data from January 1979 to October 1981. The 20-day variability, also noted in *Halpern et al.* [1988], was found to transport heat poleward at all depths, while momentum was transported poleward above the core of the EUC and equatorward below the core of the EUC. The vertical integral of this eddy flux was equivalent to heating the equatorial cold tongue at a rate of 245 Wm^{-2}.

Using tide gauges from the Pacific Sea Level Network established by *Wyrtki* [1979], two 730-day time series were constructed for 1979-1980 and 1982-1983. Examining the spectra from five latitudinal bands, a peak in variability in the 25- to 50-day band was noted north of the equator with a weaker signal south of the equator [*Mitchum and Lukas*, 1987]. This was interpreted as TIWs originating as shear instabilities.

Five moorings centered on 140°W near the equator as part of the Tropical Instability Wave Experiment (TIWE) were deployed from May 12, 1990 to June 18,

1991. These moorings, which measured currents in the upper 250 m, showed TIW wave energy that was primarily confined above the core of the EUC. The data indicated that the 1990-1991 TIW season starts in August and ends in December. This TIW season was found to be consistent with seasonal variation in accelerations of the SEC [*Qiao and Weisberg*, 1995]. Examination of perturbation energy equations led to the conclusion that the observed TIWs originated from the shear between the EUC and the SEC [*Qiao and Weisberg*, 1998].

The Tropical Atmosphere Ocean (TAO, recently known as TAO/TRITON) array presently consists of 70 moorings spanning the equatorial Pacific from 95°W to 137°E and from 12°N to 8°S. All of these moorings measure winds, SST, relative humidity, air temperature, and subsurface temperatures to a depth of 500 m. Additionally, five of the moorings along the equator measure subsurface velocity. Implementation of the TAO array began in early 1984 but was not fully completed until Dec 1994. In 1988-1989, monthly variability was observed at six moorings between 2°S to 9°N along 140°W. The moorings at 0°,140°W and 7°N,140°W also measured monthly variability in velocity. *McPhaden* [1996] characterized the variability as being in geostrophic balance with sea level, having periods between 15-50 days, estimated wavelengths between 750-1150 km and originating most likely from instabilities in the shear between the SEC and the NECC. The maximum temperature variance occurred in the thermocline between 5°N and 7°N while maxima in the SST variance occurred between 2°N and 5°N [*McPhaden*, 1996]. Current meters on the mooring at 0°,170°W also showed evidence of TIWs in 1988 [*Weisberg and Hayes*, 1995].

2.1.3   Ships & Aircraft

In preparation for NORPAX, Airborne Expendable Bathythermographs (AXBTs) were dropped from a P-3 aircraft that was flown weekly between 20°N to 17°S along 150°W and 158°W for 3 months starting in November 1977 [*Barnett and Patzert*, 1980]. Highly coherent structures in temperature with time scales of 2-3 months and spatial scales of 2000 km were found in AXBT data within 10° of the equator. Subsequently, NORPAX moorings were placed at 0°,152°W; 0°40′N,153°W and 0°40′S,153°W and monthly shipboard ADCP and CTD measurements were made from February 1979 to June 1980 along a section from Hawaii to Tahiti during the NORPAX Hawaii-Tahiti Shuttle experiment [*Wyrtki et al.*, 1981].

Initial analysis of NORPAX data within 75km of the equator found energetic variability in the 19-31 day band that was attributed to barotropic instabilities that originated from the shear between the SECN and the EUC [*Lukas*, 1987]. A more extensive analysis of the NORPAX ADCP and CTD sections from 10°N to 4°S showed three distinct regions of instability [*Luther and Johnson*, 1990]. The first region occurred between the EUC and the SECN where mean kinetic energy was converted to eddy kinetic energy. The second region was at the EF where the mean potential energy was converted to eddy potential energy. The last region existed at the thermocline near the NECC where mean kinetic energy was converted to eddy potential energy. It was also found that when neglecting vertical stresses the zonal momentum equation was balanced at 90m, with geostrophy dominating north of 5°N [*Johnson and Luther*, 1994].

Four cruises were conducted during April, June, October and November of 1984 extending as far west 170°W and to 85°W in the east. From 140°W to 85°W the

cruise tracks are along the equator, only occasionally venturing a few degrees north and south of the equator. West of 140°W, the cruise tracks extended as far north as Hawaii and as far south as Tahiti [*Wilson and Leetmaa*, 1988]. Although this sampling pattern was not ideal for characterizing the scales of TIWs, a dominant band of variability with a wavelength of approximately 1000km and a period of about 30 days was identified. Barotropic instability originating from the northern edge of the EUC was found to be an order of magnitude larger than baroclinic energy conversion in the region. It was hypothesized that the onset of TIWs is due to an increase in the transport of the EUC [*Wilson and Leetmaa*, 1988].

A large-scale survey was conducted in November of 1990 that involved ship CTD surveys with a towed platform (SeaSoar), ship-mounted ADCP sections, ARGOS-tracked drifters, TAO moorings, and infrared satellite images of SST [*Flament et al.*, 1996; *Kennan and Flament*, 2000]. The rich array of data allowed for a three dimensional picture of what the authors describe as a vortex with a 500 km diameter. The survey was constrained between 1°S and 7°N and showed a highly nonlinear vortex traveling between the shear of the NECC and SECN at .3 $\frac{m}{sec}$. This vortex affected the meridional transport of heat, salt and momentum. Upwelling on the leading edge of the vortex, due to conservation of potential vorticity caused the introduction of nutrients to the region and was associated with an order of magnitude increase in zooplankton concentrations [*Flament et al.*, 1996]. Latitudinal variation in phase speed suggested a different mechanism acting between the EUC and SECN than between the NECC and the SECN.

2.1.4 Satellites

2.1.4.1 Sea Surface Temperature

TIW signals in Sea Surface Temperature (SST) have been observed from passive measurements of infrared and microwave radiation. The defining description of the northern hemisphere signature of TIWs in the equatorial Pacific was made by Legeckis from infrared measurements from a geostationary satellite [*Legeckis*, 1977; *Legeckis et al.*, 1983]. From cloud-free days spanning the period from 1975 to 1981, crests in the EF, which lies $1° − 3°$ north of the equator, were characterized as having a period of about 25 days and a wavelength of approximately 1000 km.

The Advanced Very High Resolution Radiometer (AVHRR) on the polar orbiting NOAA-6 and NOAA-7a satellites captured the zonal structure of TIWs on cloud-free days. From June to July 1981, TIWs in SST were observed to extend from 93°W to 125°W with an approximate period of 25 days and a wavelength of about 1000 km [*Pullen et al.*, 1987]. From August 1983 to February 1984, the waves were observed to extend from 90°W to 160°W with periods ranging from 14 to 43 days and wavelengths of 600-1400 km [*Legeckis*, 1986]. The locations of the cusps in SST during 1981 are coincident with the shear between the NECC and the SECN [*Pullen et al.*, 1987].

The Tropical Rainfall Measuring Mission (TRMM) Microwave Imager (TMI) has been measuring SST in all-weather conditions since December 1997. Records from 1998 to 1999 show cusped patterns in the SST fronts both north and south of the equator extending from near the eastern boundary to 160°E [*Chelton et al.*, 2000]. These northern and southern hemisphere signatures of TIWs propagate

westward with a phase speed of .5 $\frac{m}{s}$, both north and south of the equator. The displacements were 50% larger in the north than in the south and suggested an antisymmetric structure in SST.

An optimum interpolated data product, referred to as Reynolds SST, combines ship, buoy and satellite SST to provide a global estimates of SST from 1982-1993 [*Reynolds and Smith*, 1994]. Although sharp features of TIWs are smoothed out, the long Reynolds SST record allows examination of their interannual variability. Typically, TIWs have been observed to travel westward with a phase velocity of 0.5 $\frac{m}{sec}$ between 160°W and 100°W from July to the end of the year [*Contreras*, 2001]. However, the waves have occasionally persisted for multiple years with a variable westward extent.

2.1.4.2 Wind Stress

Estimates of surface wind divergence from the Earth Remote Sensing (ERS-1) scatterometer were shown by *Xie et al.* [1998] to be significantly correlated with TIW induced SST signatures from AVHRR data set prepared at the Jet Propulsion Lab during the 27 week period beginning on June 19 1993. *Xie et al.* [1998] used an atmospheric general circulation model to show that the TIW-perturbations seen in the surface wind divergence can penetrate well above the atmospheric boundary layer.

Wind stress estimates from QuikSCAT during the strong La Niña of 1999 were observed to propagate westward with the SST signal from TMI at 0.6 $\frac{m}{s}$, both north and south of the equator [*Chelton et al.*, 2001]. During August and September of 1998 phase speeds south of the equator abruptly slowed to 0.25 $\frac{m}{s}$. Signals in

column-integrated water vapor, cloud liquid water and precipitation from TMI are also observed to travel westward with SST [*Hashizume et al.*, 2001]. The curl of the wind stress was found to be in proportion to the crosswind component of SST gradient, while the divergence of the wind stress is proportional to the downwind component of the SST gradient [*Chelton et al.*, 2001]. These correlations, along with phase lags seen between SST and vector winds [*Liu et al.*, 2000], support the negative feedback system between SST and wind proposed by *Hayes et al.* [1989]. The effect of SST on wind stress causes a narrow zonal band of wind stress curl to form north of the equator [*Chelton et al.*, 2001] that is thought to be important to the development of the SECN [*Kessler*, 2001].

2.1.4.3 Sea Surface Height

TIWs have been observed in sea surface height (SSH) measured by three different satellite altimeters; Seasat, Geosat and TOPEX/Poseidon (T/P). The first of these missions, Seasat, had a 3-day exact repeat orbit that lasted from September 15 to October 10, 1978. The 500 km spacing of ascending and descending ground tracks at 5°N could just detect 1000-2000 km wavelength TIWs [*Malardé et al.*, 1987; *Musman*, 1989]. SSH anomalies 600 km in diameter with 15-20 cm amplitude were seen traveling westward at 0.46 $\frac{m}{s}$ along 5°N. A less coherent TIW signal was also evident along 5°S which displayed a significant degree of symmetry with the signal in the north [*Malardé et al.*, 1987].

The Geosat altimeter mission lasted from November 15, 1986 to January15, 1989. The ground tracks from Geosat were 160 km apart at 5° and were much better suited to detect the spatial structure of TIWs. However, the 17-day exact repeat period of Geosat was barely adequate to sample the 20-40 day period of

the TIWs. Mapping Geosat data onto a 1° by 10-day grid, *Périgaud* [1990] found 1000-2200 km waves traveling westward at 0.4 $\frac{m}{s}$. A maximum amplitude of 8 cm occurred around 5°N. Low correlations over the 26 month record between a SSH signal filtered to retain TIWs at 5°S and 5°N along 150°E to 90°W, led to the conclusion that the anomalies were not equatorial trapped waves. During the 2-year record, TIWs were strongest from December to January and weakest from April to May.

Several studies have shown that T/P is suited for the investigation of TIWs. *Menkes et al.* [1996] validated T/P measurements in the equatorial pacific for periods longer than 35 days by comparing T/P with dynamic heights computed from TAO buoys [*Menkes et al.*, 1996]. Similarly, *Carton et al.* [1996], while looking at the importance of different data products in a data assimilation of the equatorial Pacific, noted that T/P was well suited to observing TIWs.

A recent analysis of 9 years of T/P data record starting in 1993 described the latitudinal and temporal characteristics of TIWs [*Chelton et al.*, 2003]. The spatial and temporal resolution problems of Seasat and Geosat altimeter missions are greatly reduced by the 9.9 day exact-repeat orbit and the 2.8° longitudinal spacing of ascending and descending ground tracks of the T/P sampling pattern. Zonally banded maxima in monthly variability were identified 5° north and south of the equator. The amplitudes north of the equator were 2-3 times larger than those in the south. Northern and southern structures were predominant in phase, but could vary as much as 90° or more. *Lawrence and Angell* [2000] hypothesized that a Rossby wave is present when TIWs are in phase north and south of the equator. *Chelton et al.* [2003] estimated the phase speed of the signal to be 0.55

$\frac{m}{s}$ westward with a wavelength between 1600 and 1700 km and a period around 34 days. The energy of the signal appeared to propagate to the west with a group velocity of 0.15 $\frac{m}{s}$. The variability was most energetic in the boreal fall/winter and weakest in spring.

2.2 Models

2.2.1 Nonlinear Models of TIWs

Efforts to understand the time evolution, spatial structure and energetics of fully developed TIWs have led to the development of non-linear models of the equatorial Pacific. Investigating the circulation of the equatorial Pacific, *Semtner and Holland* [1980] found waves with 33 and 44 day periods in a 14-level channel model with constant wind forcing. The 33-day signal propagated westward with a wavelength of 800 km and had a meridional and vertical structure that was similar to a n=1 vertical mode, m=1 meridional mode equatorially trapped Rossby wave, i.e. symmetrical in SSH. Unlike the 33-day signal, the 44-day wave was antisymmetric in SSH, resembling an m=2 meridional mode equatorially trapped Rossby wave. These waves were reportedly maintained by baroclinic instabilities on both sides of the equator.

TIWs with 1000 km wavelengths and 30-day periods were found north of the equator in the eastern and central Pacific by *Cox* [1980] in a 14-level model with bottom topography and coastlines that was driven by a seasonal cycle of the monthly wind stress. A flat bottom version of the model with no coastlines and a specified mean flow was used to explore the origins of the TIWs. It was found

that the main source of TIWs was barotropic instabilities from the shear between the SECN and the NECC, although baroclinic conversions were also present. *Cox* [1980] showed that vertical mode 1 Rossby-gravity waves and m=1 meridional mode Rossby waves can transport the TIW energy eastward and into the deep ocean. The dominant waves in the model were m=1 Rossby waves which transported energy mostly downward into the deep ocean. Sensitivity of both growth rate and period was observed when the strength of the SEC was altered [*Seigel*, 1985]. Increases in the SEC led to shorter periods and faster growth rates.

The seasonal cycle of the tropical Pacific and Atlantic was explored by *Philander et al.* [1986] from a 27-level general circulation model. The majority of the TIW signal occurred during boreal fall/winter between 3°S-5°N. Characterized by a period of 30-days and wavelength of 1000 km, the TIWs varied somewhat in time and longitude. The upwelling in the troughs and downwelling in the crests of the TIWs was significant, reaching the same magnitude as the mean vertical velocity. The presence of monthly variability in the deep ocean was attributed to Rossby-gravity waves that were spawned by surface trapped instabilities.

Nonlinear 2 1/2 layer models have been used to examine the stability of the equatorial Pacific [*Schopf and Cane*, 1983; *McCreary and Yu*, 1992; *Donohue and Wimbush*, 1998]. The simple physics in a 2 1/2-layer model allows for more straightforward analyses of TIW structure and dynamics. *Schopf and Cane* [1983] applied a uniform wind stress and found symmetric instabilities in pressure centered between 5°-4° north and south of the equator with wavelengths of 800 km.

McCreary and Yu [1992] added a longitudinally variable wind stress and an upper layer that could entrain and detrain water. The model developed three

types of instabilities, two antisymmetric and one symmetric in pressure. One of the antisymmetric disturbances was surface trapped with a period of 21 days, while the other instability was in the lower layer and had a period between 35-53 days. The symmetric disturbance had a period of 28-days and resembled an n=1, m=1 Rossby wave. The ability of the upper layer to alter its density enabled what the authors referred to as frontal instability, which was found to be important to the existence of TIWs. Sources of the instabilities also included barotropic and Kelvin Helmholtz instabilities, while traditional baroclinic instabilities acted as an energy sink.

Zheng et al. [1994] devised an analytical model to investigate the effects of the SEC and the NECC on the dispersion characteristics of first meridional mode Rossby Waves. The current system was modeled by a hyperbolic function that was symmetric about the equator. Their analytical model was able to reproduce eastward and stationary phase propagation observed in 25-day variability of SST in the equatorial Pacific from an Advanced Very High Resolution Radiometer.

Although the upper layer could not entrain water, the model described by *Donohue and Wimbush* [1998] was forced by a more realistic longitudinally and latitudinally variable mean monthly wind stress climatology. Two instabilities were found: one asymmetric in pressure with a maximum at 6°N and a slight peak near 5°S, a period of 30 days, and a wavelength of 1100 km; the other instability had SSH maxima near 1.5°N and 1.5°S, a period of 15 days and a wavelength of 1100 km. Two sources of these instabilities were identified: one on the equatorward side of the SECN, which was primarily barotropic, and another weaker source on the poleward flank of the SECN that was both baroclinic and barotropic.

It has been suggested that the winds are important in determining the temporal phase of TIWs [*Allen et al.*, 1995; *Lawrence et al.*, 1998; *Vialard et al.*, 2001]. The temporal phase of TIWs in a multi-level primitive equation model forced by ECMWF winds were found to be correlated with observations of TIWs in SST from TAO and Along Track Scanning Radiometer (ATSR) satellite infrared measurements of SST. Altering the winds by removing the intraseasonal cycle reduced the correlation between the model and the observations [*Allen et al.*, 1995; *Lawrence et al.*, 1998]. They suggest that this is an indication that TIWs are phase locked with the winds. *Vialard et al.* [2001] went on to show that this phase locking was also dependent on the magnitude and type of wind product used, but was not sensitive to the initial conditions applied to the model. This further implicates the importance of winds in determining the characteristics of TIWs.

Assimilation of TAO, T/P altimeter and XBT data into a 20-level Modular Ocean Model 2 (MOM2) forced by weekly averaged NCEP winds produced TIWs with realistic temporal variability and phase [*Carton et al.*, 1996; *Seidel and Giese*, 1999]. At 110°W, the TIWs were identified as both a 19-day surface-trapped signal and a 29-day signal that peaked at depth with increasing amplitude towards the west [*Seidel and Giese*, 1999].

A detailed look at the structure and energetics of TIWs in a general circulation model is given in *Masina et al.* [1999a, b]. Forcing MOM with winds representing strong La Niña conditions, TIWs were found to develop in the eastern and central Pacific. In the eastern Pacific, there were two regions of instability: a baroclinic instability between 2°N and 6°N along the north equatorial front, which is the primary triggering mechanism for the TIWs, and a barotropic instability in the

shear between the EUC and the SECN, which is triggered when energy from the baroclinic instability radiates equatorward. In the central Pacific, the sources of energy were much the same: a baroclinic instability in the south equatorial front and a barotropic instability in the shears between the EUC and both branches of the SEC. Wavelet analysis of the variability showed that TIWs had a complicated structure in period and wavelength, which varies in time, latitude, longitude and depth. The TIW variability at 140°W, 2°N in the model had a period of 21 days and a wavelength of 800 km at the surface, while below the thermocline, the period was 42 days and the wavelength was 1200 km. In the eastern Pacific, the two instabilities north and south of the equator were phase locked, producing a signal that propagated westward at approximately 0.5 $\frac{m}{s}$. In the central Pacific, the westward phase speed south of the equator slowed to 0.1 $\frac{m}{s}$, a characteristic not previously attributed to TIWs. There is also evidence of westward traveling m=1, n=1 Rossby waves and n=1 Rossby-gravity waves in the model below the thermocline.

TIWs have also been found in the Parallel Ocean Climate Model (POCM), a 20-level global ocean circulation model driven by ECMWF winds and containing realistic bathymetry and coastlines [*Semtner and Chervin*, 1992; *Stammer*, 1997; *McClean et al.*, 1997]. The TIWs produced in the POCM model are similar to those that have been observed. TIW patterns of divergence and relative vorticity in POCM are remarkably similar to in situ observations [*Kennan and Flament*, 2000]. The mean phase speeds of TIWs from T/P data, computed over a five year record, also agreed with POCM [*Weidman et al.*, 1999]. Additionally *Weidman et al.* [1999] found to first order that phase difference in POCM TIW SSH and

SST corresponded to the geostrophically balanced cat's eye stream-line pattern suggested from *Musman* [1989], i.e. the phase difference between SSH and SST varied continuously from 0° to 180° as latitude increased to the north with SSH leading SST.

2.2.2 Linear Models of TIWs

Linear models of mean ocean conditions give insight into the origins of TIWs that cannot be easily deduced from the fully non-linear solutions. The general characteristics of the observations of TIWs in SST north of the equator with a period of 25 days and a wavelength of 1000 km [*Legeckis*, 1977; *Legeckis et al.*, 1983] were reproduced by *Philander* [1978] in a 1 1/2 layer model linearized about an idealized version of the equatorial current system consisting of a broad SEC, which was not split by the EUC, and a NECC centered on 5°N. The eigenvectors corresponding to the fastest growing modes were restricted in amplitude to the region north of the equator, and had a wavelength of 1000 km and a period of 30 days. These solutions were barotropically unstable, obtaining energy from the meridional shear between the SECN and NECC.

The effects of weakly latitudinally varying background mean currents on equatorial trapped Rossby waves have been examined by *Chang and Philander* [1989]. By implementing the WKB approximation in a 1.5-layer model and examining the resulting ray paths, they found that eastward flow enhances meridional group velocity, while westward flow retards it. Therefore, the EUC and the NECC have the effect of decreasing the phase speeds of equatorial trapped waves, while the SECN and SECS increase the phase speeds of the same waves.

Proehl [1990] revisited the topic looking at the effects of strong shear between the eastward EUC and westward SEC on the structure and propagation of low meridional mode Rossby waves. The EUC and SEC were represented by equatorially symmetric Gaussian velocity profiles. He found that eastward flows had a tendency to expand the meridional structure of the pressure field and increase the rate of vertical energy propagation. The existence of critical layers in westward flows did not prevent the establishment of vertical modes. When the combined system of the SEC and the EUC was examined, *Proehl* [1990] found that, near the equator, the system was 'opaque'to vertical modes higher than mode one, suggesting a dominance of the first baroclinic mode in equatorial regions.

Investigating the origins of TIWs in their 2 1/2 layer non-linear model, *McCreary and Yu* [1992] also looked at a version of their model that was linearized about the mean current structure from the full model. The linearized model was able to reproduce the two antisymmetric modes in pressure but was unable to represent the symmetric mode accurately, producing symmetric solutions with periods of 22 days and 766 km wavelengths.

A more detailed look at the energetics in the 2 1/2 layer linearized model was given by *Yu et al.* [1995] in an attempt to understand why TIWs are largest north of the equator. By altering an idealized mean current structure, they showed that the two antisymmetric modes are affected by cross-equatorial asymmetries in the SEC and the equatorial SST fronts, while the existence of the NECC had little or no effect on the symmetry of the solutions. Reductions in the southern branch of the SEC (SECS) and the south equatorial front led to unstable solutions with the largest amplitude north of the equator. These solutions had smaller growth rates

and similar dispersion characteristics as those from a symmetric background state. The energy sources for the TIWs were both frontal and barotropic instabilities.

Expanding the vertical resolution of previous linear stability analysis, *Proehl* [1998] looked at the effect of asymmetries in the background flow on the stability of a 20-layer equatorial beta plane model. Although the shears on both sides of the SECN were found to be potentially unstable, the barotropic instabilities on the southern side of the SECN were the primary energy source for the TIWs. A physical description was presented in terms of what *Proehl* [1998] refers to as wave over reflection, which was able to explain the origins of the TIWs by the location of critical layers and surfaces of zero potential vorticity gradients. The most unstable solution from *Proehl* [1998] had maximum amplitudes within a few degrees of the equator, periods between 30-35 days and wavelengths around 800-900 km.

2.3 Summary

Finite amplitude TIWs have complicated origins. It is clear from modeling and observations that barotropic, baroclinic and frontal instabilities are possible sources of energy. However, there is not a consensus concerning which sources dominate: barotropic instabilities from the shear between the SECN and the EUC [*Hansen and Paul*, 1984; *Lukas*, 1987; *Luther and Johnson*, 1990; *Qiao and Weisberg*, 1995; *Donohue and Wimbush*, 1998; *Proehl*, 1998], barotropic instability in the shear between the SECN and the NECC [*Philander*, 1978; *Cox*, 1980; *McPhaden*, 1996; *Baturin and Niiler*, 1997], baroclinic instabilities [*Semtner and Holland*, 1980; *Masina et al.*, 1999b] or frontal instability in the north equatorial front [*McCreary and Yu*, 1992]. The NECC has been found to have little effect on TIWs in some

models [*Yu et al.*, 1995; *Masina et al.*, 1999b], while instabilities from the shear between the NECC and the SECN are an important feature in observations [*Hansen and Paul*, 1984; *Luther and Johnson*, 1990; *McPhaden*, 1996; *Baturin and Niiler*, 1997]. Regardless of which form of energy transfer is dominant, the story is further complicated by modeling and observational evidence of the existence of more than one type of source [*Cox*, 1980; *Luther and Johnson*, 1990; *Masina et al.*, 1999b].

There also appears to be at least two sets of TIW characteristics [*Kennan and Flament*, 2000]. One instability is surface trapped near the EUC and the SECN, with wavelengths around 700-1100 km and periods between 15-25 days [*Legeckis*, 1977, 1986; *Halpern et al.*, 1988; *Pullen et al.*, 1987; *Miller et al.*, 1985; *McCreary and Yu*, 1992; *McPhaden*, 1996; *Masina et al.*, 1999a; *Contreras*, 2001]. These instabilities have equatorially antisymmetric structure in pressure and are manifested as meanders in the north and south equatorial SST fronts [*McCreary and Yu*, 1992; *Proehl*, 1998; *Masina et al.*, 1999a; *Seidel and Giese*, 1999; *Chelton et al.*, 2000]. The other instability near the base of the thermocline between the SECN and the NECC has a longer wavelength (1000-1600 km) and a longer period (28-40 days) [*Miller et al.*, 1985; *McCreary and Yu*, 1992; *McPhaden*, 1996; *Donohue and Wimbush*, 1998; *Kennan and Flament*, 2000; *Masina et al.*, 1999a; *Seidel and Giese*, 1999; *Chelton et al.*, 2003]. The structure is asymmetric in pressure and resembles signals seen in SSH [*Miller et al.*, 1985; *Malardé et al.*, 1987; *Périgaud*, 1990; *McCreary and Yu*, 1992; *Donohue and Wimbush*, 1998; *Chelton et al.*, 2003]. Both of these instabilities are thought to spawn n=1, m=0 antisymmetric [*Cox*, 1980; *Miller et al.*, 1985; *Halpern et al.*, 1988; *Eriksen*, 1985; *Eriksen and Richman*, 1988; *Philander et al.*, 1986; *Masina et al.*, 1999a], n=1, m=1 symmetric

[*Cox*, 1980; *Miller et al.*, 1985; *Halpern et al.*, 1988; *Eriksen*, 1985; *Eriksen and Richman*, 1988; *McCreary and Yu*, 1992; *Masina et al.*, 1999a] and n=1, m=2 antisymmetric [*Semtner and Holland*, 1980] equatorially trapped Rossby waves.

The cross-equatorial structures of the amplitude and phase of TIWs have not been widely discussed. Disturbances south of the equator have been observed with similar characteristics to northern instabilities [*Barnett and Patzert*, 1980; *Malardé et al.*, 1987] but have only been mentioned in passing. Linear modeling surveys of TIWs has concentrated on why the signals were larger in the north, rather than describing characteristics of southern variability [*Philander*, 1978; *Yu et al.*, 1995; *Proehl*, 1998]. With regard to TIWs observed in SSH, there is now a detailed description of the cross-equatorial structure from 9 years of T/P altimeter data. Amplitudes are 3 times larger in the north than the south with spatially and temporally varying phase difference north and south of the equator. Linear modeling studies have not successfully reproduced these features. The linear stability analysis in this study of mean current structure from POCM reproduces the cross equatorial structure in amplitude and phase of TIWs observed in T/P altimeter data and POCM SSH model output.

3 POCM: MONTHLY VARIABILITY IN THE TROPICAL PACIFIC

TIWs are among the most energetic features in TOPEX altimeter observations of SSH. The vertical structure of the TIW-induced perturbations, as well as the slowly-varying background mean conditions, are only sparsely observed (as discussed in chapter 2). To circumvent the issue of data availability, TIWs are investigated here from the Parallel Ocean Climate Model (POCM). To the extent that POCM is capable of reproducing TIWs, the dynamics of TIWs inferred from the model provide insight into the dynamics of TIWs in the real ocean.

In this chapter, the characteristics of the SSH signatures of TIWs in POCM are first compared to TOPEX observations. While there are differences between modeled and observed TIWs, the salient features are sufficiently similar to justify a detailed analysis of the POCM model output.

3.1 Comparisons Between POCM and TOPEX

The existence of monthly variability in POCM has previously been noted in several studies [*Semtner and Chervin*, 1992; *Stammer*, 1997; *McClean et al.*, 1997; *Kennan and Flament*, 2000; *Weidman et al.*, 1999]. In particular, *Kennan and Flament* [2000] compared the vertical structure of a TIW from POCM with in situ observations of what they referred to as an individual vortex in the westward propagating TIW wave train and found that the distributions of the modeled and observed divergence and relative vorticity fields were in agreement. This suggests that the dynamics of monthly variability can be investigated from the POCM simulation. In this section, additional evidence is provided justifying the use of POCM to investigate TIWs in the tropical Pacific.
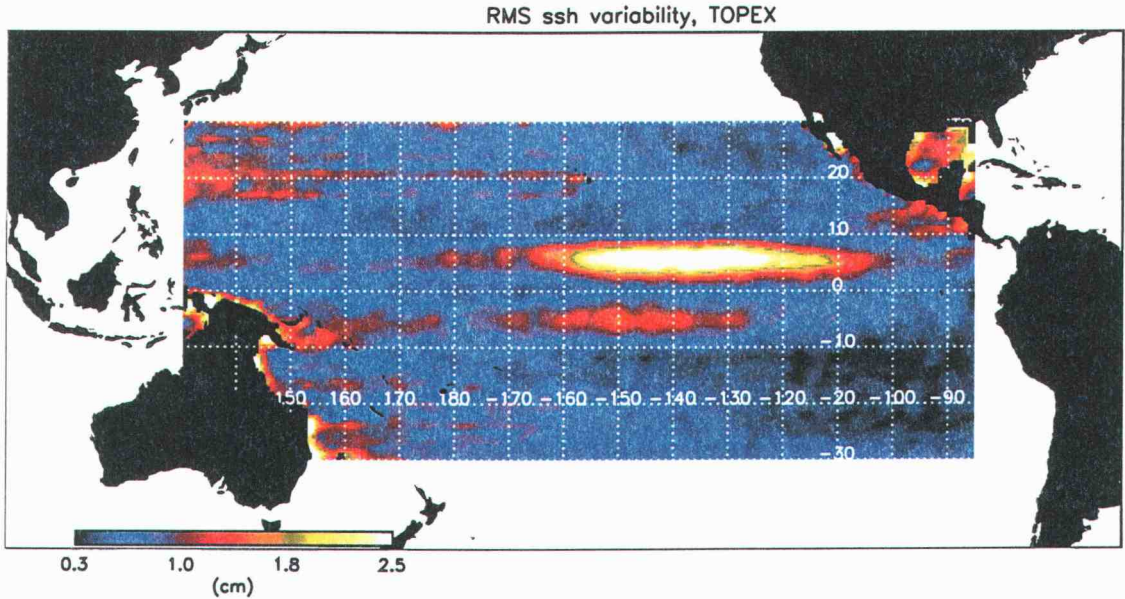
Figure 3.1: The standard deviation of SSH from TOPEX filtered to retain periods between 25 and 60 days. The standard deviation was computed over a 5-year record beginning in November 1992 and ending October 1997.

In a recent study, *Chelton et al.* [2003] investigated monthly variability of SSH in the tropical Pacific from 10 years of TOPEX altimeter data. Using complex empirical orthogonal functions (CEOFs), they depicted the variability as a westward propagating, latitudinally asymmetric wave with larger amplitudes north of the equator. This asymmetry can be seen in the standard deviation of SSH measurements from TOPEX (Fig. 3.1) that have been filtered to retain periods between 25 and 60 days. Two bands of high SSH variability straddle the equator at 5°N and 5°S. The band at 5°N is much more energetic and extends from about 100°W to about 170°E. The less energetic band in the south extends from 125°W to the dateline.
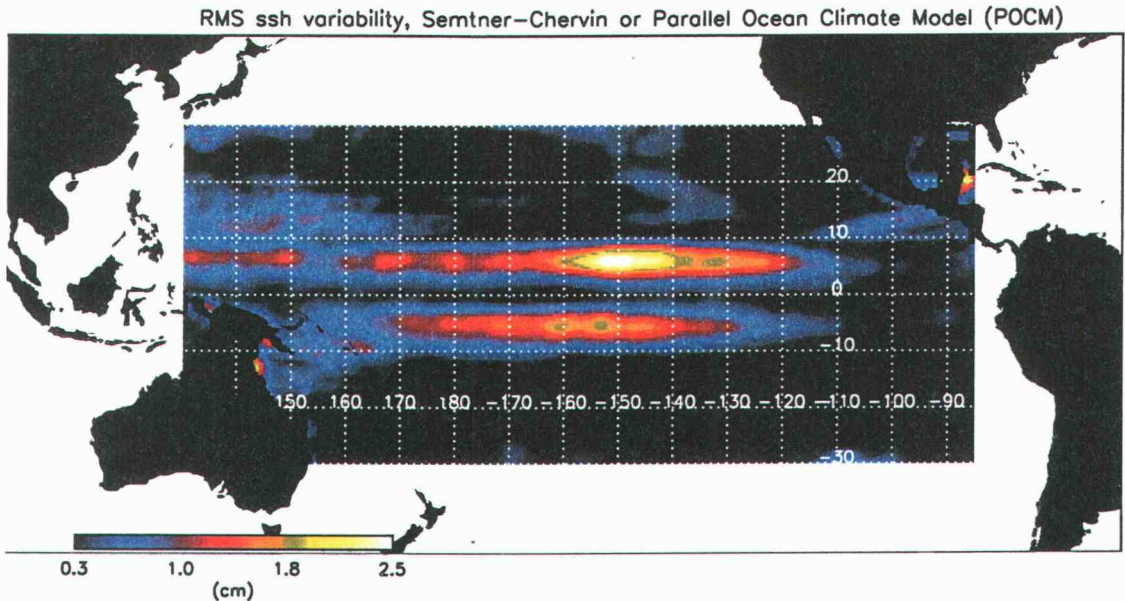
Figure 3.2: The standard deviation of SSH from POCM filtered to retain periods between 25 and 60 days, computed over the same 5-year period as Fig. 3.1.

Monthly variability of SSH in POCM is qualitatively similar to that observed in the TOPEX data. Like TOPEX, there are two bands of high variability along 5°N and 5°S in the standard deviation of filtered POCM SSH (Fig. 3.2), with larger amplitudes north of the equator. In addition, time-longitude plots of 5 years of filtered SSH along 5°N for TOPEX and POCM (Fig. 3.3) show similar annual and interannual variability in the amplitudes of the TIW signals. The SSH signals in both TOPEX and POCM are weak to non-existent during the 1997 El Niño and strong during the 1995-1996 La Niña. Over the period of the data record shown in Fig. 3.3, the TIWs have very similar amplitudes and longitudinal structure along 5°N in both TOPEX and POCM.

While the characteristics of TIWs are similar in TOPEX and POCM, there are quantitative differences. Spectral estimates from time-longitude plots of TOPEX
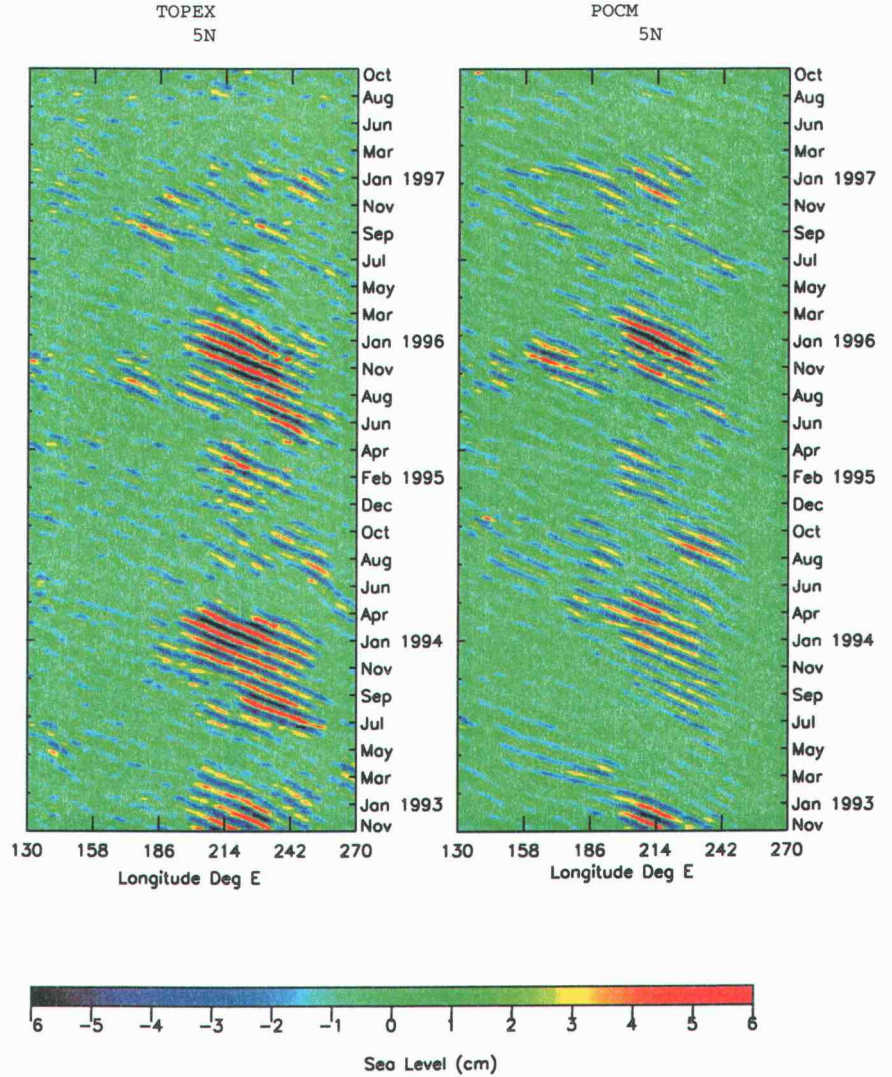
Figure 3.3: Time-longitude plots along 5°N of SSH filtered to retain periods between 25 and 60 days for TOPEX (left) and POCM (right).

variability (the left panel in Fig. 3.3) yield a period and wavelength of the TIWs to be about 33 ± 2 days and 1650 ± 150 km respectively. However, spectral estimates from the time-longitude plot of POCM variability (the right panel in Fig. 3.3) yield a shorter period of 28 ± 2 days and a shorter wavelength of 1350 ± 150 km. In both cases, the uncertainties in the period and wavelength estimates are derived from the Fourier Frequency and wavenumbers intervals based on the duration of a TIW season. In addition to these differences in the dispersion characteristics, the longitudinal extents of the variability differ between TOPEX and POCM. In POCM, the variability extends beyond the dateline to 170°E in the south and extends all the way to the western boundary in the north. In the east, the POCM variability does not appear until 120°W in the north and 130°W in the south (Fig. 3.2).

The degree of asymmetry about the equator also differs between TOPEX and POCM. In the TOPEX data, the TIW standard deviation north of the equator is up to a 1.4 times larger than in POCM (Figs. 3.1 and 3.2), while the TIW variance south of the equator is up to a factor of 1.5 times larger in POCM than in TOPEX. The equatorial asymmetry therefore is larger in TOPEX than in POCM.

The differences between the POCM simulations and TOPEX observations of monthly variability are quite likely indicative, at least in part, of a misrepresentation of the slowly varying background mean velocity fields in POCM. However, to the extent that equatorial dynamics are adequately represented in POCM, the model output can be analyzed to investigate the effects of the mean tropical Pacific currents of the TIWs in the model. While the effects of mean flow in POCM cannot

be expected to quantitatively explain the TOPEX observations, the dynamics of TIWs in POCM should provide insight into the dynamics of the observed TIWs.

The version of the POCM analyzed here is run 4C. It is a $1/4°$ resolution, 20-level model, forced by 3-day European Centre for Medium-Range Weather Forecasts (ECMWF) renanalysis winds and updated every 30 minutes (R. Tokmakian, personal communication, 1999). The fields used in this analysis were averaged over 3 days. For more details on POCM, see *Semtner and Chervin* [1992] or http://vislab-www.nps.navy.mil.

3.2   The Vertical structure of monthly variability

In the projection model described in section 4.2, it is initially assumed that the first baroclinic mode explains the majority of the vertical structure of the monthly variability. The validity of this assumption is investigated here by examining the vertical structure of monthly variability of meridional velocity in POCM from July 8, 1995 to September 6, 1995, the time period for which the mean fields are calculated for the stability analysis in chapters 4 and 5. Here the perturbation meridional velocity is decomposed as:

$$v_T = v + V \tag{3.1}$$

where v_T is the total meridional velocity, V is the slowly varying meridional velocity and v is the perturbation meridional velocity, defined here to be the variability with periods shorter than 60 days.

Meridional velocity was chosen to examine the vertical structure of TIWs for several reasons. First, unlike zonal velocity, the perturbations in meridional ve-

locity are larger than the mean meridional velocity. Hence, the perturbations in meridional velocity are less noisy. Second, unlike density, the vertical structure of the baroclinic eigenfunctions for meridional velocity are the set of functions $\psi_n(z)$ which are used in the projection model. Meridional velocity has also classically been the variable used to explain equatorial Rossby waves [*Gill*, 1982] and is not a derived quantity from POCM like pressure.

It is generally agreed that monthly SSH signals in the equatorial Pacific are associated with TIWs [*Malardé et al.*, 1987; *Musman*, 1989; *Périgaud*, 1990; *Giese et al.*, 1994] that extend a few hundred meters in depth [*Philander et al.*, 1985, 1986; *Halpern et al.*, 1988; *Masina et al.*, 1999a; *Kennan and Flament*, 2000]. The standard deviation of perturbation meridional velocity in POCM along 5°N in Fig. 3.4 shows that the majority of the variance is in the upper few hundred meters, which is consistent with the notion that the variability is surface trapped. However, it can also be seen that there is variability in the deep ocean to the west of about 130°W.

Additional evidence that the monthly variability associated with TIWs extends much deeper than a few hundred meters can be found in the literature. *McPhaden* [1996] examined the vertical structure of meridional velocity from current meter moorings at 7°N, 140°W and 0°, 140°W . The current meters only extended to 300m, which is not deep enough to include the zero crossing of the first mode (see appendix 7.1). However, the frequency domain EOF in v at 7°N was dominated by monthly variability that was in phase throughout the upper 300 m, which is consistent with the vertical structure of the first baroclinic mode in POCM. *Halpern et al.* [1988] found peaks at 30 days in the velocity spectra at depth of 200 and 250
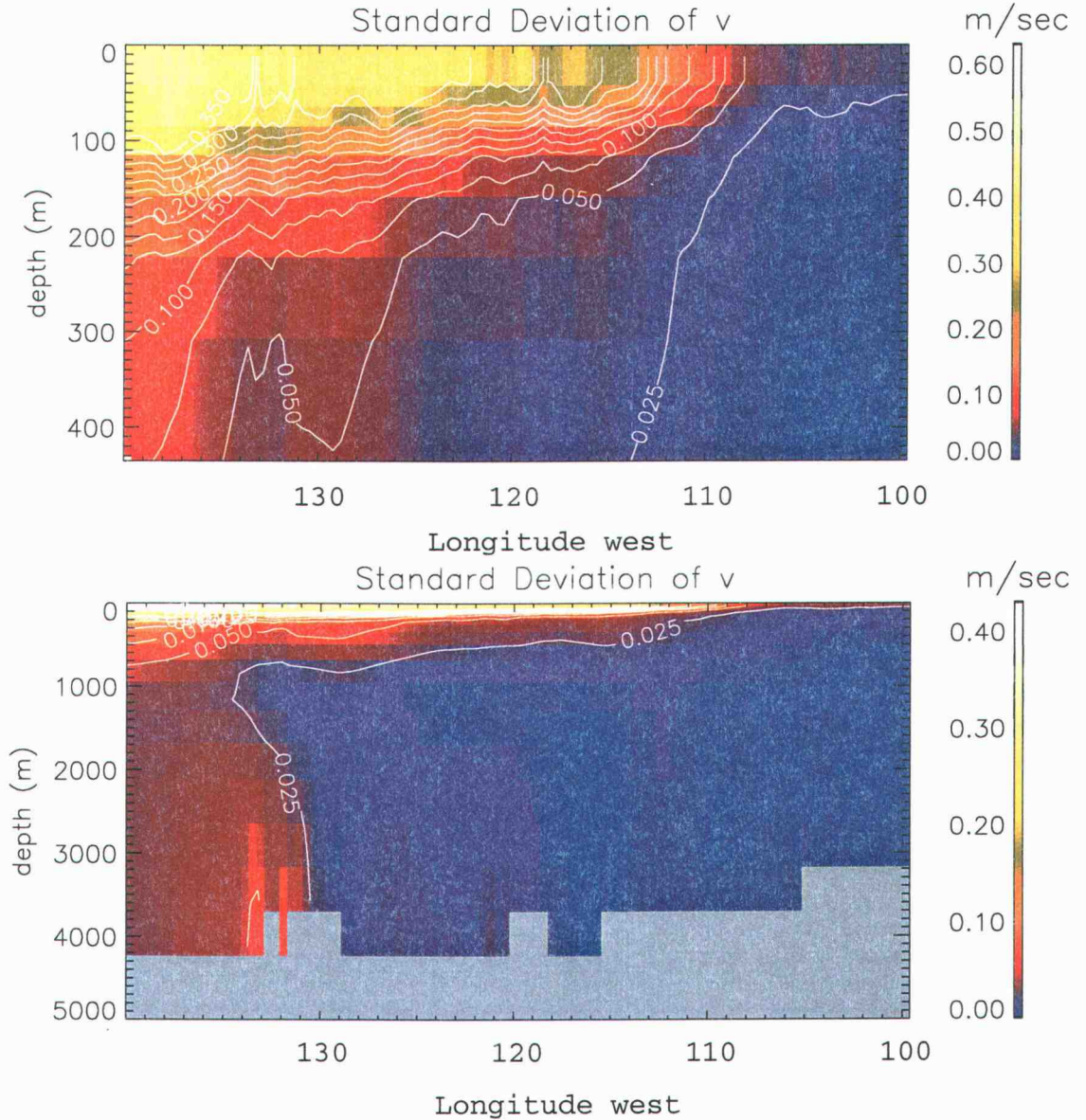
Figure 3.4: The standard deviation of meridional velocity. Velocity has been filtered to retain periods shorter than 60 days along 5°N for a 150-day period beginning on June 8, 1995. The upper 450 m are shown on an expanded scale in the top panel.

m, below the thermocline. *Eriksen and Richman* [1988] found evidence of 30-day M1 Rossby waves at depths between 1400-3000 m in current measurements of zonal velocity (u) at the equator near 140°W, showing clearly that monthly signals can penetrate below 300 m.

The vertical structure of the perturbation meridional velocity can be separated into the baroclinic modes of variability. The perturbation fields are projected onto the set of vertical eigenvectors $\psi_n(z)$ calculated from the mean $N^2(z)$ (see equation 4.13) for the case of zero background flow as discussed in appendix 7.1. Typical $\psi_1(z)$ and $\psi_2(z)$ profiles are shown in Figs. A.1 and A.2. From Fig. A.1, it can be seen that the zero crossing of the first baroclinic mode is at a depth of about 1200m. It is also apparent that the character of ψ_1 changes at 300m, where there is a slope break in the eigenvector structure.

The perturbation meridional velocities were projected onto the set of vertical eigenfunctions, ψ_n, over an area extending from 180°W to 111°W in longitude and from 20°N to 20°S in latitude during the period June 1-August 31, 1995. The resulting projections vary in latitude, longitude and time. The average percent variance described by each mode was computed, yielding the maps of the average percent of the variance described by ψ_1 and ψ_2 during June through August of 1995 that are shown in Figs. 3.5 and 3.6.

Two bands exist north and south of the equator in which ψ_1 describes more than half of the vertical structure of the perturbation meridional velocity variability. The northern band is approximately centered on 7°N and explains up to 80% of the vertical structure. The southern band is approximately centered on 7°S explaining a slightly smaller amount of the vertical structure than in the north.

Similarly, between 10°N and 10°S there are two bands where ψ_2 explains a significant percentage of the variance. The northern band is approximately centered on 2°N and explains up to 40% of the vertical variability. The southern band is approximately centered on 2°S and explains a similar amount of the vertical variability as the northern band. Higher order modes (not shown) individually account for less than 20% of the variance within 20° of the equator.

The presence of the second vertical mode in POCM monthly variability near the equator is also evident in the temperature variability. If the variability were entirely in the first vertical mode, then temperature fluctuations above the base of the mixed layer would vary in phase with variation in the thermocline. It is clear, however, from Fig. 3.7 that the two are out of phase. This difference in phase is evidence of higher order vertical mode contributions.

Although the first baroclinic mode dominates the perturbation meridional velocity in POCM, we conclude that the second vertical mode is also apparently important in the tropical band. The initial formulation of the projection model in chapter 4 considers only the first baroclinic mode. The second baroclinic mode is included in section 5.3 where it is shown to be crucially important to the formation of TIWs.

3.3   The Mean current at 134°W

The mean zonal current used in the linear stability analyses in chapters 4-7 is defined to be the average over 60 days centered on August 8, 1995 and 14° in longitude centered at 134°W. This corresponds to about two periods and one wavelength of the TIW variability in the high-pass filtered POCM fields. This time-period and
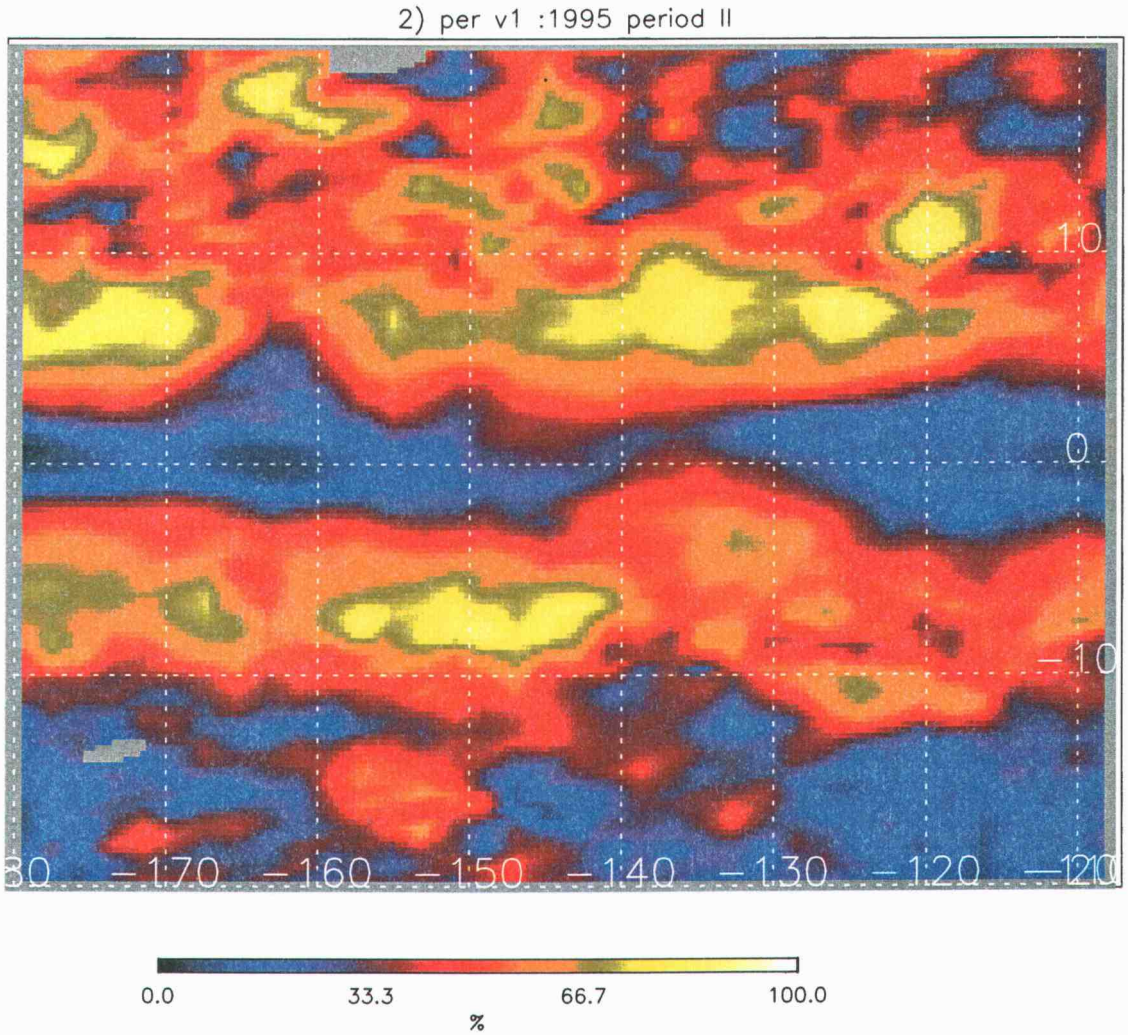
Figure 3.5: The percent of the vertical structure of perturbation meridional velocity variability that is described by the first baroclinic mode, ψ_1 computed over the 3-month period June 1-August 31, 1995.
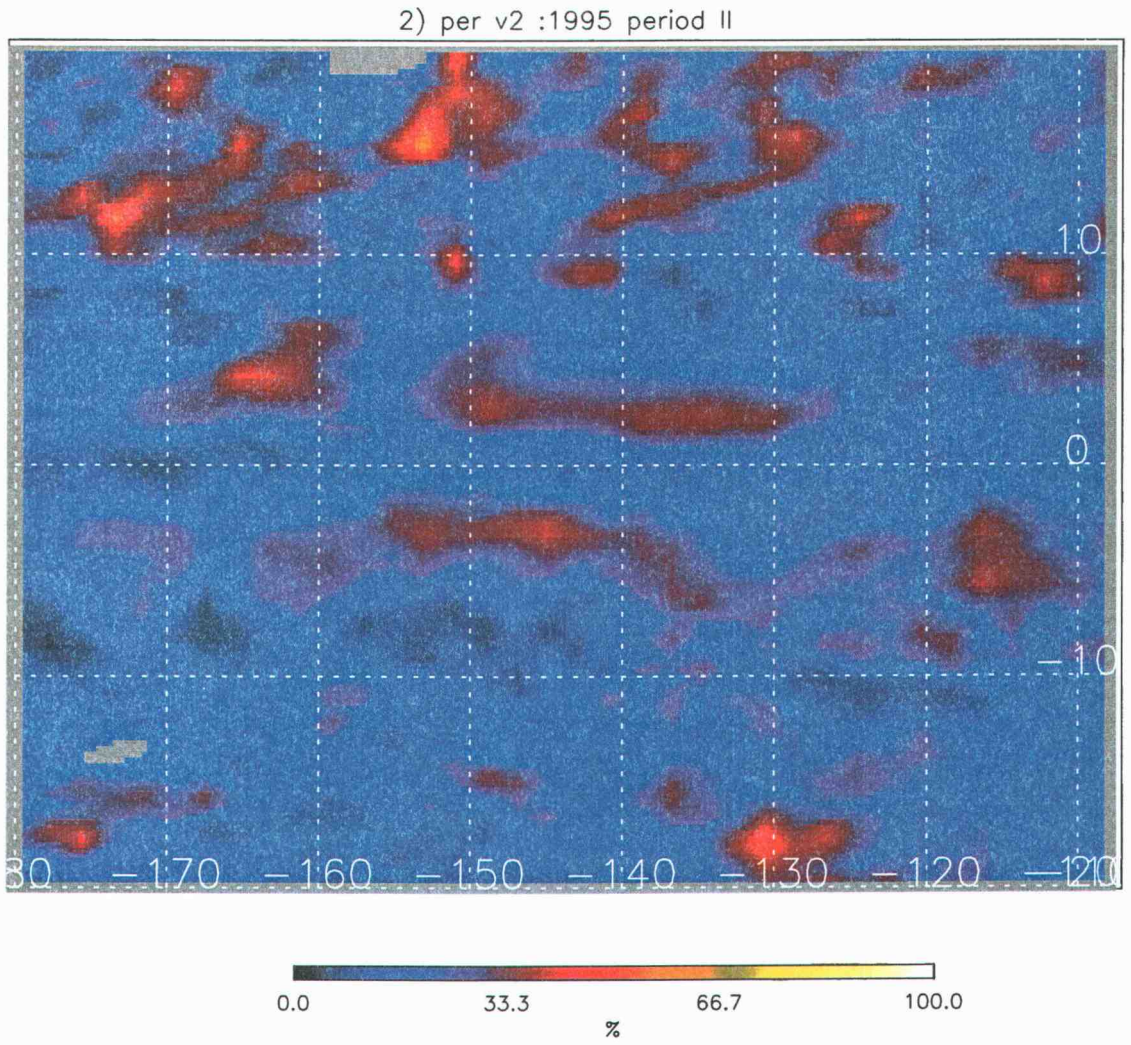
Figure 3.6: Same as Fig: 3.5, except for the second baroclinic mode, ψ_2.
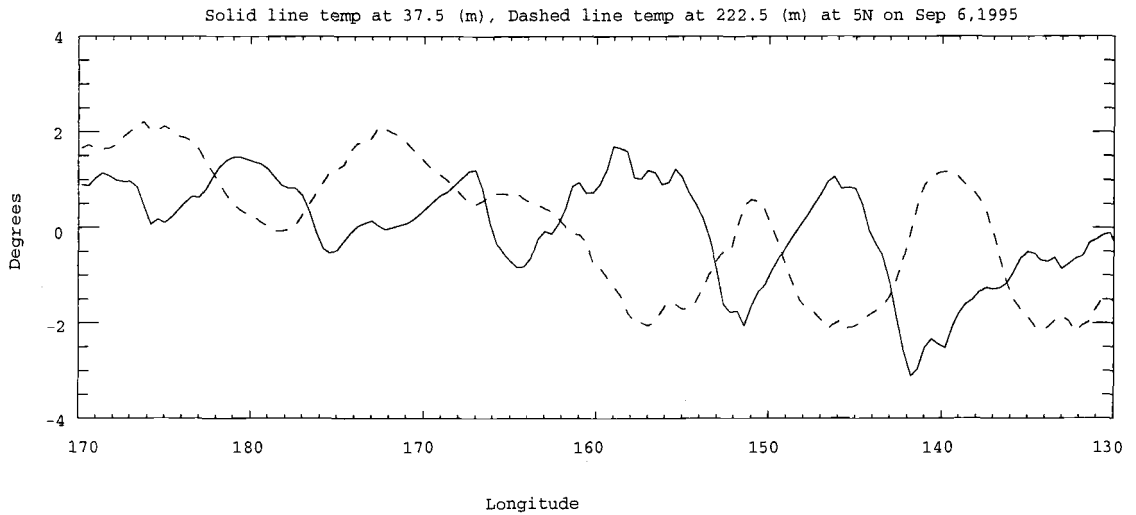
Figure 3.7: The temperature from POCM along 5°N averaged over a three day period centered on September 6, 1995. The solid line is the temperature at 37.5 meters and the dashed line is the temperature at 222.5 meters. In both cases the longitudinal mean has been removed.

area were chosen because they coincide with a La Niña event during which TIWs are generally most energetic [*Baturin and Niiler*, 1997; *Chelton et al.*, 2003]. The 1995 La Niña in particular was chosen because the monthly SSH signal in the POCM record was similar to TOPEX observations (see Fig. 3.3).

The POCM mean zonal current structure (Fig. 3.8) contains all the components of the equatorial current system that are thought to be important in the formation of TIWs. There is an EUC, NEC, SECN and SECS all of which contain strong vertical and meridional shears.

There are many ways the mean zonal currents can be represented in a simplified linear model. The currents could be averaged to a particular depth (e.g. as shown by the red dotted line in Fig. 3.8) or to the depth of a particular isotherm (e.g., the 20° isotherm as shown by the red dashed line in Fig. 3.8). These methods have an arbitrary nature. An alternative, which will be described in chapter 4, involves weighting the mean fields by the baroclinic vertical eigenfunctions. This method produces more consistent and less arbitrary results and is the basis of the projection model described in chapter 4.

3.4 The Temporal and Meridional Structure of Monthly Variability at 134°W

The characteristics of TIWs are known to vary both geographically and temporally over the course of a 9-month TIW season [*Philander et al.*, 1986; *Luther and Johnson*, 1990; *Masina et al.*, 1999a; *Chelton et al.*, 2003]. These variations can be quantified by a wavelet decomposition, which is similar to a Fourier decomposition except that the decomposition is over a set of specified basis functions (wavelets)
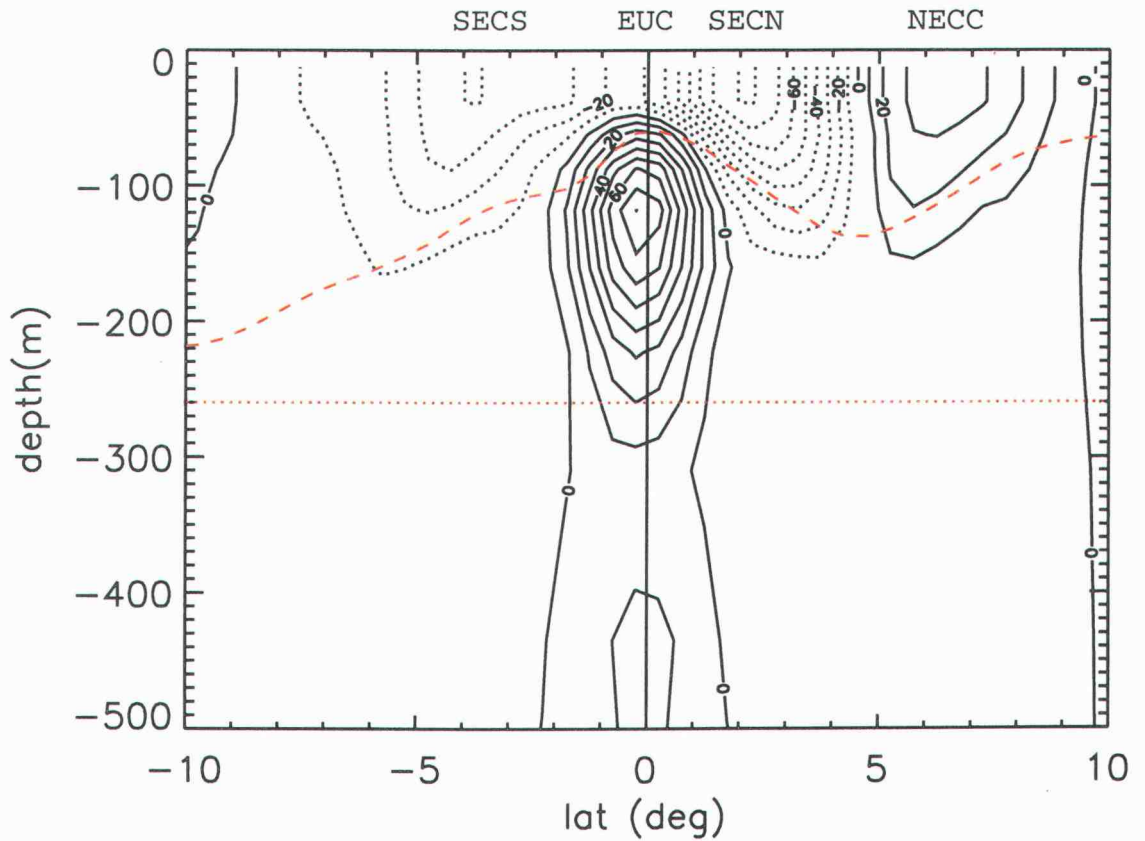
Figure 3.8: A contour plot of the mean currents from POCM at 134°W, averaged during the early period of the 1995-1996 TIW season (July 8, 1995 to September 6, 1995). The two red lines represent options for arbitrary vertical averaging of the currents. The red dotted line is the 260m isobath and the red dashed line is the 20° isotherm.

that are localized in both time and frequency space, rather than the set of sine and cosine functions [Mallat, 1999]. The structure of the wavelet used in the decomposition is chosen to resemble the structure of the signal of interest. The Morlet wavelet, which is an exponentially tapered sine and cosine (middle panel Fig. 3.9), resembles the temporal variability of TIWs (top panel Fig. 3.9). The Morlet wavelet is described by:

$$W_S(t) = \frac{1}{\pi S^2} e^{i\frac{kt}{S}} e^{-\frac{1}{2}\left(\frac{t}{S}\right)^2} \tag{3.2}$$

where t is time, S characterizes the temporal scale of the wavelet and k is the order of the wavelet, characterizing the number of sinusoidal oscillations within a e-folding scale. For the analysis presented here, the order of the wavelet was held constant at $k = 3$. The frequency of the wavelet is $\frac{k}{S}$ and the e-folding time is $S\sqrt{2}$. By representing SSH by Morlet wavelets and identifying the wavelet scale S with the largest amplitude it is possible to look at how the TIW periodicity and meridional structure change in time.

The amplitude of fit of a particular wavelet at the time t is given by,

$$A_S(t) = \frac{\int f(u) W_s(u - t) du}{\int W_s^2(u) du} \tag{3.3}$$

In the case presented in this section, f represents the time series of SSH. Because $W_s(t)$ is complex, the resulting amplitude time series $(A_S(t))$ yields both a magnitude and a phase. These two pieces of information are used later in this section to look at the cross equatorial structure of the phase and amplitude of the TIWs.
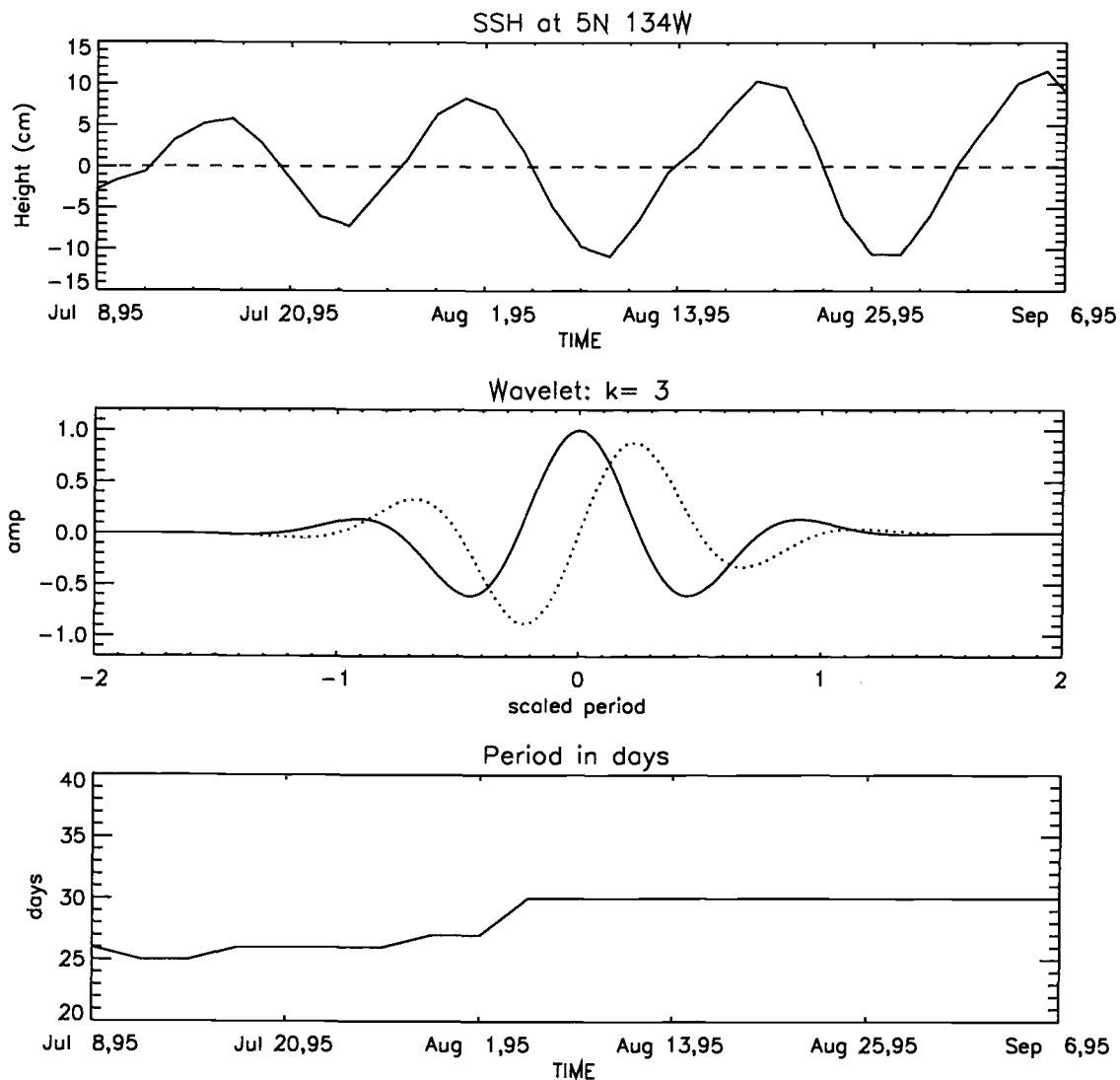
Figure 3.9: The wavelet decomposition of filtered SSH from POCM. The top panel is a slice of filtered SSH at 5°N, 134°W during the early period of the 1995-1996 TIW season. The second panel is a plot of the $k = 3$ Morlet wavelet that was fit to SSH. The solid and the dashed lines are the Gaussian tapered cosine and sine functions of the Morlet Wavelet. Wavelets of different periods, i.e. different scales (S), were fit to SSH for each time. The bottom panel is the period of the wavelet with the best fit to SSH as a function of time.

The $k = 3$ Morlet wavelets were fit to the filtered SSH signal along 5°N, 134°W (top panel Fig. 3.9) at each successive 3-day time step. The process was repeated for wavelet time scale S corresponding to periods ranging from 20 and 40 days in 1-day increments. At each 3-day time step, the period $\frac{S}{k}$ that described the greatest amount of variance was chosen to represent SSH (bottom panel of Fig. 3.9). The small span of the exponentially decaying envelope compared with the periodicity of the Morlet wavelet allows for higher resolution of the temporal variations of the structure of the signal. The down side of the small envelope is poor frequency resolution [*Mallat*, 1999]. The plot of the period as a function of time is therefore only a rough guide to the frequency content of the signal and we do not consider the small variation in period to be significant.

The scale of Morlet wavelet with the largest amplitude at 5°N, 134°W was used to characterize the meridional structure of SSH as a function of time. For a given time, this best fit wavelet at 5°N was fit to every other latitude along 134°W. Because the Morlet wavelet is complex, this fit yields an amplitude and phase that varies in latitude and time. The results of this decomposition are shown in Fig. 3.10. The top panel of Fig. 3.10 shows a contour plot of filtered SSH at 134°W. The phase relative to 5°N and the amplitude of the fit are shown in the second and third panels, respectively. This decomposition describes more than 70% of the variance in SSH between the equator and about 8°N (bottom panel of Fig. 3.10). Between about 2° and 8°S, about 40% of the variability is accounted for by this decomposition. The small amount of the variance described in the south by the wavelet decomposition is largely due to the small amplitude of the signal in the south during the first few weeks of the time period shown in Fig. 3.10. Over the

entire TIW season (July 1995-July 1996), the percent of the variance described in the south increases to about 70% (see Fig 3.11).

The meridional characteristics of the TIWs seen in the time-latitude plot of SSH are quantified by the wavelet decomposition. For example, the amplitude of the SSH in the time-latitude plot in the bottom panel of Fig. 3.10 is larger in the north. From the wavelet decomposition, the amplitude at 5°N is about a factor of 5 larger than at 5°S in early July. The asymmetry decreases over the 2-month record, becoming about a factor of 3 times larger in the north by the end of August. The phase of the SSH, more elusive than amplitude in the time-latitude plot (Fig. 3.3), can also be quantified by the wavelet analysis. The tilting near the equator in the SSH signal (top panel Fig. 3.10), which is evidence of barotropic energy conversion (see chapter 5), represents a phase lag of about 45° at the equator relative to 5°N in the second panel of Fig. 3.10. Likewise, the phase lag of SSH at 5°S relative to 5°N varies from 45° in July to 0° in August.
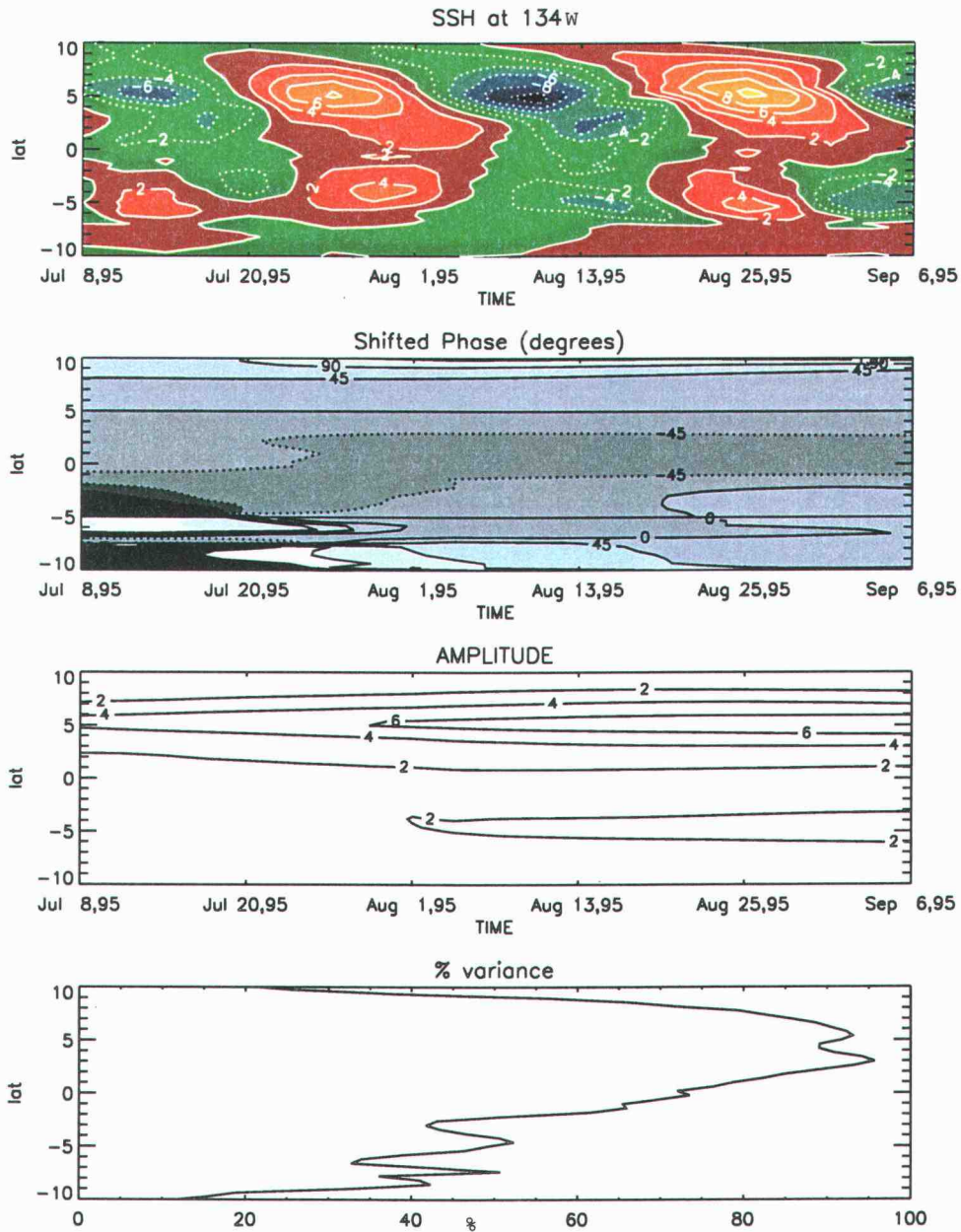
Figure 3.10: The decomposition of filtered SSH from POCM into phase and amplitude as a function of time and latitude. The top panel is a time-latitude plot of the SSH at 134°W during the early period of the 1995-1996 TIW season. At each 3-day time step, the best-fit wavelet at 5°N (Fig. 3.9) was fit to SSH at each latitude. The second panel is the phase of the wavelet fit relative to the phase at 5°N. The third panel is the amplitude of the wavelet fit in cm. The bottom panel is a plot of the amount of SSH variance that the wavelet explained over this 2 month record.

% variance July 1995 to July 1996
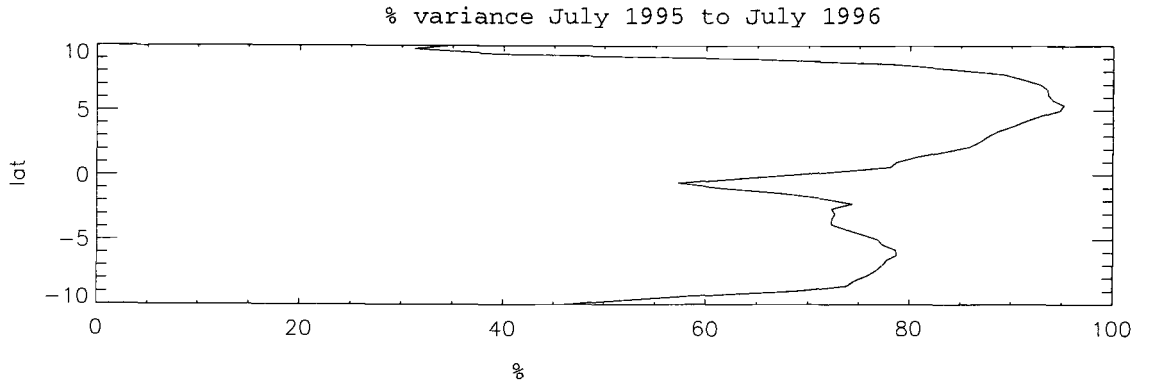
Figure 3.11: The percentage of SSH variance explained by the $k = 3$ wavelet over the period July 1995 through July 1996.

4 THE PROJECTION MODEL

Sea surface height variability in the equatorial Pacific is widely believed to be dominated by the first baroclinic mode. To understand the dynamics of the first baroclinic mode it is useful to separate it from higher order baroclinic effects. The simplest representation of the first baroclinic mode is a 2-layer reduced gravity model. When applied as a diagnostic tool, the 2-layer reduced gravity model requires an arbitrary averaging scheme in the vertical (see Appendix ??). Here, we develop a model that contains the dynamics of a representative first baroclinic mode, yet also incorporates information about the vertical structure of the equatorial oceans without employing an arbitrary vertical averaging scheme. In the presence of strong zonal currents, it should be noted that energy is scattered from the first baroclinic mode to higher-order modes as the first baroclinic mode sets up [*Proehl*, 1998].

The vertical dependence of the state variables u, v and p in a continuously stratified model can be projected onto any complete basis set of orthogonal eigenfunctions. The most common projection of this kind is the Fourier transform, where the set of sines and cosines are used as an orthogonal basis set. In the equatorial oceans, trigonometric functions do not have a particular physical meaning. There is, however, an orthogonal set of eigenfunctions, defined by the mean background stratification, that does have physical meaning. These vertical eigenfunctions are defined by the vertical profile of the buoyancy frequency and represent the vertical structure of the baroclinic modes in the absence of any mean background current (see appendix 7.1).

The method of projecting the continuous model onto the baroclinic eigenfunctions is described in this chapter. The full 3-dimensional continuous model is described in section 4.1. In section 4.2, the continuous set of equations are projected onto the vertical eigenfunctions, integrated and truncated such that the results yield a set of equations representative of the first baroclinic mode which are not subject to an arbitrary averaging scheme.

4.1 The Continuous Model

The continuous, 3-dimensional equations at the equator subject to a rigid lid, the Boussinesq approximation, and linearized around a mean background zonal current $U_o(y, z)$ and the associated geostrophically balanced mean background density $\rho_o(y, z)$ (see appendix 7.1) are:

$$\left(\frac{\partial}{\partial t} + U_o\frac{\partial}{\partial x}\right) u + \left(\frac{\partial U_o}{\partial y} - \beta y\right) v + \frac{1}{\rho_\times}\frac{\partial}{\partial x}p + \frac{\partial U_o}{\partial z}w = 0 \qquad (4.1)$$

$$\left(\frac{\partial}{\partial t} + U_o\frac{\partial}{\partial x}\right) v + \beta yu + \frac{1}{\rho_\times}\frac{\partial}{\partial y}p = 0 \qquad (4.2)$$

$$\left(\frac{\partial}{\partial t} + U_o\frac{\partial}{\partial x}\right) \rho + \frac{\partial \rho_o}{\partial y}v + \frac{\partial \rho_o}{\partial z}w = 0 \qquad (4.3)$$

$$\frac{\partial}{\partial x}u + \frac{\partial}{\partial y}v + \frac{\partial}{\partial z}w = 0 \qquad (4.4)$$

$$\rho = \frac{-1}{g}\frac{\partial}{\partial z}p \qquad (4.5)$$

In the above equations:

$$x = \text{zonal coordinate axis}$$

$$y = \text{meridional coordinate axis}$$

$$z \;=\; \text{vertical coordinate axis}$$

$$u \;=\; \text{the perturbation zonal velocity}$$

$$v \;=\; \text{the perturbation meridional velocity}$$

$$w \;=\; \text{the perturbation vertical velocity}$$

$$p \;=\; \text{the perturbation pressure}$$

$$\rho \;=\; \text{the perturbation density}$$

$$\rho_o \;=\; \text{the mean background density structure}$$

$$\rho_* \;=\; \text{the constant reference background density}$$

Equations (4.1)-(4.5) are subject to the boundary conditions:

$$v \;=\; 0, \text{ at northern and southern boundaries} \tag{4.6}$$

$$w \;=\; 0, \text{ at the top and bottom boundaries} \tag{4.7}$$

In linearizing the equations around a mean background density structure, it is assumed that:

$$\text{density} = \rho_* + \rho_o(y,z) + \rho(x,y,z,t) \tag{4.8}$$

It is also assumed that $\rho_o(y,z)$ is a weakly varying function of y,

$$\rho_o(y,z) = \rho_1(z) + \epsilon \rho_2(y,z) \tag{4.9}$$

where $\epsilon \ll 1$.

Equations (4.1)-(4.5) can be combined to obtain a single equation in terms of any one of the state variables. However, there are extraneous roots to this equation [*Proehl*, 1991]. In order to avoid these extraneous roots, equations (4.1)-(4.5) are

rewritten in terms of a coupled set of three equations involving u, v and p, as suggested by *Proehl* [1998]. The resulting equations are

$$\left(\frac{\partial}{\partial t} + U_o\frac{\partial}{\partial x}\right) u + \left(\frac{\partial U_o}{\partial y} - \beta y + \frac{g}{\rho_\times N^2}\frac{\partial U_o}{\partial z}\frac{\partial \rho_o}{\partial y}\right) v +$$
$$\left[\frac{1}{\rho_\times}\frac{\partial}{\partial x} + \frac{-1}{\rho_\times N^2}\frac{\partial U_o}{\partial z}\left(\frac{\partial}{\partial t} + U_o\frac{\partial}{\partial x}\right)\frac{\partial}{\partial z}\right] p \quad = \quad 0 \qquad (4.10)$$

$$\left(\frac{\partial}{\partial t} + U_o\frac{\partial}{\partial x}\right) v + \beta y u + \frac{1}{\rho_\times}\frac{\partial}{\partial y} p \quad = \quad 0 \qquad (4.11)$$

$$\frac{\partial}{\partial x} u + \left[\frac{\partial}{\partial y} + \frac{\partial}{\partial z}\left(\frac{g}{\rho_\times N^2}\frac{\partial \rho_o}{\partial y}\right) + \left(\frac{g}{\rho_\times N^2}\frac{\partial \rho_o}{\partial y}\right)\frac{\partial}{\partial z}\right] v +$$
$$\frac{\partial}{\partial z}\left[\frac{-1}{\rho_\times N^2}\left(\frac{\partial}{\partial t} + U_o\frac{\partial}{\partial x}\right)\frac{\partial}{\partial z}\right] p \quad = \quad 0 \qquad (4.12)$$

where

$$N^2 = -\frac{g}{\rho_\times}\frac{\partial \rho_1}{\partial z} \qquad (4.13)$$

represents the buoyancy frequency.

4.2   Projection onto the Vertical Eigenfunctions

The vertical dependencies of the state variables in (4.10)-(4.12) can be projected onto the set of eigenfunctions $\psi_n(z)$ derived in appendix 7.1:

$$u \quad = \quad \sum_n u_n(x, y, t)\psi_n(z) \qquad (4.14)$$

$$v \quad = \quad \sum_n v_n(x, y, t)\psi_n(z) \qquad (4.15)$$

$$p \quad = \quad \sum_n p_n(x, y, t)\psi_n(z) \qquad (4.16)$$

The projections (4.14)-(4.16) can then be substituted into the continuous model, equations (4.10)-(4.12). The terms in the new set of equations can be categorized into two groups. The first group of terms do not contain any mean fields, hence

the z dependence is solely due to a single eigenvector, ψ_n. The vertical dependence in these terms is eliminated by multiplying each equation by ψ_1, integrating with respect to z and applying the boundary conditions (A.2). The orthogonality condition of the eigenvectors eliminates terms that contain projections onto vertical modes greater than mode 1.

The second group of terms contain state variables and mean fields. When the equations are multiplied by ψ_1, the vertical dependence is expressed as a product of two eigenfunctions with a mean field. Here, orthogonality does not eliminate terms containing higher order vertical modes, as in the case of the first group. Consequently, the terms containing vertical modes greater than one are truncated, yielding the following definitions of the mean fields:

$$\overline{U^{(1)}}(y) \quad \equiv \quad \int_{-H}^{0} U_o \psi_1 \psi_1 \, dz \tag{4.17}$$

$$\overline{U_y^{(1)}}(y) \quad \equiv \quad \int_{-H}^{0} \frac{\partial U_o}{\partial y} \psi_1 \psi_1 \, dz \tag{4.18}$$

$$\overline{U^{(2)}}(y) \quad \equiv \quad \int_{-H}^{0} \frac{-c_1^2}{N^2} \frac{\partial U_o}{\partial z} \psi_1' \psi_1 \, dz \tag{4.19}$$

$$\overline{f^\times}(y) \quad \equiv \quad \int_{-H}^{0} \frac{g}{\rho_\times N^2} \frac{\partial U_o}{\partial z} \frac{\partial \rho_o}{\partial y} \psi_1 \psi_1 \, dz \tag{4.20}$$

$$\overline{\alpha}(y) \quad \equiv \quad \int_{-H}^{0} \frac{U_o}{\rho_\times N^2} \frac{\partial U_o}{\partial z} \psi_1' \psi_1 \, dz \tag{4.21}$$

$$\overline{H_y^{(1)}}(y) \quad \equiv \quad c_1^2 \int_{-H}^{0} \frac{1}{\rho_\times} \frac{\partial}{\partial z} \left(\frac{1}{N^2} \frac{\partial \rho_o}{\partial y} \right) \psi_1 \psi_1 \, dz \tag{4.22}$$

$$\overline{H_y^{(2)}}(y) \quad \equiv \quad c_1^2 \int_{-H}^{0} \frac{1}{\rho_\times} \left(\frac{1}{N^2} \frac{\partial \rho_o}{\partial y} \right) \psi_1' \psi_1 \, dz \tag{4.23}$$

An example of these mean fields is shown in Fig. 4.1.

For zonally propagating wave solutions, the x-t dependences of the coefficients u_1, v_1 and p_1 in the expansions (4.14-4.16) are assumed to have the form $e^{i(kx - \omega t)}$.
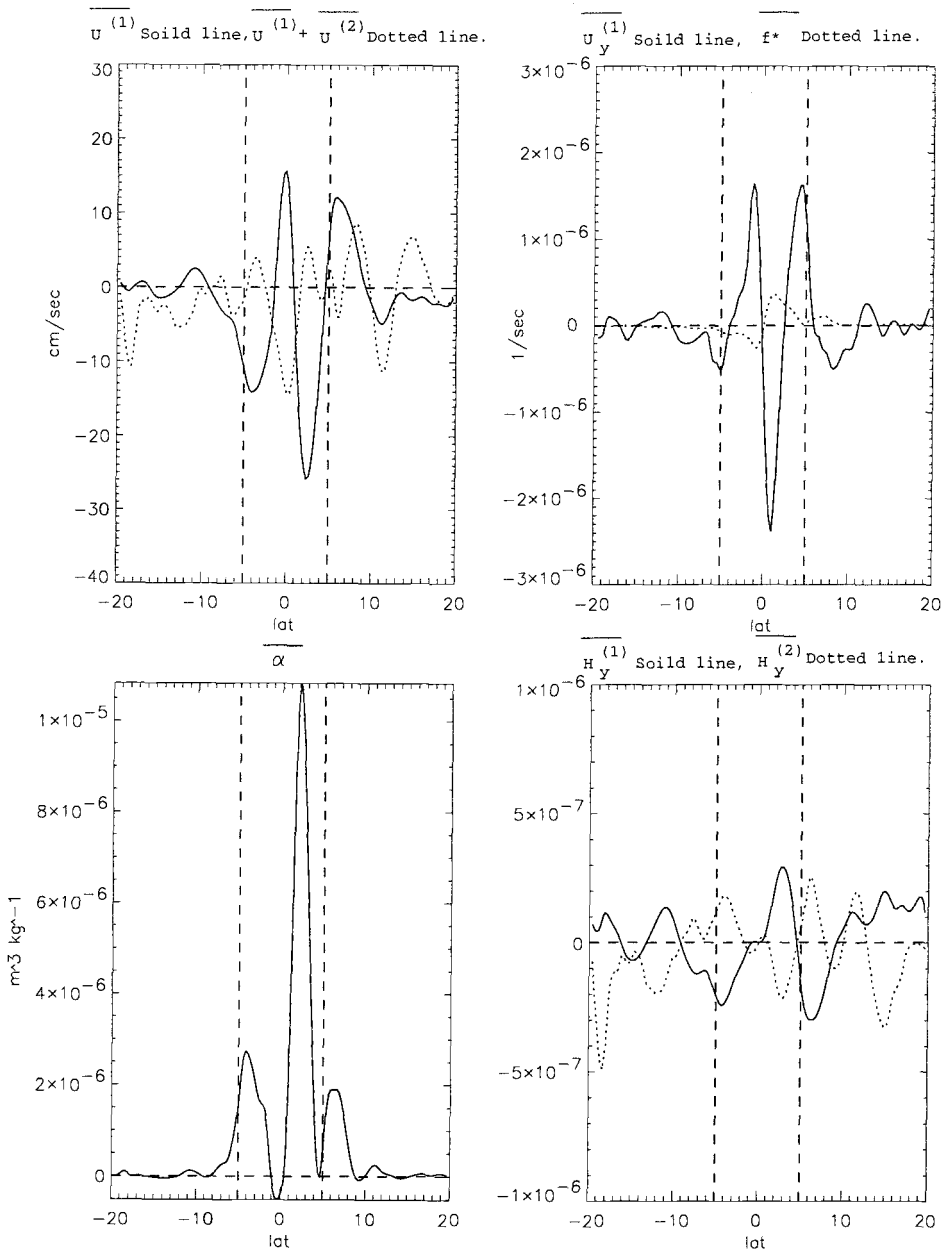
Figure 4.1: Plots of the mean fields from equations. (4.17)-(4.23) computed over the period from July 8, 1995 to September 6, 1995 at 134°W (the same as Fig. 3.8). The top left panel is a plot of $\overline{U^{(1)}}$ (the solid line) and $\overline{U^{(2)}} + \overline{U^{(1)}}$ (the dotted line). The top right panel is a plot of $\overline{U_y^{(1)}}$ (solid line) and $\overline{f^*}$ (the dotted line). The bottom left panel is a plot of $\overline{\alpha}$ and the bottom right panel is a plot of $\overline{H_y^{(1)}}$ (solid line) and $\overline{H_y^{(2)}}$ (dotted line).

Then the system of equation can be written in matrix form as:

$$
\begin{bmatrix}
\overline{U^{(1)}}k & i(\beta y - (\overline{U_y^{(1)}} + \overline{f^z})) & \left(\frac{1}{\rho_*} - \overline{\alpha}\right)k \\
-i\beta y & \overline{U^{(1)}}k & -\frac{i}{\rho_*}\frac{\partial}{\partial y} \\
c_1^2\rho_* k & -i\rho_*\left(g\left(\overline{H_y^{(1)}} + \overline{H_y^{(2)}}\right) + c_1^2\frac{\partial}{\partial y}\right) & (\overline{U^{(1)}} + \overline{U^{(2)}})k
\end{bmatrix}
\begin{bmatrix}
u_1 \\
v_1 \\
p_1
\end{bmatrix}
$$

$$
= \omega
\begin{bmatrix}
1 & 0 & \frac{1}{c_1^2\rho_*}\overline{U^{(2)}} \\
0 & 1 & 0 \\
0 & 0 & 1
\end{bmatrix}
\begin{bmatrix}
u_1 \\
v_1 \\
p_1
\end{bmatrix}
\tag{4.24}
$$

where u_1, v_1 and p_1 are now functions only of y.

Although the first vertical mode dominates the vertical structure of the currents in the equatorial pacific there are small areas the equator where the second vertical mode describes a significant percentage of the vertical variability (see section 3.2). To explore whether contributions from second and higher order vertical modes affect the linear stability of a given meridional current profile, a formulation of equation (4.24) is given in Appendix 7.1 for an arbitrary number of vertical modes. The results of this analysis are discussed in chapter 5.

The terms in the matrix equation (4.24) can be simplified by determining the relative magnitudes of the coefficients computed from the projection of time-averaged zonal and vertical velocity sections from the POCM model. An example of the mean fields along 134° W for the 3-month period from July to September 1995 is shown in Fig. 4.1. Restricting attention to the region of the dispersion space where TIWs are found,

$$
\overline{\omega/k} \leq 1 \text{ ms}^{-1},
\tag{4.25}
$$

it is apparent that

$$|\overline{\alpha}| \ll \left|\frac{1}{\rho_{\times}}\right| \tag{4.26}$$

$$\left|\frac{\omega}{k}\frac{1}{c_1^2\rho_{\times}}\overline{U^{(2)}}\right| \ll \left|\frac{1}{\rho_{\times}}\right| \tag{4.27}$$

If these smaller terms are neglected, (4.24) reduces to:

$$\begin{bmatrix} \overline{U^{(1)}}k & i(\beta y - (\overline{U_y^{(1)}} + \overline{f^{\times}})) & \frac{1}{\rho_*}k \\ -i\beta y & \overline{U^{(1)}}k & -\frac{i}{\rho_*}\frac{\partial}{\partial y} \\ c_1^2\rho_{\times}k & -i\rho_{\times}\left(g\left(\overline{H_y^{(1)}} + \overline{H_y^{(2)}}\right) + c_1^2\frac{\partial}{\partial y}\right) & (\overline{U^{(1)}} + \overline{U^{(2)}})k \end{bmatrix}\begin{bmatrix} u_1 \\ v_1 \\ p_1 \end{bmatrix} = \omega\begin{bmatrix} u_1 \\ v_1 \\ p_1 \end{bmatrix}$$

$$\tag{4.28}$$

This equation bears a striking resemblance to the matrix equation (B.5) for a 2-layer reduced-gravity model (see Appendix ??). For the zero mean flow case, the matrix equations (B.5) and (4.28) are exactly the same. When the mean background fields are considered, counterparts can be drawn between the two equations (see table 4.1). The equivalent to $g'H(y)$ in (B.5) becomes c_1^2 in (4.28), U_o becomes $\overline{U^{(1)}}$ in the equations for u_1 and v_1, while, U_o becomes $(\overline{U^{(1)}} + \overline{U^{(2)}})$ in the equation for pressure where the addition of $\overline{U^{(2)}}$ is an effect of the chain rule, $\partial U_o/\partial y$ is modified to $\overline{U_y^{(1)}} + \overline{f^{\times}}$ and $\partial H(y)/\partial y$ replaces $\left(\overline{H_y^{(1)}} + \overline{H_y^{(2)}}\right)$. Gradients in mean layer thickness, $\partial H/\partial y$ in the 2-layer reduced gravity model, are represented by gradients in density, $\left(\overline{H_y^{(1)}} + \overline{H_y^{(2)}}\right)$, in the projection model. $\overline{H_y^{(1)}}$ corresponds to geostrophy in the 2-layer reduced gravity model, while $\overline{H_y^{(2)}}$ is a new term in the projection model, which resembles a density gradient in geostrophic balance with $\overline{U^{(2)}}$. $\overline{f^{\times}}$ can be seen to be βy divided by the gradient Richardson number, $\frac{N^2}{(\frac{\partial U_o}{\partial z})^2}$.

Reduced-Gravity Model	Projection Model momentum equations	Projection Model continuity equation
$g'H(y)$		c_1^2
$U_o(y)$	$\overline{U^{(1)}}$	$\left(\overline{U^{(1)}} + \overline{U^{(2)}}\right)$
$\partial U_o/\partial y$	$\overline{U_y^{(1)}} + \overline{f^{\times}}$	
$\partial H/\partial y$		$\left(\overline{H_y^{(1)}} + \overline{H_y^{(2)}}\right)$

Table 4.1: A summary of the relationship between the terms in the 2-layer reduced gravity model and the one mode Projection Model.

The energy conversion in the one-mode projection model are defined by the fallowing equation:

$$-\rho_{\times}\left(\overline{U_y^{(1)}} + \overline{f^{\times}}\right)[v_1 u_1] - \frac{g}{c_1^2}\left(\overline{H_y^{(1)}} + \overline{H_y^{(2)}}\right)[v_1 p_1] - [(v_1 p_1)_y] = \omega_i[E_1] \quad (4.29)$$

In equation (4.29), ω_i is the imaginary part of the eigenvalue, $E_1 = \rho_{\times}\left(v_1^2 + u_1^2\right) + \frac{p_1^2}{\rho_{\ast}c_1^2}$ is the total vertically integrated mode-1 perturbation energy, the potential energy has been derived from the traditional definition [*Luther and Johnson*, 1990] and the bracketed terms have been zonally averaged over a wavelength.

From left to right, the terms in equation (4.29) represent barotropic and Kelvin-Helmholtz energy conversions, baroclinic energy conversion, and wave flux divergence, which only redistributes energy in the domain. The $\frac{\partial U_o}{\partial z}w$ term in equation (4.1) is the source of Kelvin-Helmholtz energy conversions. In matrix equation (4.28) $\frac{\partial U_o}{\partial z}w$ is replaced by $\overline{f^{\times}}$, $\overline{\alpha}$ and $\frac{1}{c_1^2\rho_{\ast}}\overline{U^{(2)}}$ in the first row equation. The particular scales in POCM show that $\overline{\alpha}$ and $\frac{1}{c_1^2\rho_{\ast}}\overline{U^{(2)}}$ are negligible, as shown in equations (4.26) and (4.27), while $\overline{f^{\times}}$ can make a small contribution to Kelvin-Helmholtz energy conversion near the equator.

We thus have a system of equations that are not arbitrarily averaged in depth and contain information about the vertical structure of the ocean. Compared with the 2-layer reduced-gravity model, the projection model provides a less subjective and more representative model of a vertical mode 1 equatorial ocean while retaining relatively simple physics. The vertical resolution of the model can easily be increased by including higher order vertical modes (see appendix 7.1).

The matrix eigenvalue problem (4.28) was solved on a c-grid with u_1 and v_1 sharing the same grid points and p_1 at the adjacent grid points. The northern and southern boundaries were placed at the u_1 and v_1 grid points at 19.75°N and 19.75°S. The eigenvalues and eigenfunction of the matrix were solved using the EISPACK subroutine package.

5 APPLICATION OF THE PROJECTION MODEL

The meridional structure and dispersion characteristics of Rossby waves in the presence of mean currents are examined during the beginning of the 1995-1996 TIW season. This time period was chosen because the SSH signals in TOPEX and POCM are similar during the TIW season (Fig. 3.3) as discussed in chapter 3. The characteristics of the SSH variability from the Projection Model are compared with those from the wavelet analysis of POCM SSH over the same time period considered in Section 3.1. The meridional structure and the dispersion characteristics are found by substituting the mean fields along 134°W from POCM into the eigenvalue problem (4.28) and examining the resulting eigenvalues and eigenvectors. The mean fields are computed during the beginning of the TIW season before the TIWs become finite amplitude [*Kennan and Flament*, 2000] and the assumption of linearity is no longer valid. For this study, the period from July 8, 1995 to September 6, 1995 was chosen because the TIW signal was small. The structure of the mean currents is shown in Fig. 3.8.

In this analysis, the mean fields from POCM were used to compute eigenvectors and eigenvalues over a range of wavenumbers, k. The real part of the eigenvalue represents the frequency of the wave and is displayed as a dispersion relation, while the imaginary part of the eigenvalue represents the growth rate of the wave. When written in Eulerian form, the phase between u, p and v represents the amount of energy transfer between the mean and the perturbations, eq. (4.29), while the amplitude is the size of the disturbance. If the wave is stable, u and p will be in quadrature with v and hence there will be no energy transfer.

5.1 $\overline{U^{(1)}}$ at 134°W

The mean background current in POCM (Fig. 3.8) was adjusted slightly for the computation of mean fields in eqs. (4.17)-(4.23) and eqs. (C.1)-(C.6) as to represent more closely the geostrophic current in the model by reducing the effects of Ekman currents. This was achieved by replacing the mean current in the top layer with the mean current in the second layer of the model.

It is useful to look at the general structure of $\overline{U^{(1)}(y)}$, which acts similarly to the upper layer mean zonal velocity $U(y)$ in the upper layer of a 2-layer reduced gravity model (see section 4.2). From Fig. 5.1, the presence of the NECC, the northern branch of the South Equatorial Current (SECN), the EUC, and the southern branch of the South Equatorial Current (SECS) are apparent in the meridional profile of $\overline{U^{(1)}(y)}$. Hence, the vertical projection method retains all of the currents that are thought to be important to the stability of the equatorial current system. For present purposes, $U(y)$ was defined to be the average over the upper 260 m of the POCM model. It is evident that the amplitudes of the components of the equatorial current system in $\overline{U^{(1)}(y)}$ are diminished compared $U(y)$ (the dotted line in Fig. 5.1). The differences in the amplitudes of the currents in $\overline{U^{(1)}(y)}$ and $U(y)$ are sensitive to the depth of the vertical average, highlighting the arbitrary nature of a vertical average as discussed previously in chapter 4. There are small differences in the westward currents (SECN and SECS), which are less stable than the eastward currents [*Philander*, 1976]. The largest difference is in the relatively stable eastward EUC whose vertical structure contains higher vertical modes then the NECC, SECN and SECS (see Fig. 3.8).
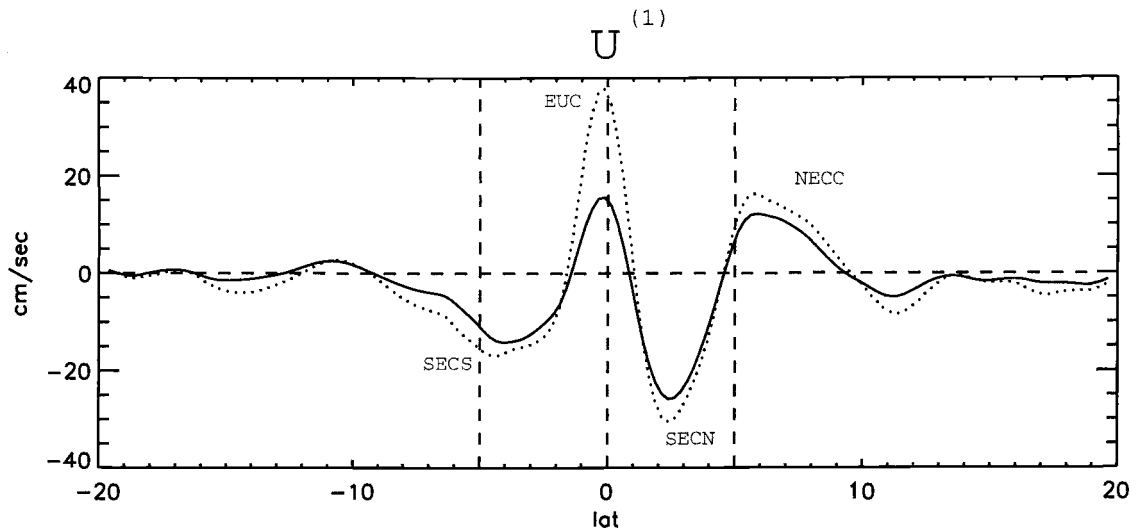
Figure 5.1: Two different estimates of the upper-ocean mean velocity along 134°. Both are derived from the mean vertical velocity section shown in Fig. 3.8. The solid line is $\overline{U^{(1)}(y)}$ from the one-mode projection model. The dotted line is a 260 m vertical average of the $U(y, z)$ section in Fig. 3.8

5.2   The One-Mode Projection Model

The solutions to the simplest version form of the projection model are investigated in this section. By only projecting onto one vertical mode, the structure of the equations are similar to the 2-layer reduced gravity model (see section 4.2) and act as a good first-order look at the effects of mean fields on the structure and dispersion characteristics of TIWs.

The mean fields (Fig. 4.1) produce the solutions shown in Fig. 5.2. The first-meridional, first-baroclinic Rossby waves (referred to as M1) shown as the middle solid line in panel c of Fig. 5.2 are closest in dispersion space to the observed SSH variability in POCM (the black box in panel c of Fig. 5.2). The dotted lines in the same figure are the solutions for the case with no background flow. The

addition of the mean flow systematically reduced the phase speed of M1 Rossby waves for wavenumbers smaller then 7.5×10^{-4} cycles/km. The phase speeds of the second-meridional mode, first-baroclinic mode Rossby waves (referred to as M2) re increased for wavelengths less than 1250 km, These results are consistent with those of *Chang and Philander* [1989]. At shorter wavelengths, the phase speed of the M1 and M2 Rossby waves decrease and begin to interact with the SECN, which has a speed of 0.25 m/sec and is represented by the red line. All of the solutions are effectively stable in this single-mode projection; i.e. the most unstable solutions have e-folding times several times longer than the duration of the TIW season.

While the dispersion characteristics are only moderately affected, the meridional structure of the M1 Rossby wave is significantly altered by the background mean currents. Panels d-f in Fig. 5.2 show the meridional structure of the M1 Rossby wave for solutions with 30-day period and 1300 km wavelength. The solid curves represent the solutions based on $\overline{U^{(1)}(y)}$ shown in Fig. 5.1, while the dash-dotted lines represent the zero-mean flow case. In SSH (panel d), the mean flow causes the maxima to shift poleward, the amplitude in the south decreases to 40% of the amplitude in the north, and the trough at the equator deepens by 50%. The structures in u and v show similar differences, with peaks shifting poleward and amplitudes decreasing in the south. As noted above, these solutions are stable, hence u and p are in or out of phase with each other. Likewise, v is 90° out of phase with u and v.

These effects on the meridional structure of the solutions are a robust feature of this analysis. Panels a and b of Fig. 5.2 show the wavenumber dependence of the meridional structure of p for the mean flow case and the zero-mean flow
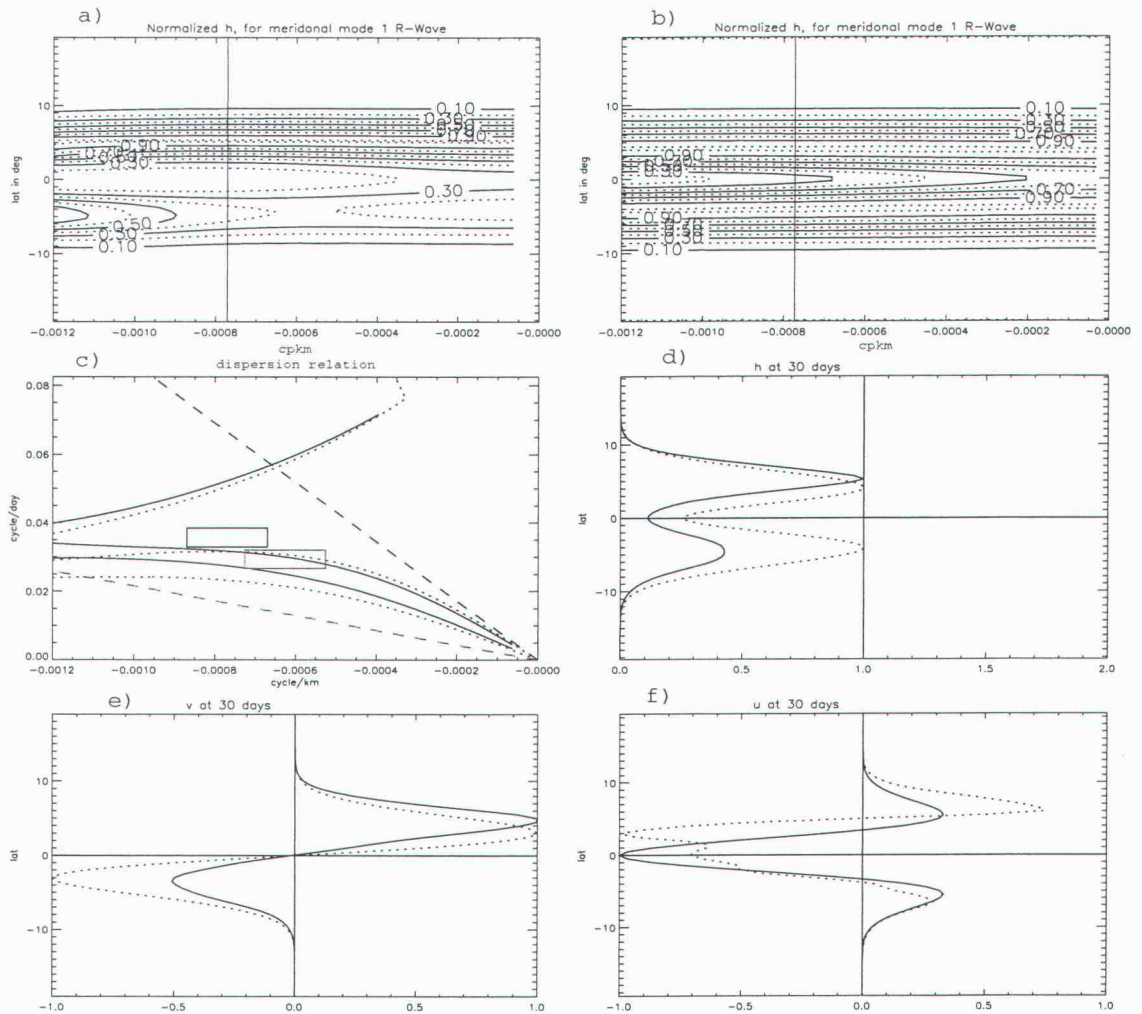
Figure 5.2: The solutions to the one-mode projection model. Panel a) is a contour plot of SSH of the M1 Rossby wave vs. wavenumber for the case with the mean flow $\overline{U^{(1)}(y)}$ shown in Fig. 5.1. Panel b) is the same as a), but for the case of zero mean flow. Panel c) is the dispersion relation. The solid lines represent the eigenvalues from the mean flow case. The dotted lines represent the eigenvalues from the zero mean flow case. The black dashed line represents a phase speed of 1 m/sec. The red dashed line represents the fastest westward value of $\overline{U^{(1)}(y)}$ in Fig. 5.1. The black and red boxes represent estimates of the wavenumber-frequency content of TIWs in POCM and TOPEX, respectively. Panel d) is a latitudinal profile of the eigenfunction for SSH for the 1300km, 30 day wave, where the maximum value has been normalized to one. The solid and dotted lines represent the mean flow and zero mean flow cases, respectively. Panels e) and f) are the same as panel d), except for the eigenfunctions of v and u, respectively.

case, respectively. While the zero-mean flow case shows symmetric structure in amplitude for all wavenumbers, the presence of the mean flow can be seen to decrease the amplitude of the SSH in the south for wavelengths between 800-20,000 km. At higher wavenumbers, the amplitude in the south become 60% of that in the north. As the wavenumber decreases, the amplitude in the south also decreases, reaching a minimum of 35% of the amplitude in the north at a wavelength of about 1800 km. TIWs exist in the 1000-2000 km region where the meridional asymmetry in SSH is most sensitive to changes in wavenumber. Additionally, the mean flow consistently deepens the trough at the equator and shifts the northern maximum in SSH poleward.

This simple model provides a valuable first-order look at the meridional structure of wave solutions close to the TIW period and wavenumber range. The amplitudes of the asymmetric solutions are similar to those deduced in section 3.4 from POCM SSH fields. The degree of asymmetry is somewhat sensitive to the wavenumber of the instability, particularly in the range of reasonable values for TIWs. These solutions give an estimate of the structure of the free waves that are thought to be generated by TIWs [*Cox*, 1980]. Because the one-mode projection model is stable for the mean zonal velocity section considered here, these solutions cannot explain the phase structure of TIWs in POCM.

5.3   The Two-Mode Projection Model

The one-Mode Projection model discussed in the pervious section, was not able to capture the instabilities that generate TIWs. By increasing the vertical resolution to include the first two vertical modes, the mean current structure Fig. 3.8 is

more completely represented. The added complexity produces a set of six coupled equations (see appendix 7.1). The mean fields are computed over the same time period as for the one-mode projection model and are shown in Fig. 5.1.

Unlike the one-mode projection model, the two-mode projection model produces unstable solutions (Fig. 5.3). The top panel shows a plot of the growth rate as a function of wavenumber for the most unstable solutions. The fastest growing solution, with a wavelength of 1384 km, is the most likely to occur. The dispersion relation for the two-mode projection model (the bottom panel in Fig. 5.3) shows an increase in phase speed from the one-mode model such that the observed wavenumber-frequency characteristics of the TIWs in POCM (the black box in the lower panel of Fig. 5.3) are consistent with the dispersion relation of the two-mode projection model. At longer wavelengths, the solutions become stable, splitting into two stable modes at -5×10^{-4} cpkm. The characteristics of these two stable modes will be investigated later in chapter 7.

As in the case of the one-mode projection model, the meridional structures of the solutions of the two-mode projection model are sensitive to wavenumber in the TIW wavenumber range. The amplitude and phase of the fastest growing solution over the TIW wavenumber range are shown in the lower two panels of Fig. 5.4. Amplitudes at 5° north are 2 to 10 times larger than those at 5° south and the phase at 5° north leads the phase at 5° south by 0° to 45° degrees. This sensitivity provides an environment in which a host of different meridional structures are possible, depending on the wavenumber, making identification of a particular structure in the SSH record difficult.
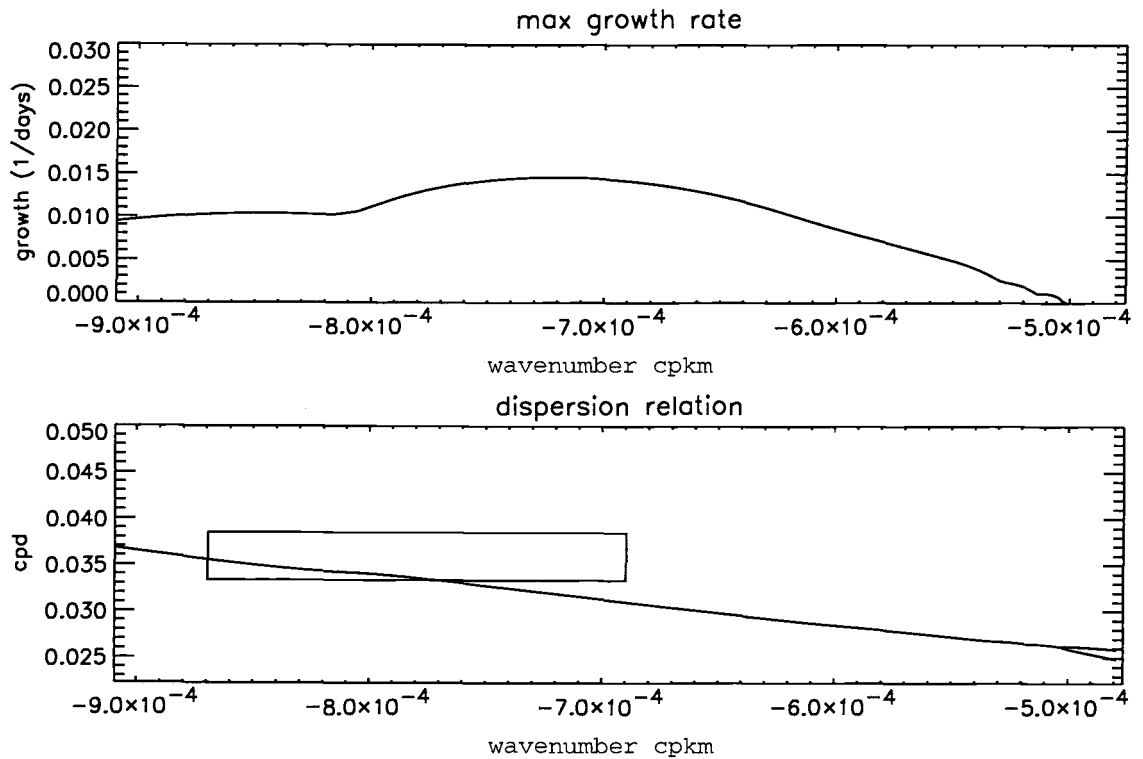
Figure 5.3: The eigenvalues from the stability analysis of the two-mode projection model. The upper panel shows the growth rate of the solutions as a function of wavenumber. The structure of the fastest growing solution at a wavenumber of 7.2×10^{-4} cpkm is plotted in Fig. 5.5. The bottom panel shows the frequency of the solutions as a function of wavenumber. The box in the plot represents the estimate of the wavenumber-frequency content of TIWs in POCM.
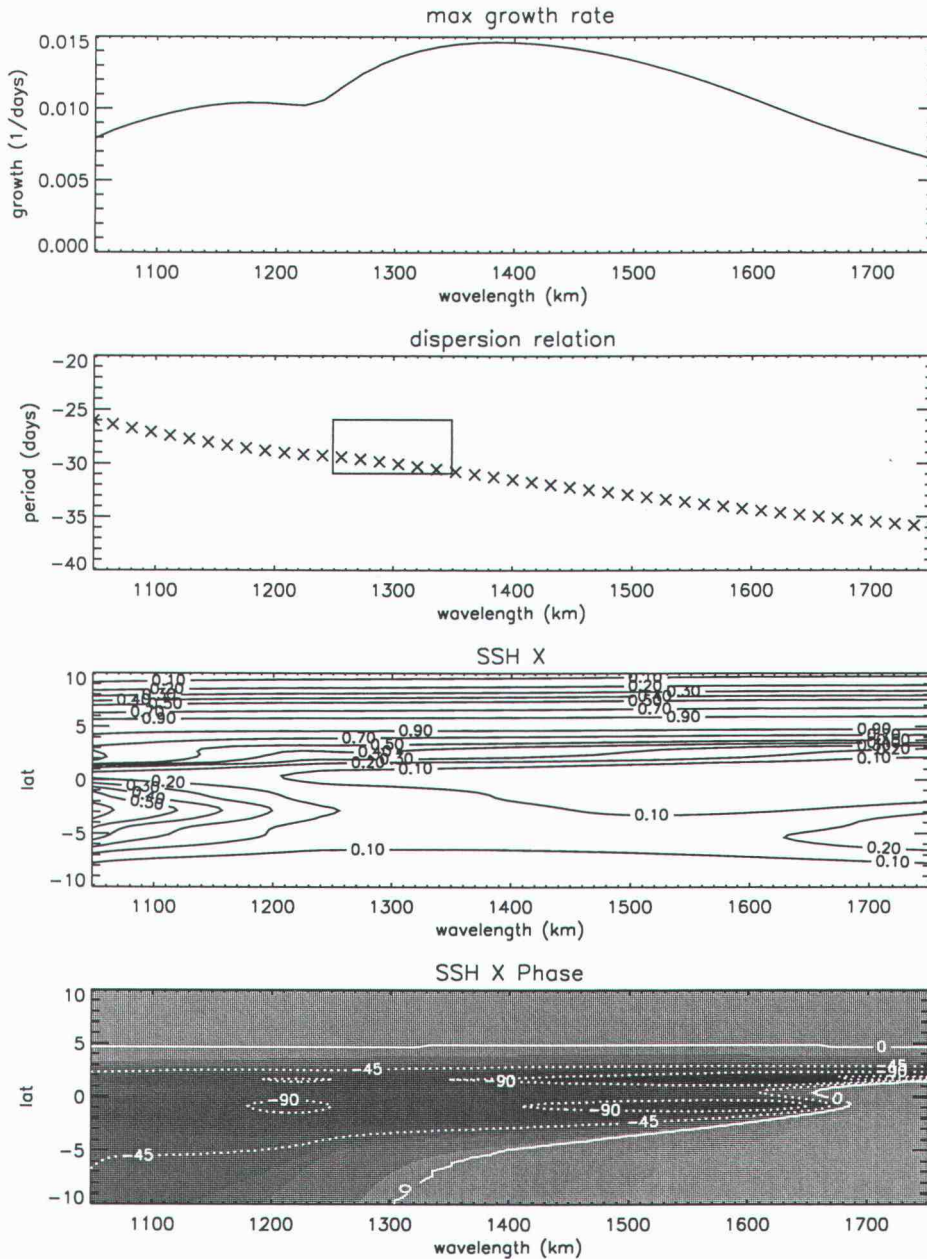
Figure 5.4: The eigenvalues and eigenvectors from the stability analysis of the two-mode projection model. The first panel shows the growth rate of the solutions as a function of wavelength. The structure of the fastest growing solution (wavelength of 1384 km) is plotted in Fig. 5.5. The second panel shows the period of the solutions as a function of wavelength. The box in the plot represents the estimate of the wavenumber-frequency content of TIWs in POCM. The bottom two panels are contour plots of the amplitude and phase of the SSH eigenfunctions as a function of wavelength.

The fastest growing mode from the two-mode projection model (Fig. 5.5) has an amplitude structure in SSH very similar to that of the stable solution from the one-mode projection model (Fig. 5.2d). Most notably, the peaks in SSH amplitude are still at 5°N and 5°S, with a larger amplitude in the north. However, the amplitude in the north is more than 5 times larger than in the south, compared with less than a factor of 3 difference in the one-mode projection model. This structure of the eigenfunction from the two-mode projection model is more similar to the SSH variability in POCM shown in Fig. 3.10.

Whereas the stable one-mode solution had constant phase with latitude, the phase of the unstable two-mode solution varies with latitude (second panel Fig. 5.5). SSH at 5°S is in phase with SSH at 5°N. The approximate 90° phase lag near the equator is evidence of an equatorward eddy transport of zonal momentum which leads to the barotropic conversion of energy in the presence of the large mean velocity shears in the region. As in amplitude, these latitudinal variations in phase are similar to latitudinal "tipping" of the structure of SSH in POCM.

The vertical structure of the pressure field is shown as the fraction of the total amplitude in each of the baroclinic modes in the bottom panel of Fig. 5.5. Except within a few degrees of the equator, SSH variability is dominated by the first baroclinic mode. Near the equator, the variability is approximately equally partitioned between vertical modes on and two.

The relationships between p, u and v are not as simple as in the one-mode projection model. The introduction of the instability forces the phases of u and p to no longer be in quadrature with v (compare second panels of Figs. 5.5, 5.6 and 5.7). This results in a transfer of energy between the mean and the perturbations
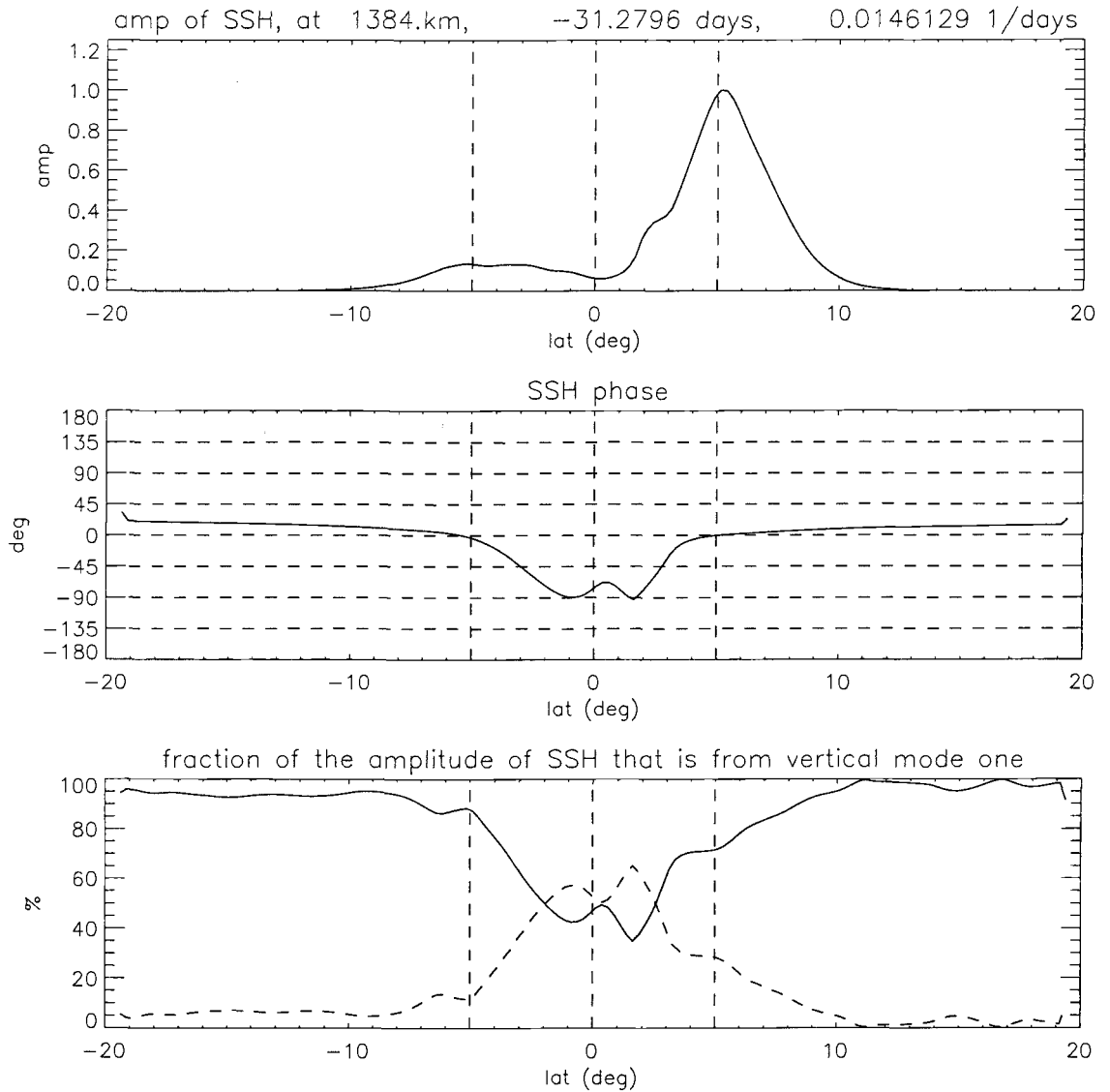
Figure 5.5: Latitudinal profiles of the amplitude (top) and phase (middle) relitive to 5°N of the eigenfunctions of SSH for the fastest growing solution to the two-mode projection model. The bottom panel shows the percent of SSH in each vertical mode, with the solid line representing mode 1 and the dashed-line representing mode 2. This solution has an e-folding time of 68 days, a period of 31 days and a wavelength of 1384 km.

(eq. 4.29). The vertical structure of the state variables is also different. The meridional velocity v has a vertical structure similar to p poleward of 2°. Unlike p, however, v is almost wholly made up of mode 2 near the equator. Within 5° of the equator, u alternates being dominated between mode 1 and mode 2 (Fig. 5.6). Outside of this region, u variability is dominated by only mode 1, similar to p and v.

The energy transfer of this mode is mostly barotropic (Fig. 5.8) and occurs just north of 2.5°N on the poleward flank of the SECN (see Fig. 5.1). However, baroclinic energy conversion is not negligible (see the thin solid line in Fig. 5.8), which also contributes to perturbation energy conversion on the poleward flank of the SECN. The dominance of the poleward flank of the SECN as a region of energy transfer hints at its importance in the development of the instability. This is discussed extensively in the sensitivity studies in chapter 6.

The nature and location of the maximum energy transfer is not surprising. Previous linear stability analyses have all found barotropic conversion associated with the SECN to be the main source of energy for TIWs [*Philander*, 1978; *Proehl*, 1998]. However, there has been debate as to which side of the SECN is important. Originally, *Philander* [1978] and *Cox* [1980] found the shear between the SEC and the NECC to be important, which has been supported by observations [*Baturin and Niiler*, 1997]. A More recent linear stability analysis finds that the shear between the SECN and the EUC is the energy source for the instabilities [*Proehl*, 1998], a region where observations have also found barotropic energy transfer [*Luther and Johnson*, 1990; *Qiao and Weisberg*, 1995]. The present analysis finds that the shear on the poleward flank of SECN near the maximum of the SECN is the

amp of u , at 1384.km, −31.2796 days, 0.0146129 1/days

Phase of u

fraction of the amplitude of u that is from vertical mode one
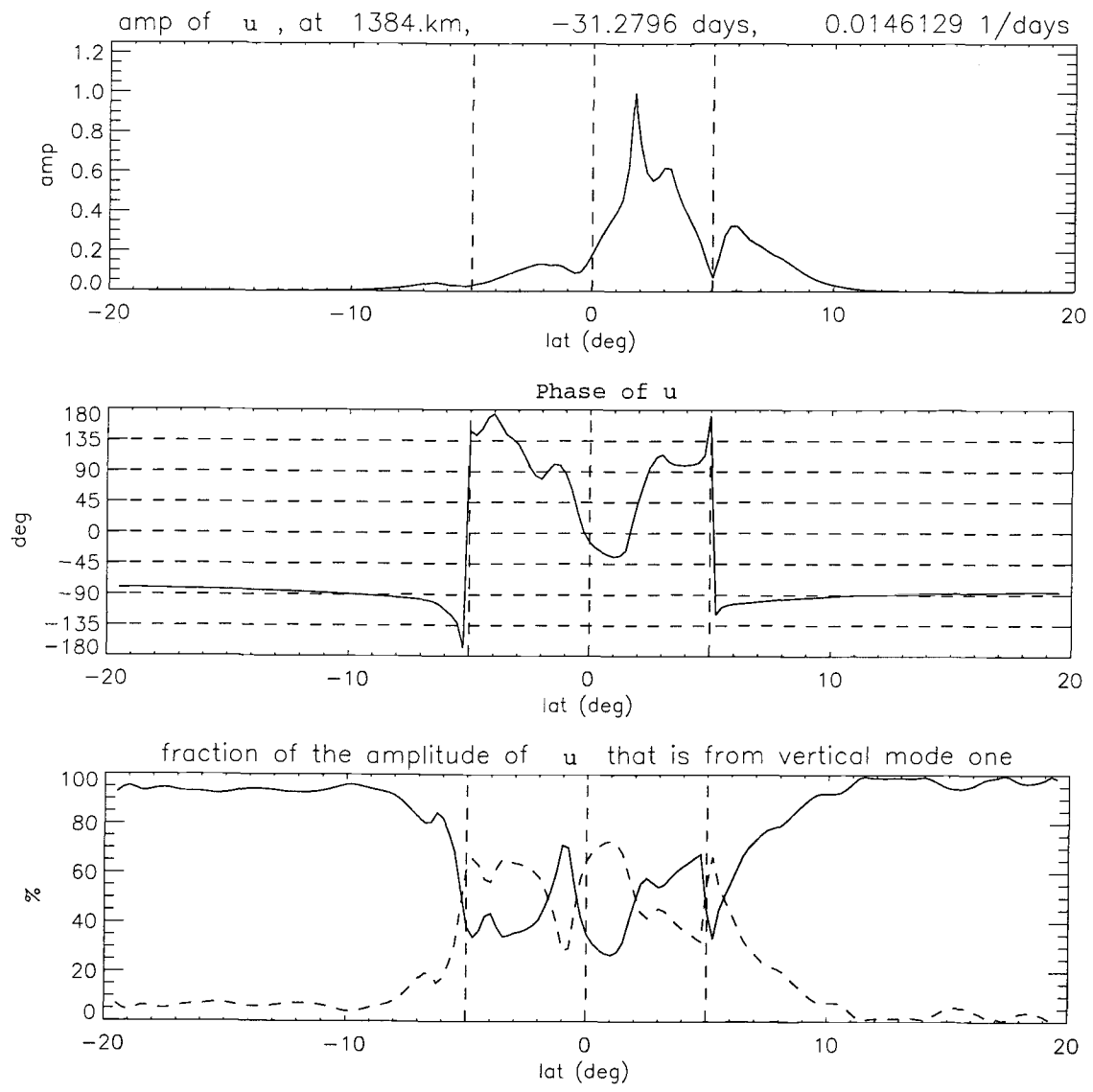
Figure 5.6: The same as Fig. 5.5, except for the eigenfunction of u.
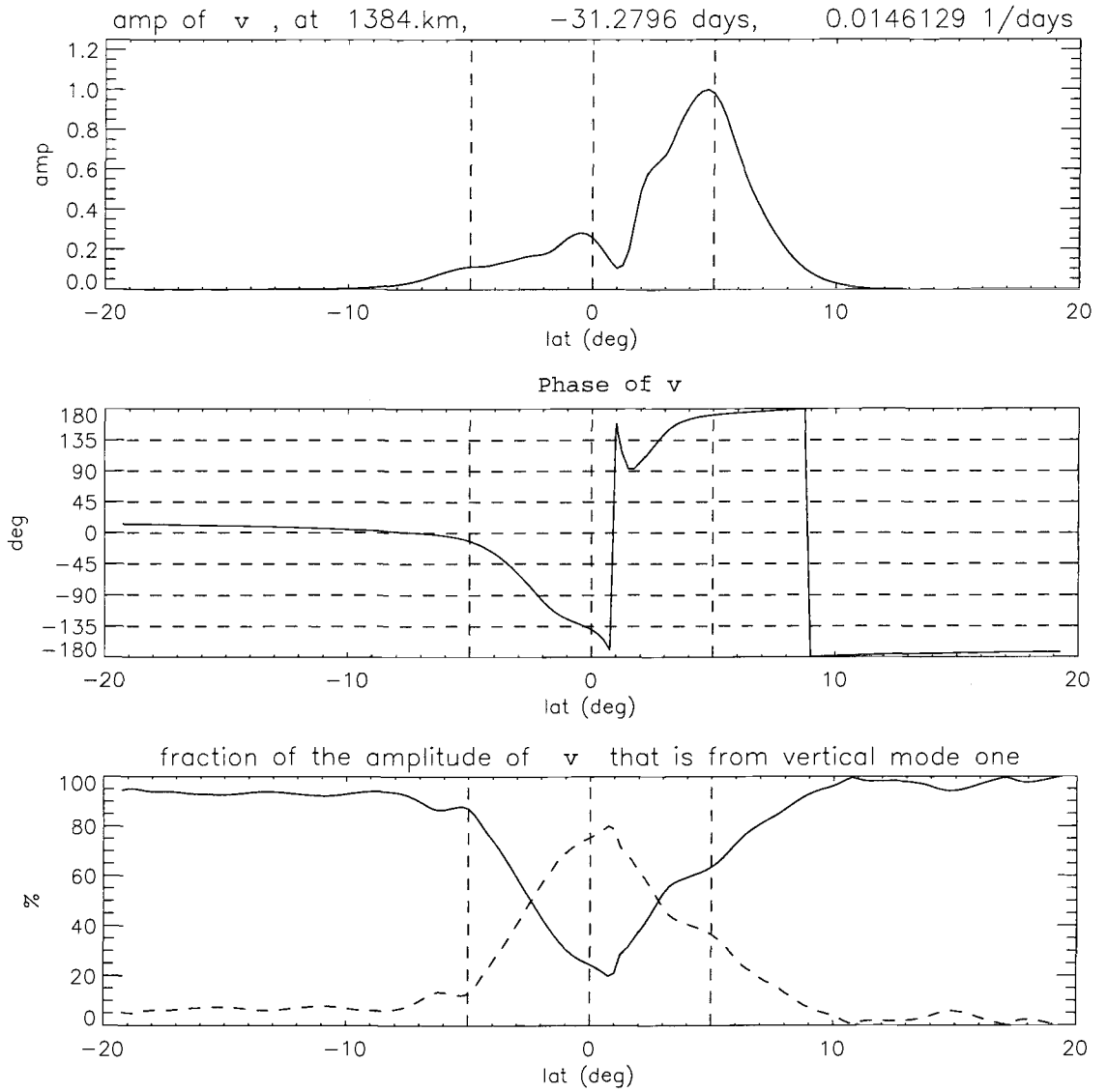
Figure 5.7: The same as Fig. 5.5, except for the eigenfunction of v.

Total production
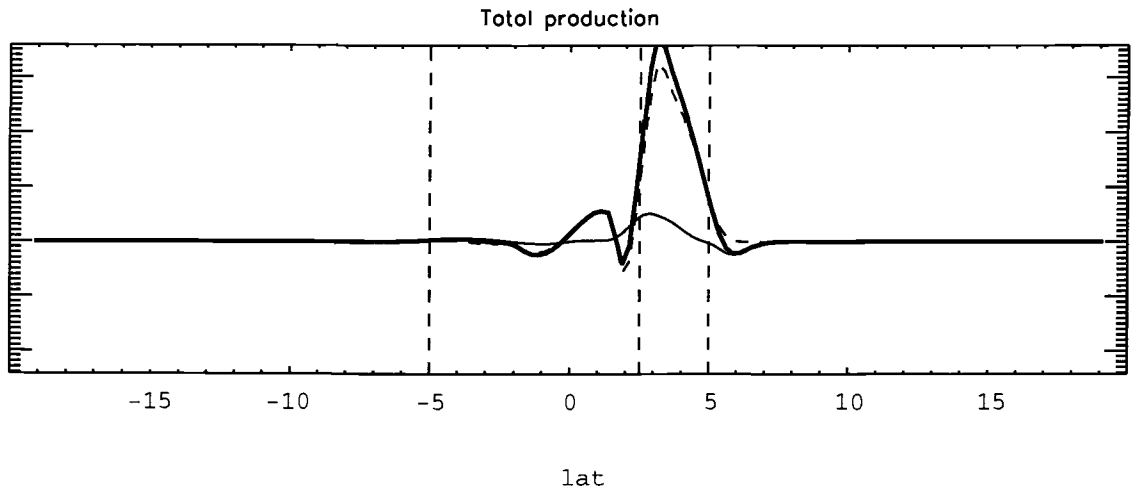
Figure 5.8: The energy conversion from the two-mode projection model for the unaltered mean flow $\overline{U^{(1)}(y)}$ shown in Fig. 5.1. The thick solid line represents the total energy conversion. The thin solid line represents the baroclinic conversion and the dashed line represents the barotopic conversion (see eq. 4.29).

location of most of the energy transfer. Because the region of energy transfer is far from the NECC, the present analysis suggests that the NECC is not crucial to the instability. This is investigated further in chapter 6.

5.4 Five-Mode projection Model

The solutions to the one and two-mode projection models have been shown in sections 5.2 and 5.3, respectively. In the area of wavenumber-frequency space that we are interested in, it was shown that the one-mode model produced stable solutions while the two-mode projection model was able to produce instabilities that are similar to the initial stages of the 1995 TIW season in POCM. It is of interest to determine whether the addition of higher order vertical modes changes the characteristics of the instability. This was investigated by increasing the vertical

resolution of the model to include projection onto the first five baroclinic modes (appendix 7.1). The mean fields for the five-mode projection model were computed over the same time period as the one and two-mode projection models considered previously.

The latitudinal structure of SSH for the fastest growing solution to the five-mode projection model is shown in Fig. 5.9; the dashed lines are the fastest growing solution from the two-mode projection model. There are minor changes in the solution: the e-folding time increases insignificantly from 68 to 73 days and the wavelength increase from 1384 to 1592 km. The latitudinal structures of the eigenvectors are almost identical. The amplitudes in the top panel differ insignificantly at all latitudes; the phases in the second panel differ near the equator by only about 10°. The vertical mode partitioning in the bottom panel is almost wholly made up of the first two baroclinic modes, with higher order modes cumulatively accounting for less than 25% of the variability near the equator.

It is thus apparent that there is not much difference in the meridional structure, vertical structure or dispersion characteristics between the fastest growing solutions in the two and five-mode projection models (Fig. 5.5). The similarity in the solutions between the two and five-mode projection models implies that the import physics of this instability are captured in the two-mode projection model. The analysis in chapter 6 therefore focuses on the results of the two-mode projection model.
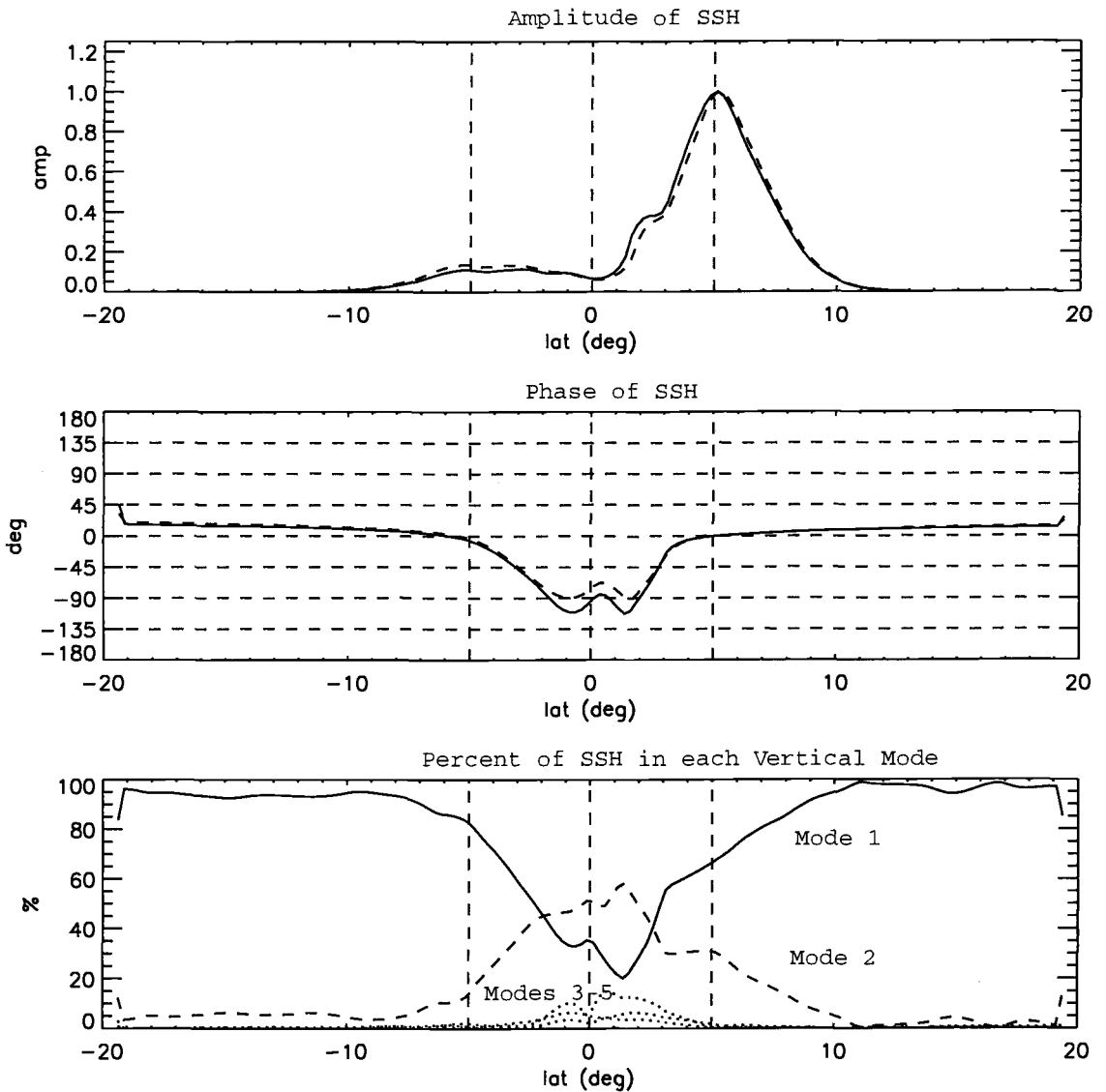
Figure 5.9: The same as Fig. 5.5, except the eigenfunction of SSH for the fastest growing solution to the five-mode projection model. This solution has a e-folding time of 73 days, a period of 32 days and a wavelength of 1592 km. The dashed lines in the top two panels are the solution for the two-mode projection model in Fig. 5.5.

6 SENSITIVITY OF THE TWO-MODE INSTABILITY TO ALTERATIONS IN THE MEAN FIELDS

SSH from the two-mode projection model was shown in section 5.3 to capture most of the features of the TIWs in POCM. However, over the 60-day averaging period of the mean zonal velocity field used in the two-mode projection model, there were substantial variations in the latitudinal structure of the amplitude of SSH associated with TIW variability in POCM, ranging from 3-5 times larger in the north than in the south. Additionally, the phase difference of the TIWs in the north and in the south varied from 0°-45°. These variations can partially be expected because the mean-fields computed from POCM (Fig. 5.1) do not necessarily represent the background mean flow that influence the TIWs in the model. The background mean currents are not constant. They evolve seasonally in response to the varying wind forcing. In addition, the TIWs will inevitably alter the structure of the mean flow as the instabilities extracts energy from the mean flow and the TIWs become non-linear [*Pedlosky*, 1987] (pp. 490-492).

In order to determine what features of the background mean currents are important to the structure and strength of the two-mode instability, elements of the mean background flow were altered. Eight different alterations were made to the mean currents. First, all the currents were increased and decreased both south of the EUC and from the EUC north. Then only the SECN was increased, decreased and shifted north and south. Close attention was paid to how the amplitude, phase, e-folding time, period and wavenumber of the fastest growing solution changed relative to the unaltered solution considered in section 5.3 and the structure of SSH in the POCM model inferred from the wavelet analysis of POCM in section 3.4.

6.1 Altering the currents south of the EUC

The most striking feature in the TOPEX data, the POCM model and in the two-mode instability solutions is the latitudinal asymmetry of the SSH amplitude. The features that control this asymmetry are investigated in the section by increasing and decreasing the mean currents north of EUC (including the EUC) and south of the EUC (excluding the EUC).

When altering the mean fields, it is important that the new current profiles are smooth, minimizing the addition of small-scale variability and shear that is unrealistic. Keeping this in mind, the altered fields were obtained by multiplying the mean current structure by an error function, i.e. the integral of a Gaussian (bottom panels of Figs. 6.2-6.10). The weighting function was produced by integrating the Gaussian,

$$e^{-(\theta - \theta_0)^2/W^2} \tag{6.1}$$

from south to north when the currents were altered in the north and from north to south when the currents were altered in the south: W represents the e-folding scale of the Gaussian, θ_0 is the latitude of the center of the Gaussian and θ in the independent variable, latitude. The maximum value of the error function was set to 0.2, a magnitude that is typical observed fluctuations in the magnitude of $\overline{U_{11}^{(1)}}$ in POCM (see Fig. 6.1). This quantity was added to 1 to increase the currents and subtracted from 1 to decrease the currents. When the currents were altered north of the equator, the Gaussian was centered on the EUC. When the currents were altered in the south, the Gaussian was centered on 2°S. This translation of the error function separated alteration of the EUC from alteration of the SECS.
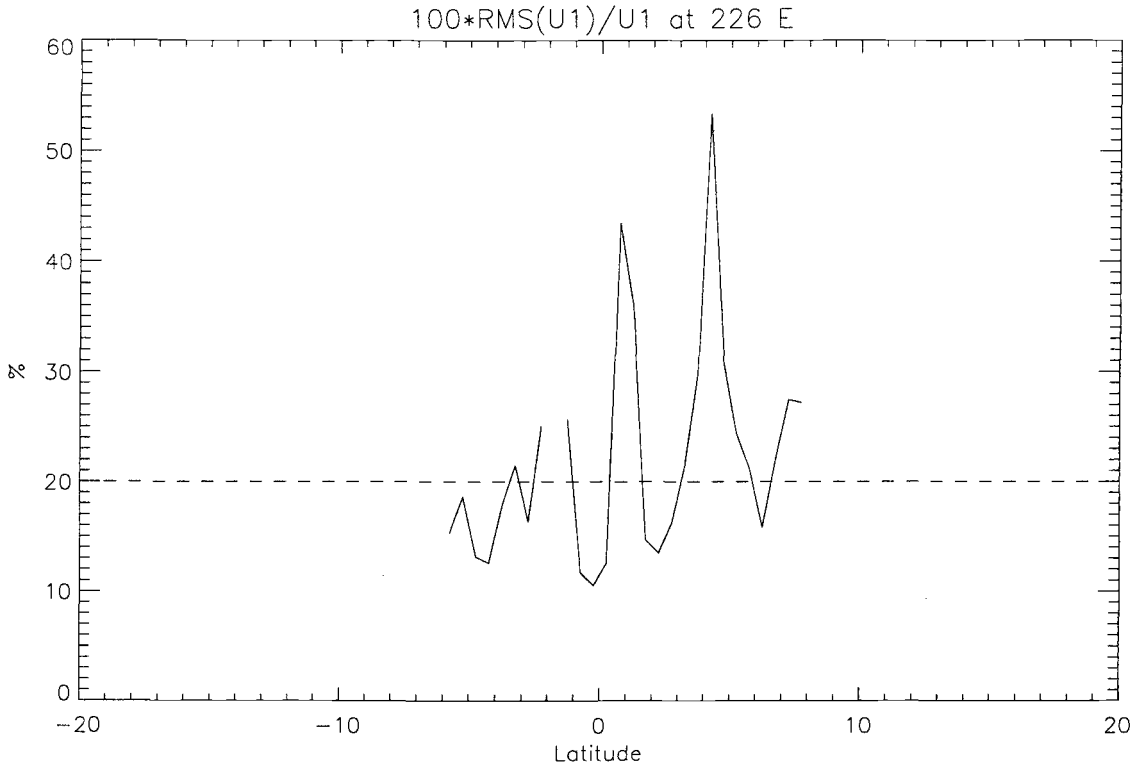
Figure 6.1: The root mean squared variability of $U_{11}^{(1)}(y,t)$ computed during the period from July 8 to September 6, 1995 at 134°W and expressed as a percentage of mean of $\overline{U_{11}^{(1)}}(y)$ computed over the same time period. To avoid singularities, solutions are restricted to where $\overline{U_{11}^{(1)}} \geq 5\frac{cm}{sec}$.

For both cases, W was set equal to 1°, which gave a smooth transition between the regions. The error function and the resulting $\overline{U_{11}^{(1)}}$ profile and shear are shown in Figs. 6.2, 6.3, 6.8 and 6.10.

The mean fields defined in equations (C.1)-(C.6) were altered such that the currents remain in geostrophic balance. Increasing and decreasing the southern mean currents causes only the SECS to change in amplitude, while increasing and decreasing the northern mean currents causes the EUC, SECN and the NECC to change in magnitude.
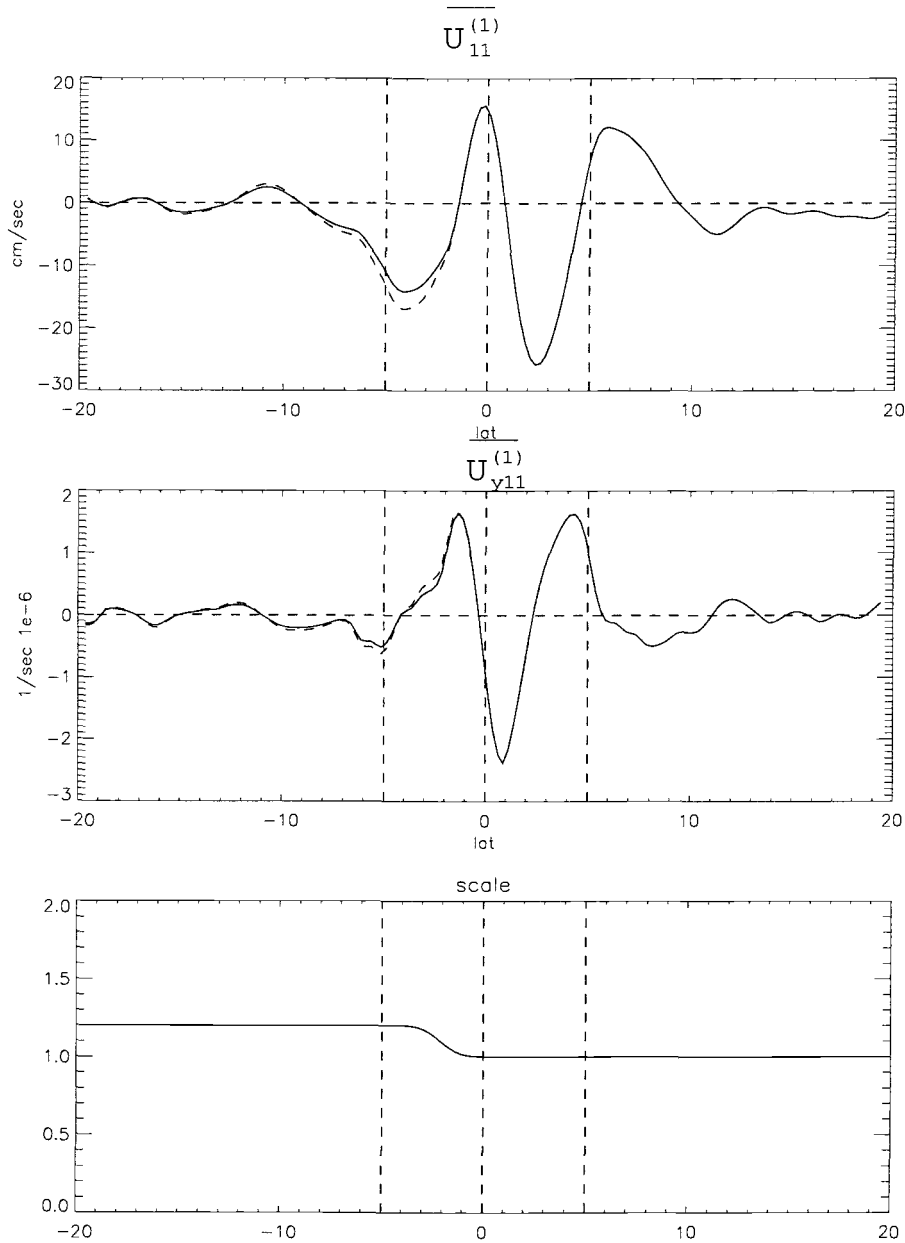
Figure 6.2: The effects of increasing the mean currents in the south. The top panel is a plot of $\overline{U_{11}^{(1)}}$. The middle panel is a plot of the meridional gradient of the top panel. In both of these plots, the solid line represents the unaltered current and the dashed line represents the altered current. The bottom panel is a plot of the scale factor that multiplied the unaltered current to produce the altered current.
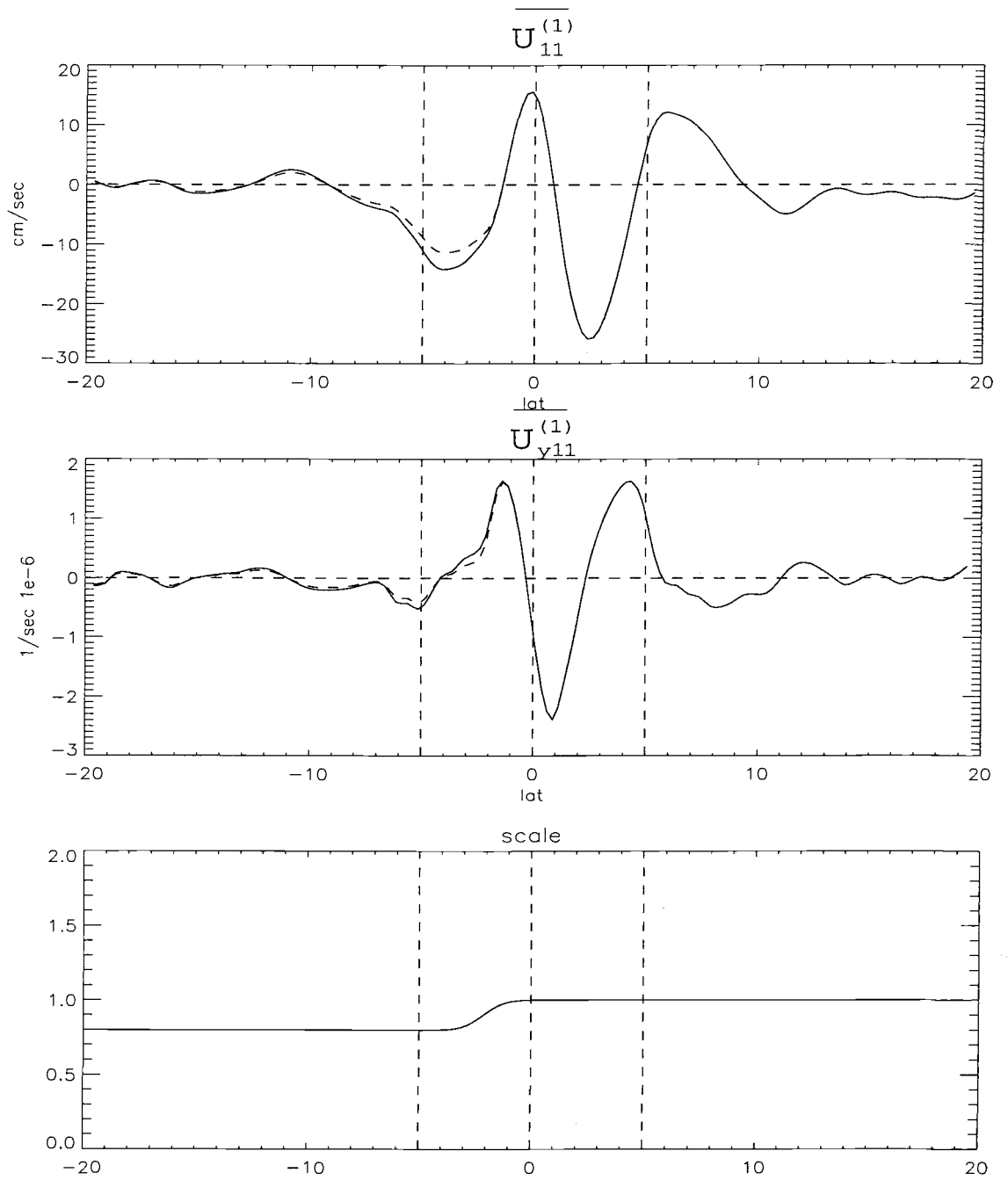
Figure 6.3: The same as Fig. 6.2, except for the effects of decreasing the mean currents in the south.

When the currents are increased or decreased in the south (Fig. 6.2 and 6.3), there is very little change to the eigenvectors or the eigenvalues of the fastest growing mode (Figs. 6.4 and 6.5). The amplitude of SSH for both cases are essentially unchanged from the unaltered case. The wavelength is the same for all three cases, within the resolution of the analysis. The period and e-folding time change by insignificant amounts. The only noticeable changes are small changes in the phase. The phase lags the unaltered case in the south by a few degrees when the currents are increased and leads by a similar amount when the currents are decreased.

The magnitude of these alteration are reasonable estimates of the range of variations of the SECS [*Johnson et al.*, 2002]. The insensitivity of the e-folding time to the changes in the mean fields south of the EUC should be expected. As shown in Fig. 5.8, the majority of the energy production occurs in the north. It is surprising, however, that altering the currents in the south has such a small affect on the meridional structure of the amplitude and phase of TIWs.

The extreme case of effectively eliminating all the flow in the south determines whether the SECS has an effect on the latitudinal structure of the unstable solution. For this purpose, the weighting function used to eliminate the currents in the south had a minimum value of 0.1 and was centered on the EUC rather than 2°S (Fig. 6.6). This was done to maximize the possible effects of the southern current structure. Surprisingly, removing the SECS had no effect on the amplitude structure of SSH (Fig. 6.7). There was also no change in the wavelength, period and e-folding time of the fastest growing mode. The only significant change is that

Figure 6.4: The same as Fig. 5.9, except for the latitudinal structure of SSH for the fastest growing solution to the two-mode projection model with the currents in the south increased by 20% (see Fig. 6.2). This solution has an e-folding time of 69 days, a period of 31 days and a wavelength of 1384 km.

Figure 6.5: The same as Fig. 6.4, except for the latitudinal structure of SSH for the fastest growing solution to the two-mode projection model with the currents in the south decreased by 20% (see Fig. 6.3). This solution has an e-folding time of 69 days, a period of 31 days and a wavelength of 1384 km.

the phase south of the equator systematically increased by about 20° relative to the unaltered case.

6.2   Altering the currents north of the EUC

In contrast to the minor influence of the currents south of the equator on the unstable eigensolutions, altering the mean structure of the northern currents, where the energy transfer is large, significantly affects the fastest growing solutions. Increasing the currents in the north (Fig. 6.8) produced somewhat faster growing instabilities with e-folding times of 48 days compared to 68 days from the unaltered case (see Fig. 6.9). The wavelength and period of the instability changed by small amounts to 1448 days and 30.5 days, respectively. Although faster growing, there was very little change in the meridional structure of the instability. The largest difference occurred in the phase structure south of the shear between the EUC and the SECN. In comparison to alterations in the currents south of the equator, these phase differences are large, on the same order as the phase difference when the currents south of the equator were completely eliminated.

Decreasing the currents north of the equator (Fig. 6.10) caused the fastest growing solution to become more stable, with an increased e-folding time of 104 days, and shortened the period of the wave to 30.5 days and the wavelength to 1192 km (see Fig. 6.11). The reduced shear in the north had an unexpected effect on the meridional structure of the instability. As the instability became more stable, its meridional structure became more similar to that obtained for the stable M1 Rossby wave from the one-mode projection model considered in section 5.2. This change can be seen in all three panels of Fig. 6.11: the amplitude increased in the

Figure 6.6: The same as Fig. 6.2, except for the effects of eliminating the currents.

Figure 6.7: The same as Fig. 6.4, except for the latitudinal structure of SSH for the fastest growing solution to the two-mode projection model with currents south of the equator eliminated. This solution has an e-folding time of 69 days, a period of 31 days and a wavelength of 1384 km.

Figure 6.8: The same as Fig. 6.2, except for the effects of increasing currents in the north.
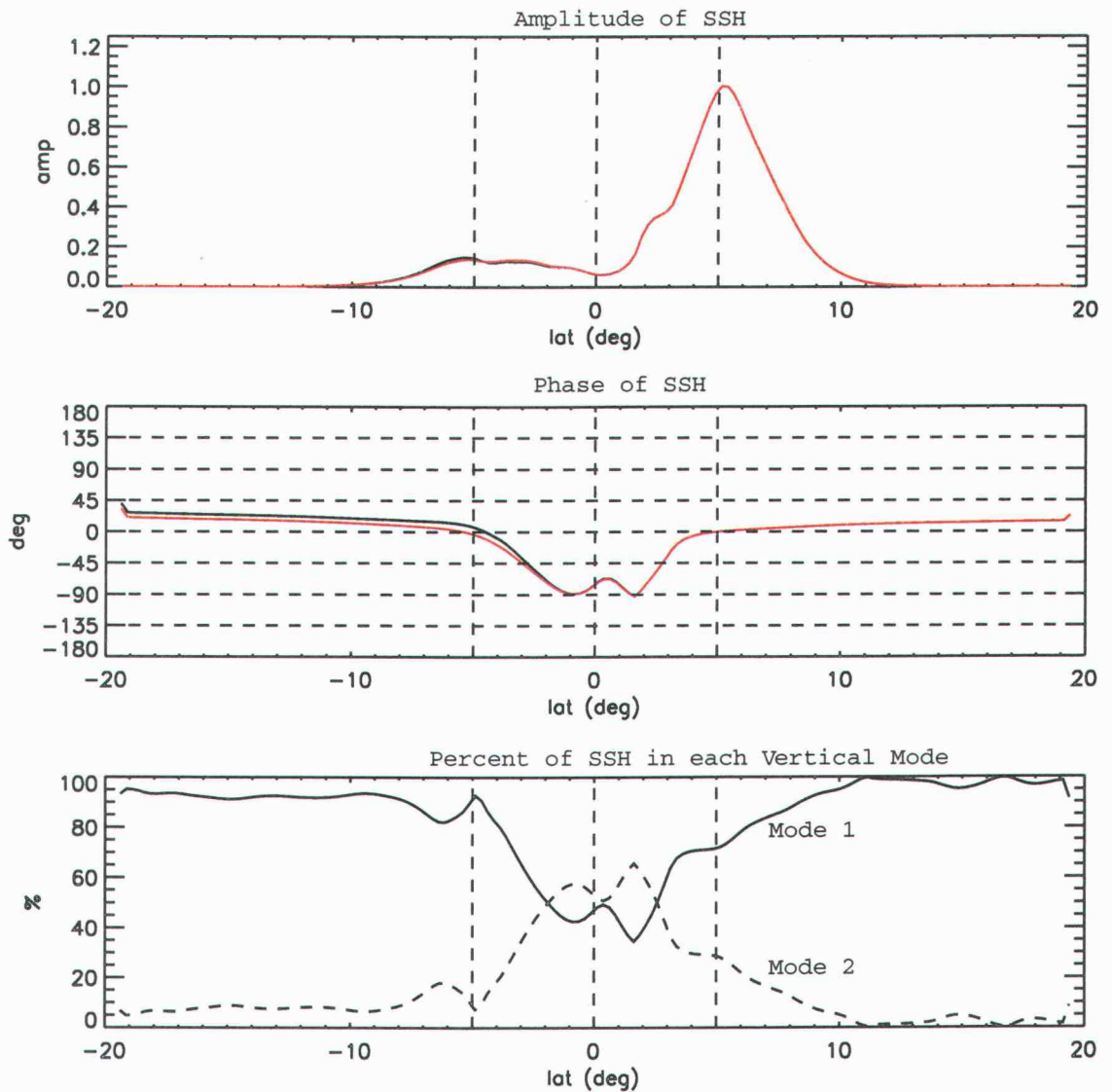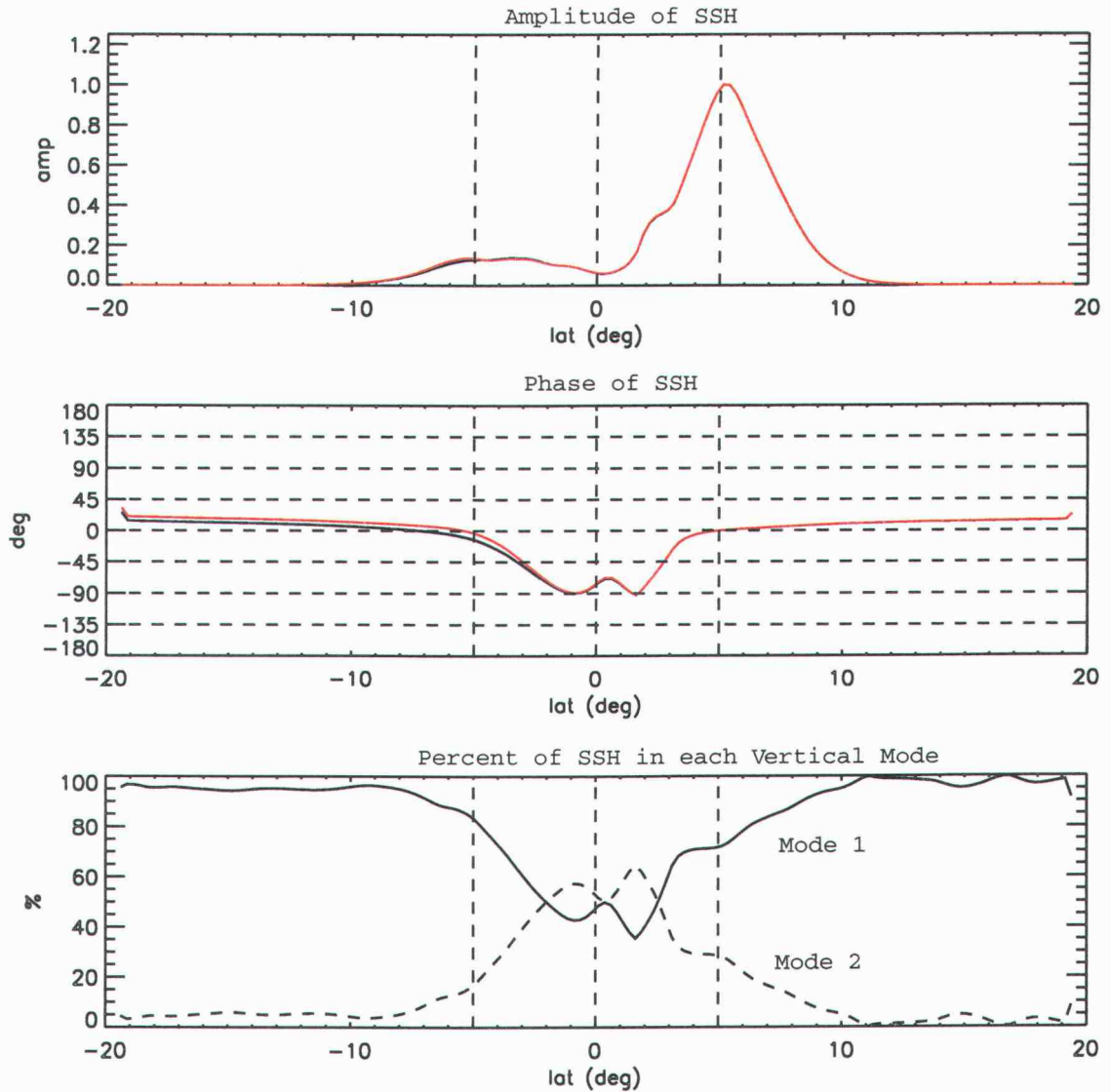
Figure 6.9: The same as Fig. 6.4, except for the latitudinal structure of SSH for the fastest growing solution to the two-mode projection model with the currents in the north increased by 20%. This solution has an e-folding time of 48 days, a period of 30.5 days and a wavelength of 1448 km.

south (top panel), the latitudinal variations in phases decreased (middle panel), and the variability becomes mostly vertical mode one (the bottom panel).

The larger amplitude in the south seen here is surprising, given that the alteration to the SECS had almost no effect on the amplitude in the south. It will be shown later in chapter 7 that, in the low wavenumber limit, the instability is created from a resonance between the first baroclinic mode M1 Rossby wave and an altered second baroclinic mode M2 Rossby wave. The reduction in meridional shear reduces the instability and moves the solution closer to the high wavenumber resonance point where the meridional structure resembles the M1 Rossby wave.

6.3   Altercating the SECN

It was shown in section 6.2 that altering the currents in the north causes large changes in the structure of the unstable wave solutions. It was also shown in section 5.3 that the majority of the energy transfer occurs near the maximum of the SECN. For these reasons, the effects of increasing, decreasing and shifting the SECN in isolation are examined in detail in this section.

The same Gaussian function (eq. 6.1) used to create the weighting functions in sections 6.1-6.2 was used to alter only the SECN. In this case, the Gaussian had an amplitude of 0.2, θ_0 was set to the center of the SECN and the width, W, was 2°, which localized the alterations of the SECN and associated shears but did not change the location of the shears. This Gaussian was either added to 1 to increase the SECN, or subtracted from 1 to decreased the SECN. The results were multiplied by the mean fields to produce changes in the SECN with similar
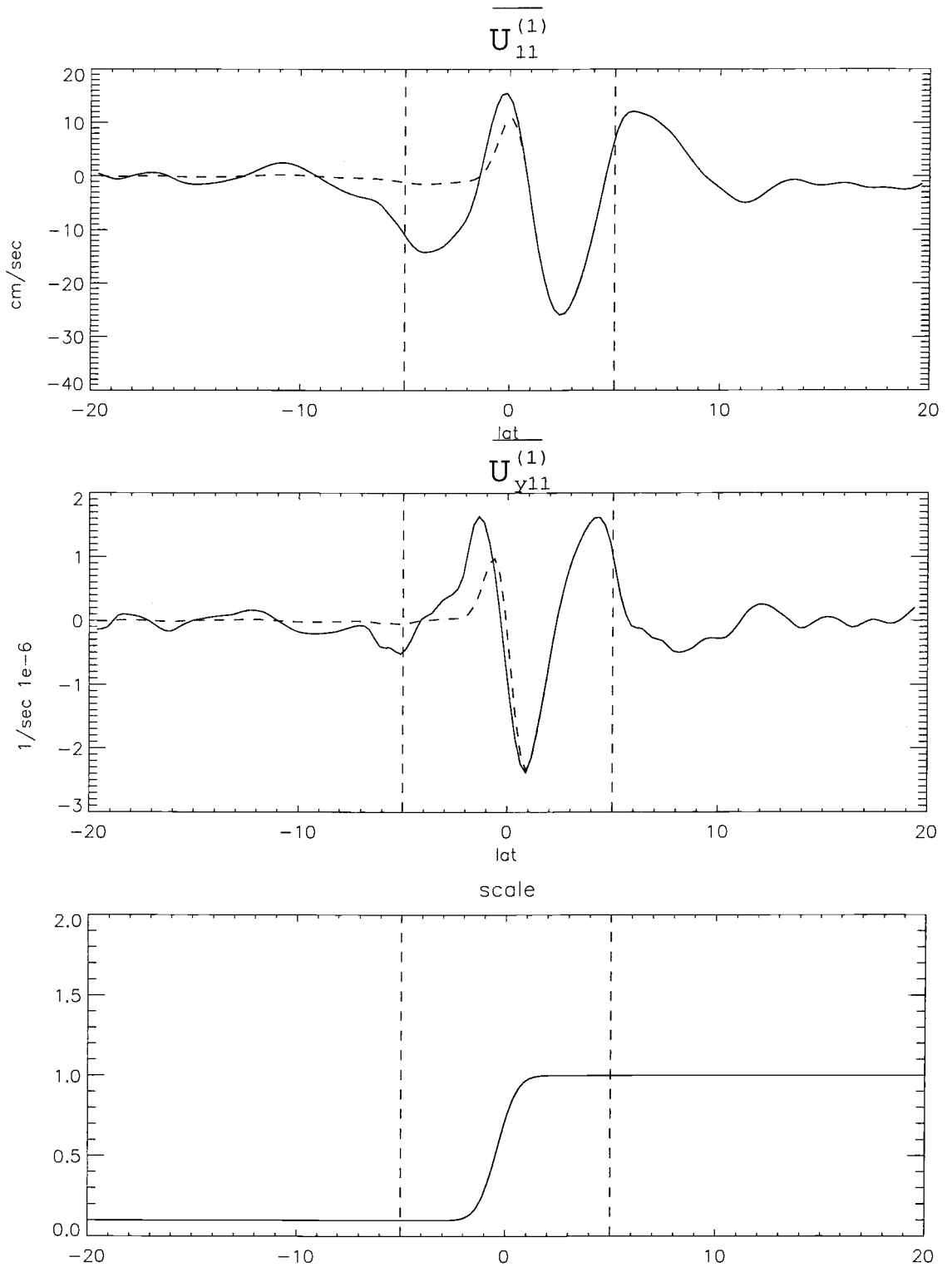
Figure 6.10: The same as Fig. 6.2, except for the effects of increasing the currents in the north.
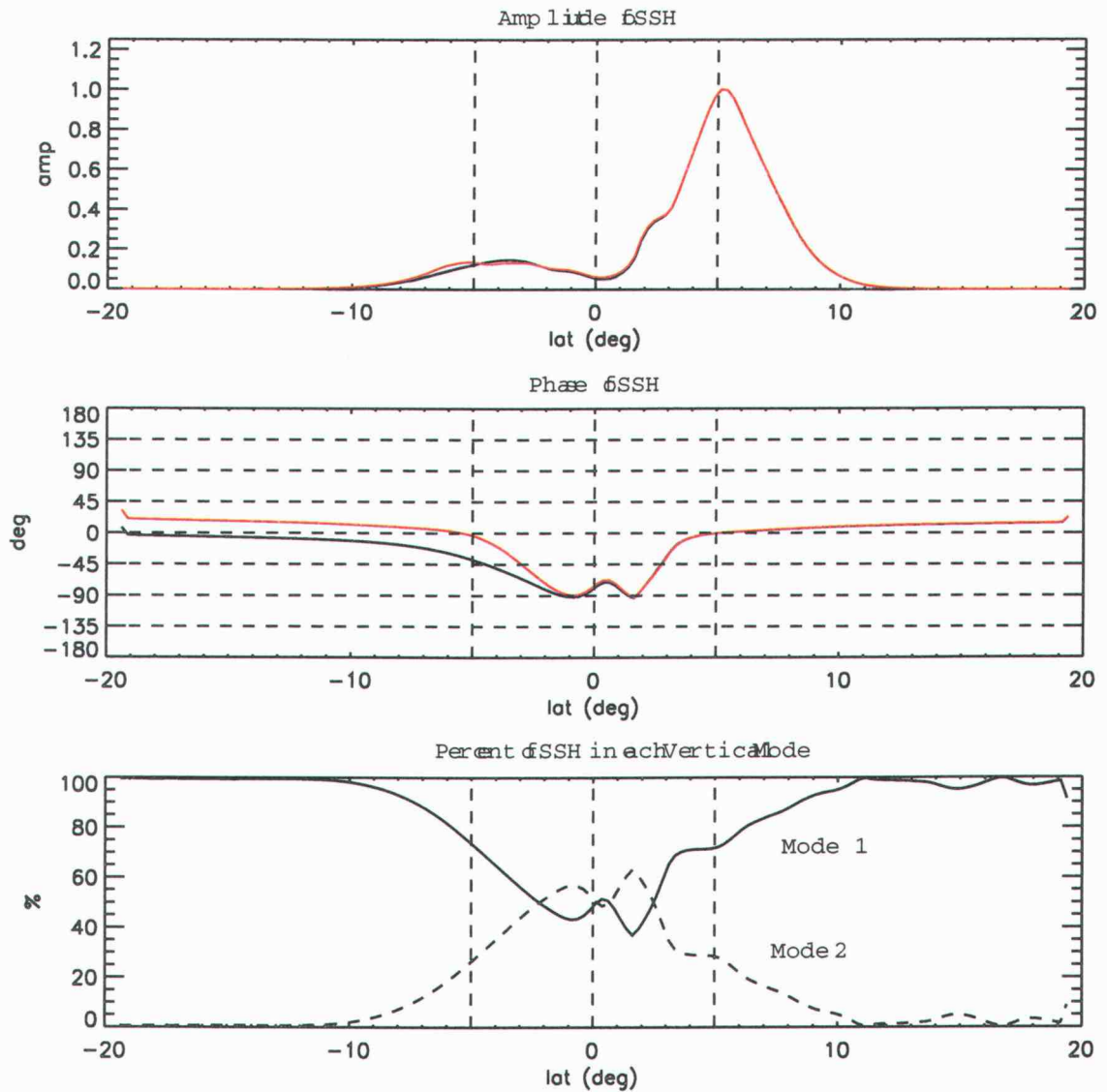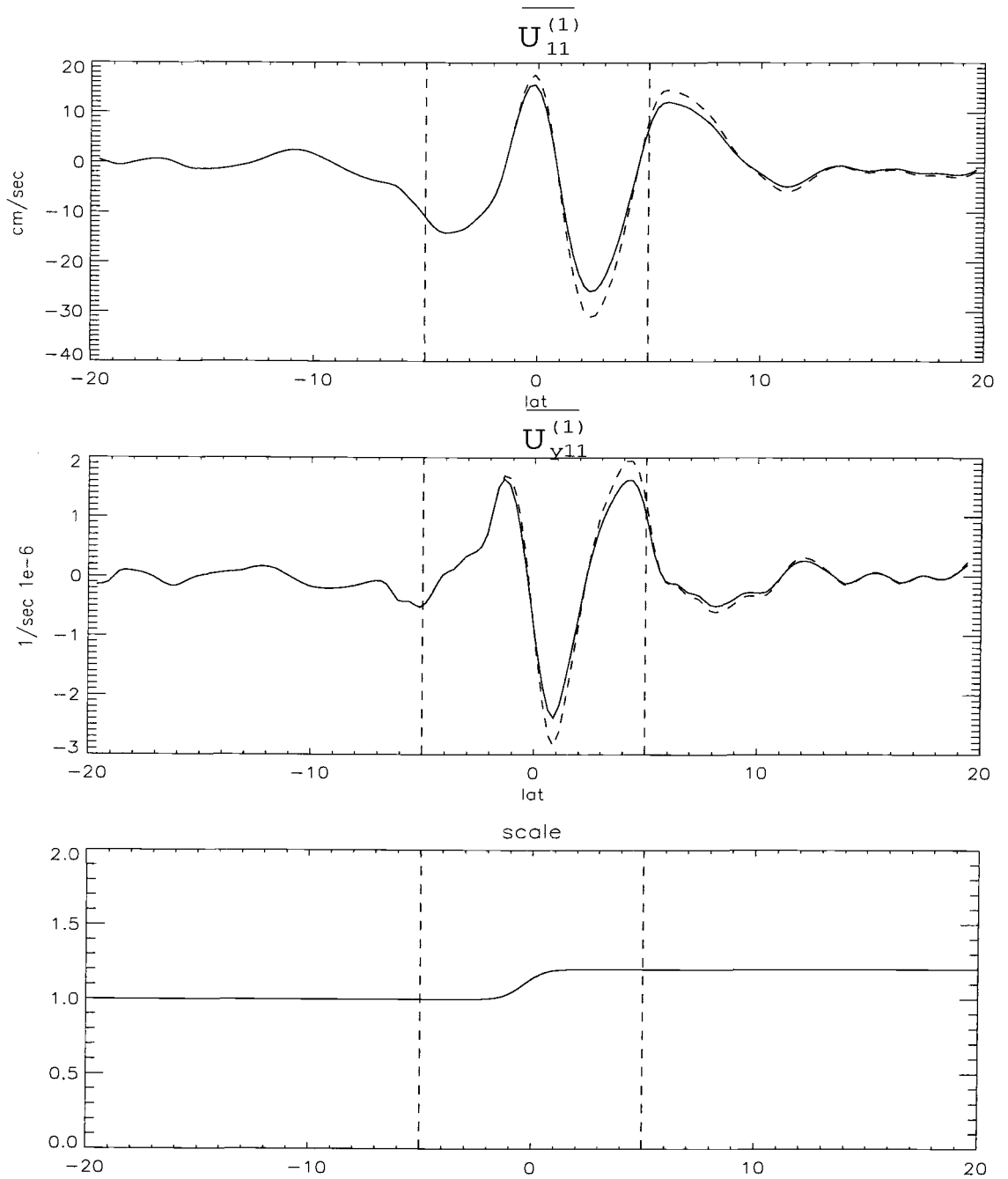
Figure 6.11: The same as Fig. 6.4, except for the latitudinal structure of SSH for the fastest growing solution to the two-mode projection model with the currents in the north decreased by 20%. This solution has an e-folding time of 104 days, a period of 30.5 days and a wavelength of 1192 km.

magnitude to the previous alterations of the northern currents (Figs. 6.12 and 6.13).

Increasing and decreasing the SECN had similar effects to increasing the currents north of the equator (Figs. 6.14 and 6.15). The most noticeable differences between the two cases were in the eigenvalues. Increasing the SECN produced a fastest growing solution with a short e-folding time of 36 days, a period of 28.6 days and a wavelength of 1352 km. This is more unstable than the case where all the currents in the north were increased. Decreasing the SECN produced a fastest growing solution that was more stable than the case when all the currents in the north were decreased, increasing the e-folding time to 171 days with an associated period and wavelength of 30.3 days and 1240 km. These 20% alterations of the SECN thus determine whether or not the solution is essentially stable or unstable.

The changes in the stability of the solutions are also reflected in the meridional structure of the phase. Increasing the SECN causes the phase to lag more at southern latitudes (second panel of Fig. 6.14) compared with the case where all of the northern currents are increased(second panel of Fig. 6.9). Decreasing the SECN has the opposite effect, producing less phase lag at low latitudes (second panel of Fig. 6.15) compared with the case when all of the currents are decreased (second panel of Fig. 6.11). The solution with the decreased SECN also has a greater amount of the variability in first baroclinic mode (bottom panel of Fig. 6.15) compared with the case when all the currents in the north were decreased.

To further investigate its importance to the stability of the solution, the SECN was shifted north and south by 0.25°. So as not to alter the latitudinal structure of the shear at the same time (except for the latitudinal shifts), the north side of
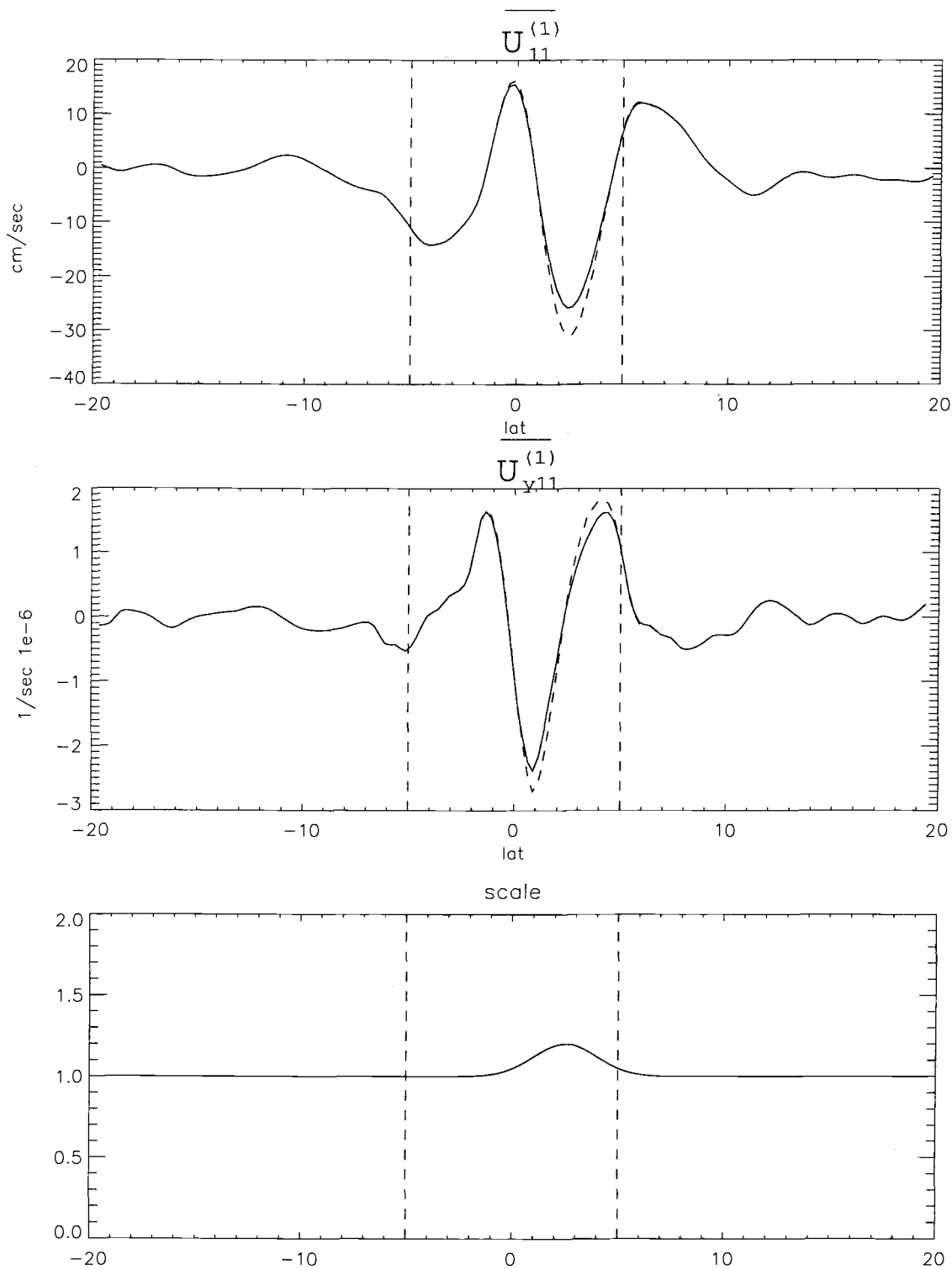
Figure 6.12: The same as Fig. 6.2, except for the effects of increasing the SECN.
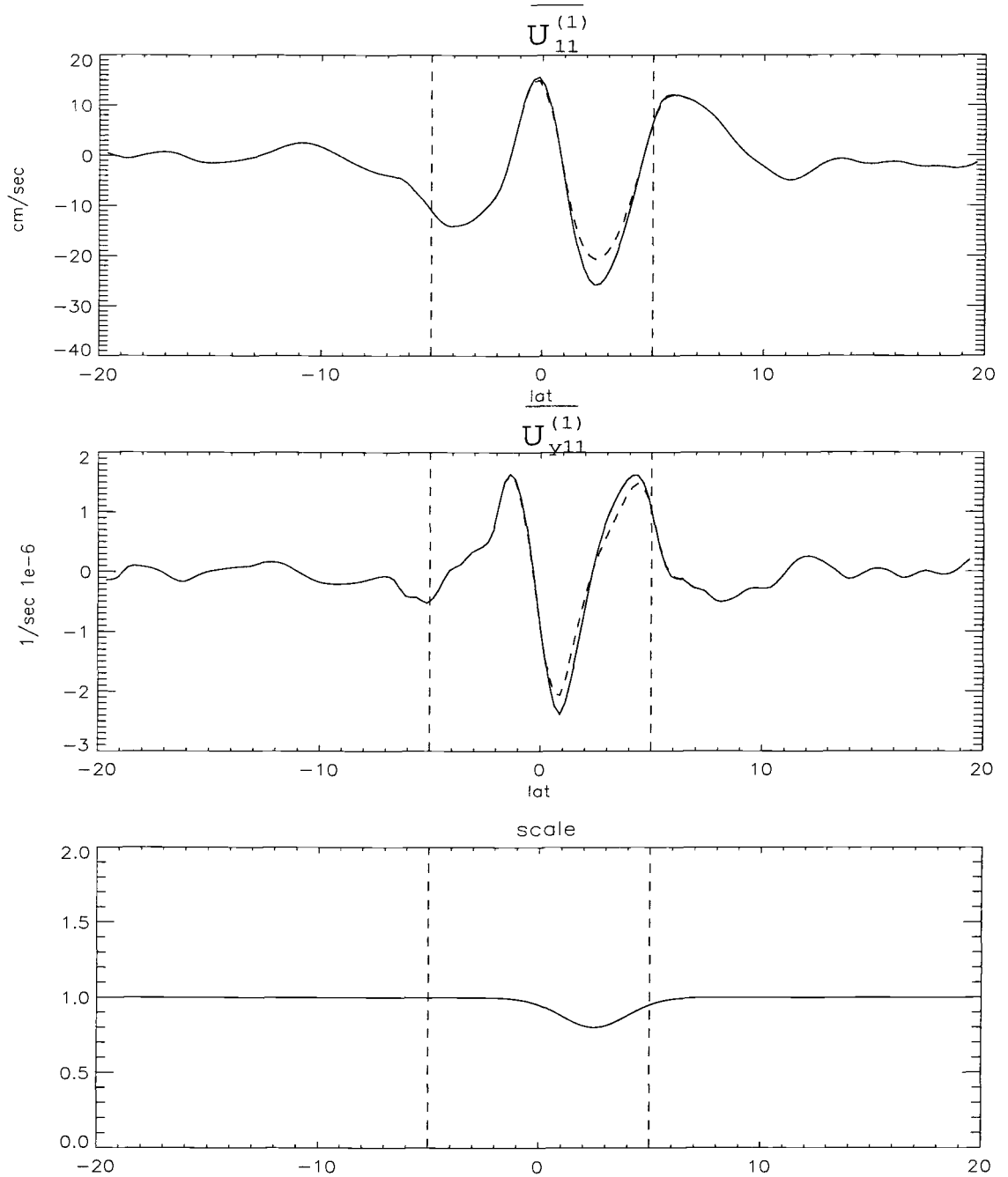
Figure 6.13: The same as Fig. 6.2, except for the effects of decreasing the SECN is decreased.
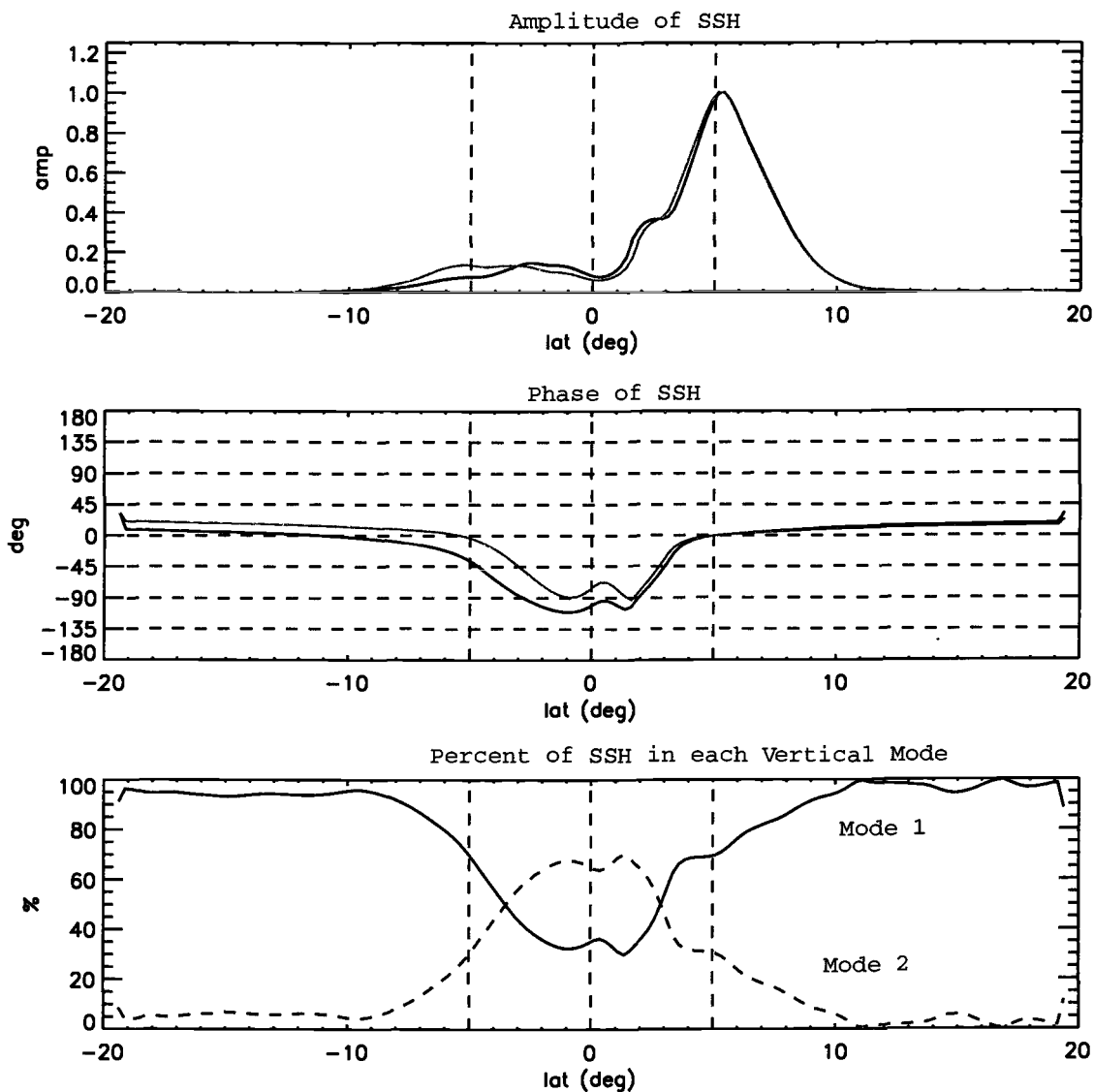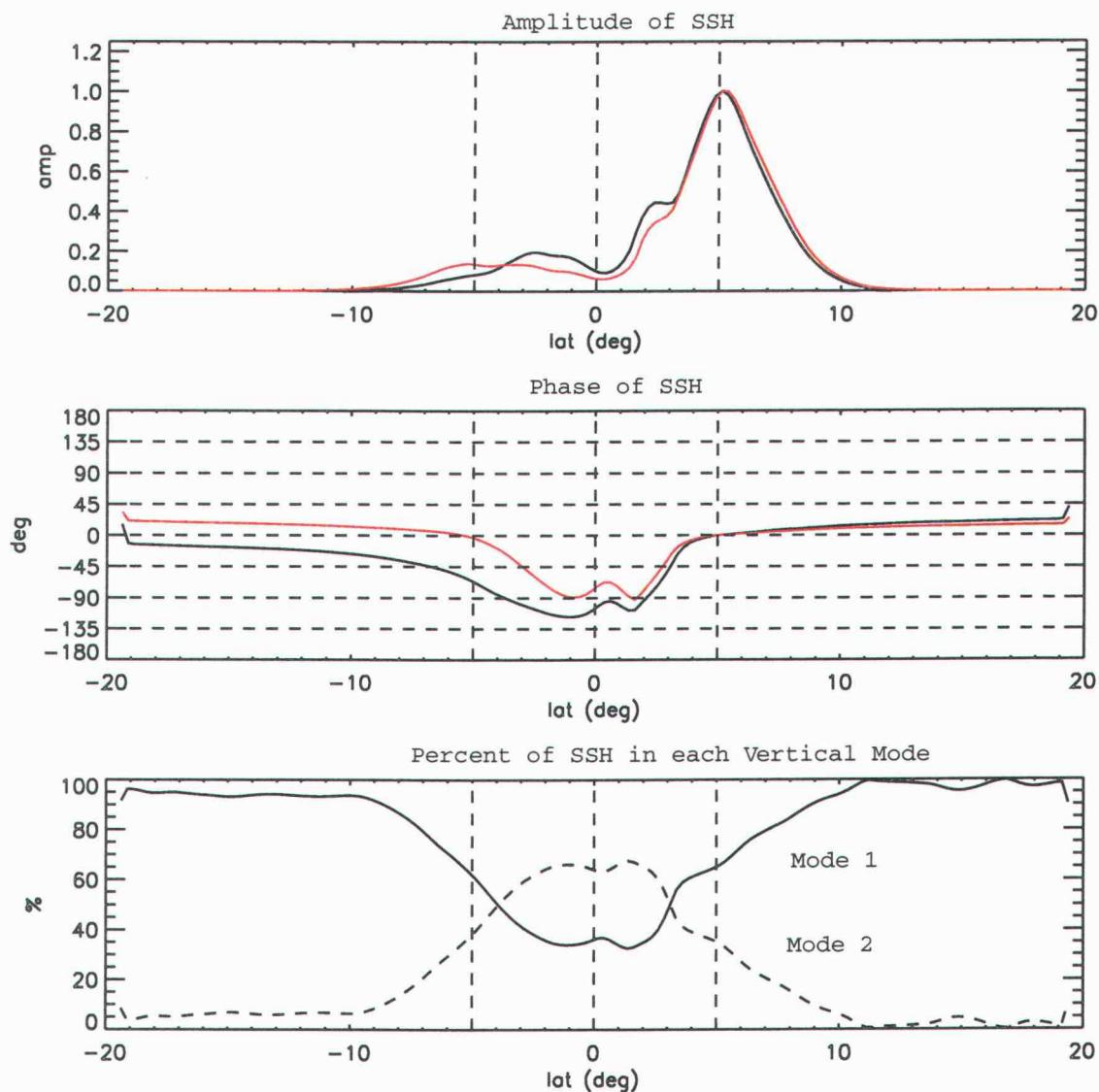
Figure 6.14: The same as Fig. 6.4, except for the latitudinal structure of SSH for the fastest growing solution to the two-mode projection model with only the SECN increased by 20%. This solution has an e-folding time of 36 days, a period of 29 days and a wavelength of 1352 km.
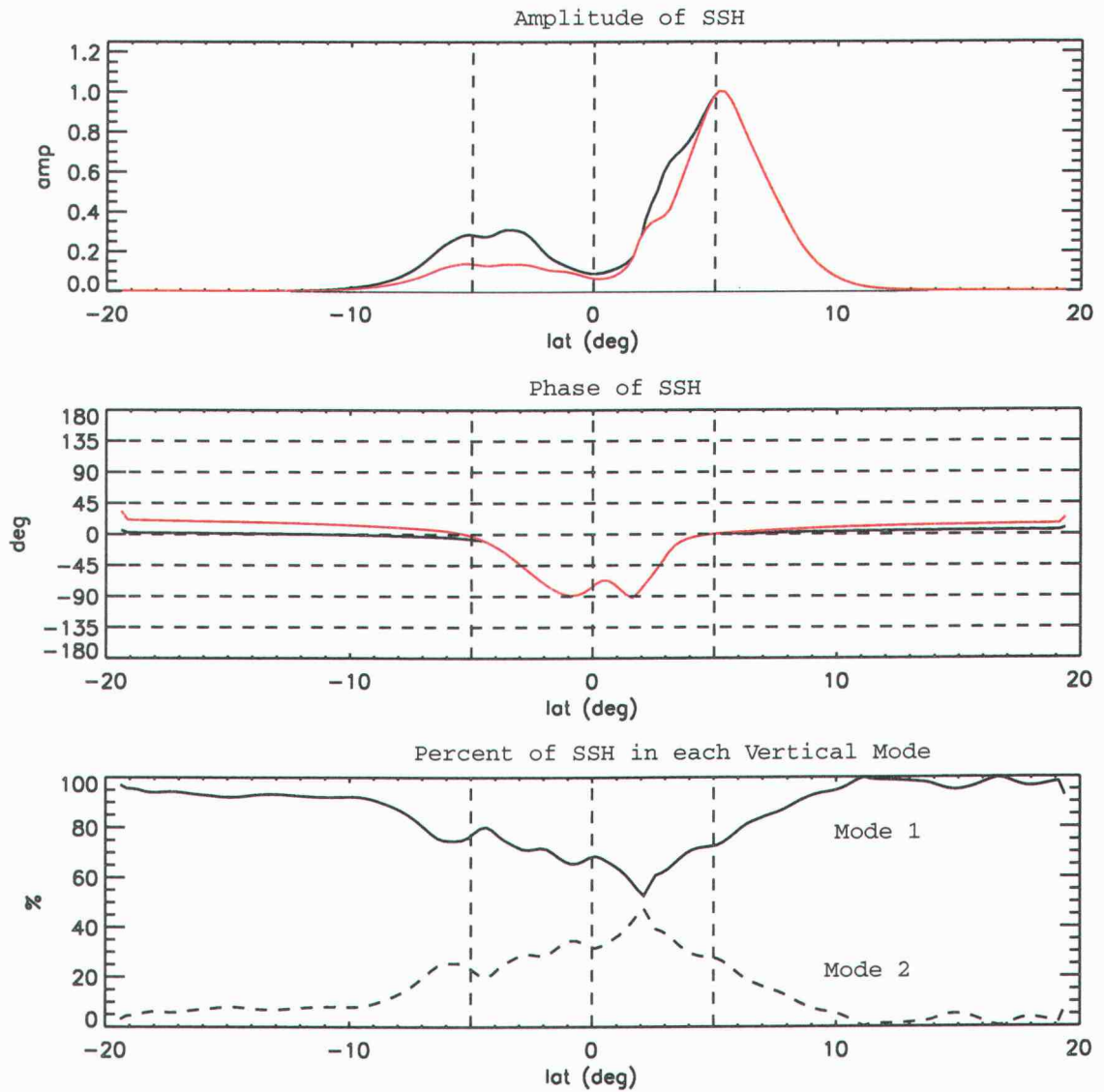
Figure 6.15: The same as Fig. 6.4, except for the latitudinal structure of SSH for the fastest growing solution to the two-mode projection model with only the SECN decreased by 20%. This solution has an e-folding time of 171 days, a period of 30 days and a wavelength of 1240 km.

EUC and south side of the NECC were broadened or sharpened as required. For the 0.25° shifts considered here, these effects are small (Figs. 6.16 and 6.17).

The effects of latitudinal shifts if the SECN produced small but not negligible changes in the solutions. Shifting the SECN 0.25° to the north caused the solution to become more stable, increasing the e-folding time from 68 to 96 days. Shifting the SECN to the south produced solutions that were somewhat more unstable, decreasing the e-folding time from 68 to 58 days. The period and wavenumber of the fastest growing solution changed by small amounts, increasing to 33 days and 1480 km when the SECN was shifted north and decreasing to 30 days and 1336 km when the SECN was shifted south.

As in the other sensitivity studies, the phase lag at low latitudes changed when the solutions became more or less unstable. Shifts to the south increased the phase lag (Fig. 6.19), while shifts to the north decreased phase lag (Fig. 6.18). The vertical structure of the more stable solutions was represented by a higher percent of variance in the first baroclinic mode than the second baroclinic mode, similar to the case when the SECN was decreased. Although latitudinal shifts of the SECN altered the meridional structure of the phase, there was almost no change in the meridional structure of the amplitude.

6.4   Summary of Alteration

Slight alterations to the current system have been shown to alter the e-folding time, dispersion characteristics and meridional structure of the instability. Increasing or decreasing the SECN by only 20% produced SSH amplitudes ranging from 3 to 5 times larger in the north than in the south, phase lags in SSH between the
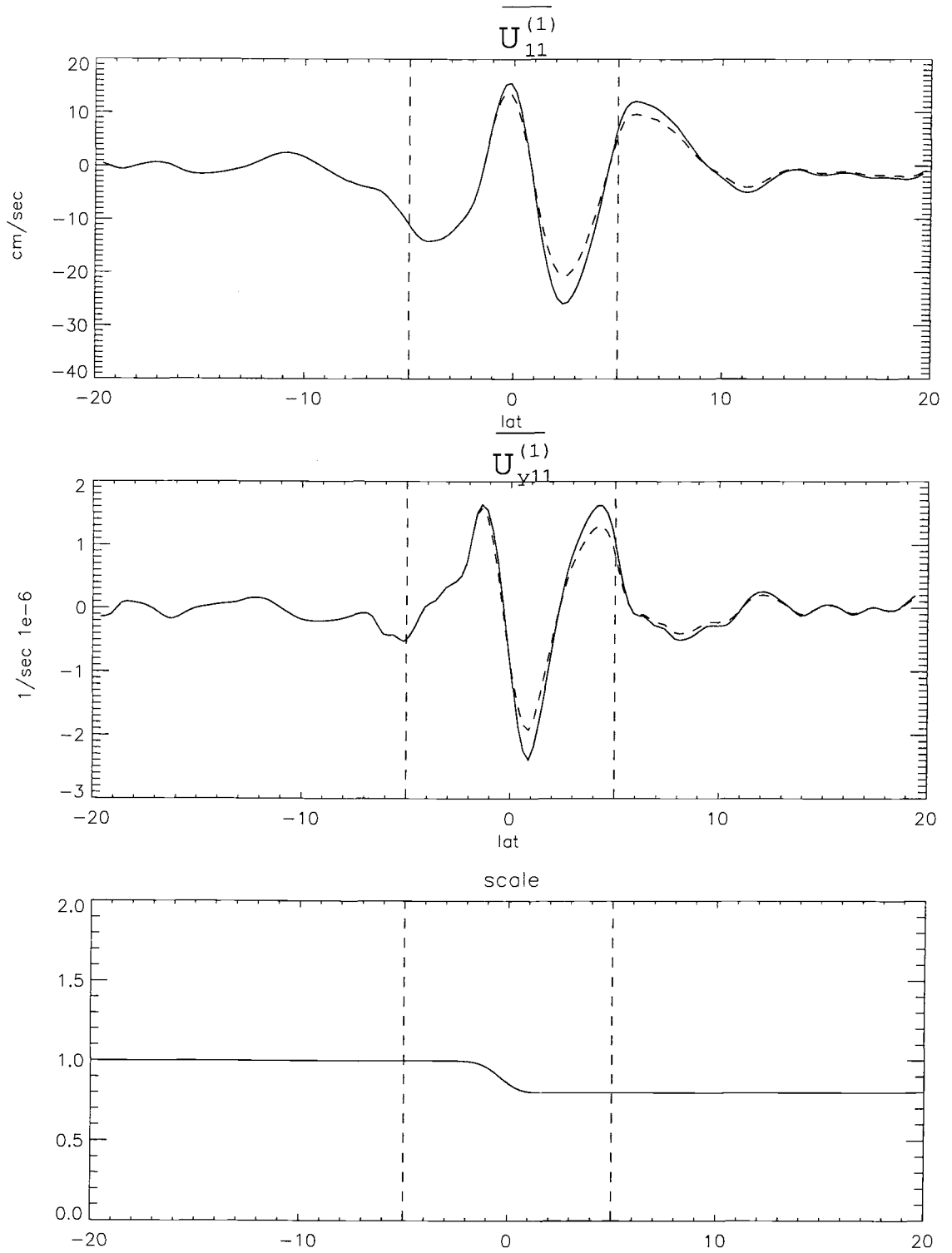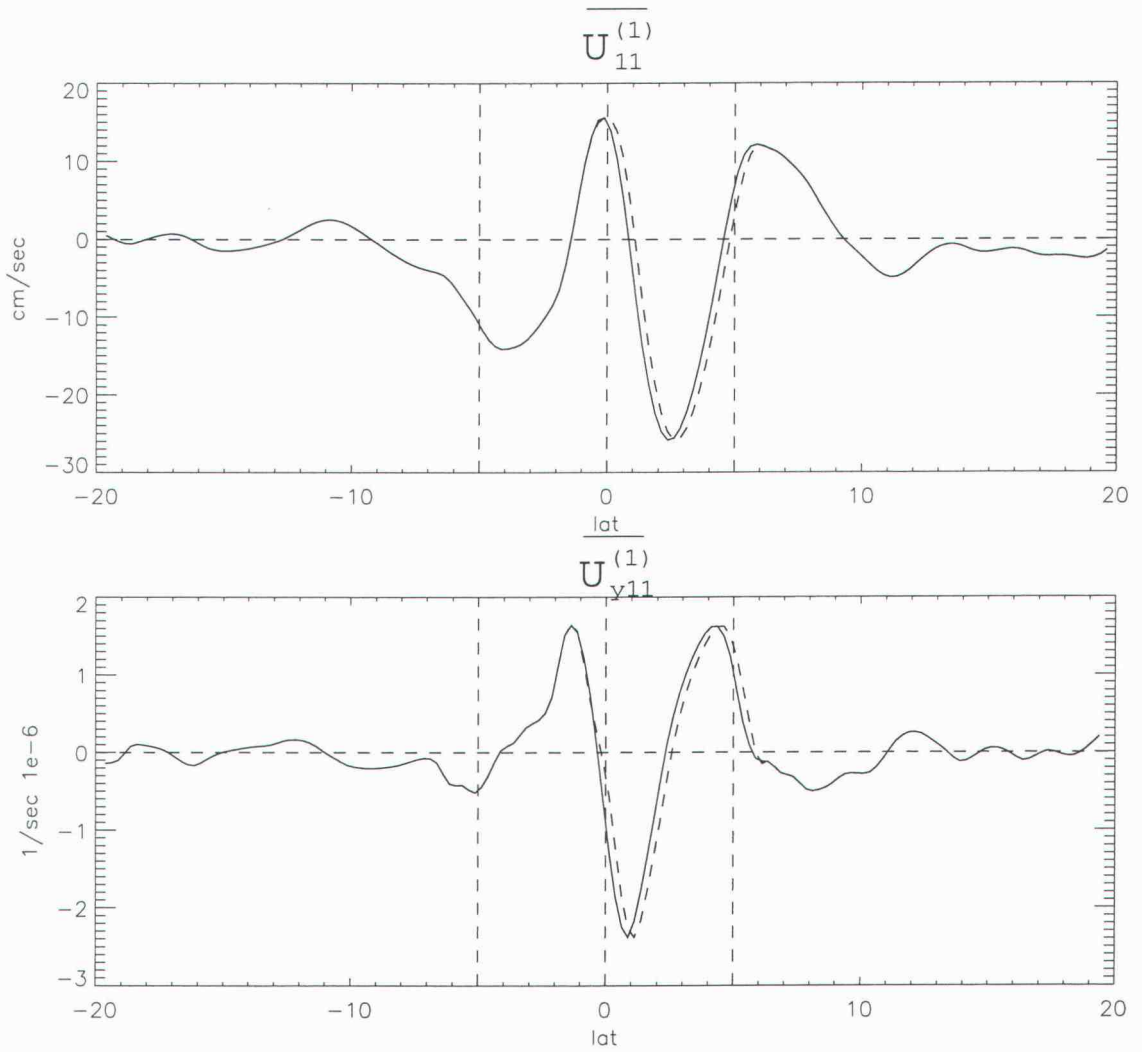
Figure 6.16: The same as Fig. 6.2, except for the effects of shifting the SECN 0.25° to the north.
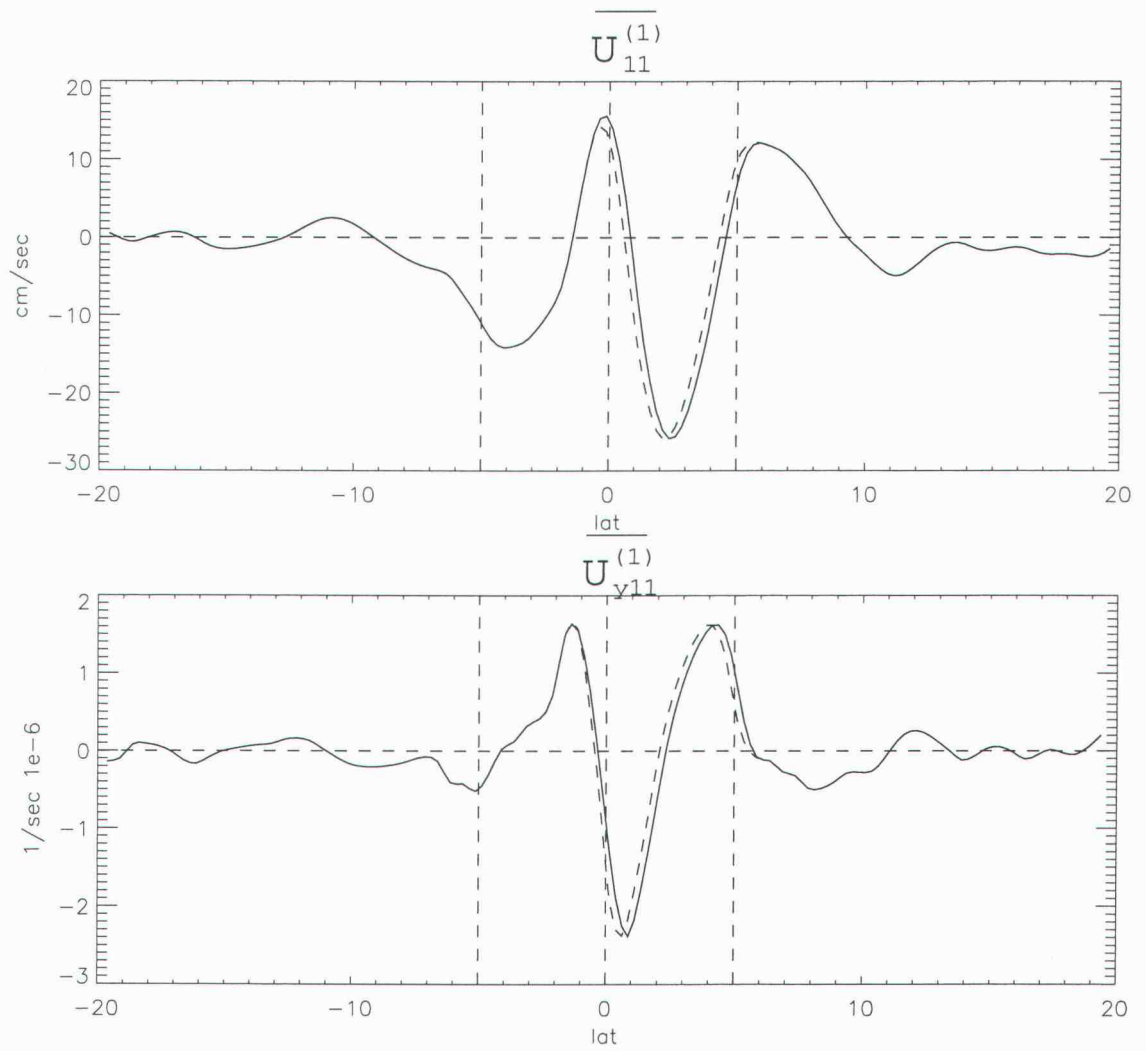
Figure 6.17: The same as Fig. 6.2, except for the effects of shifting the SECN 0.25° to the south.
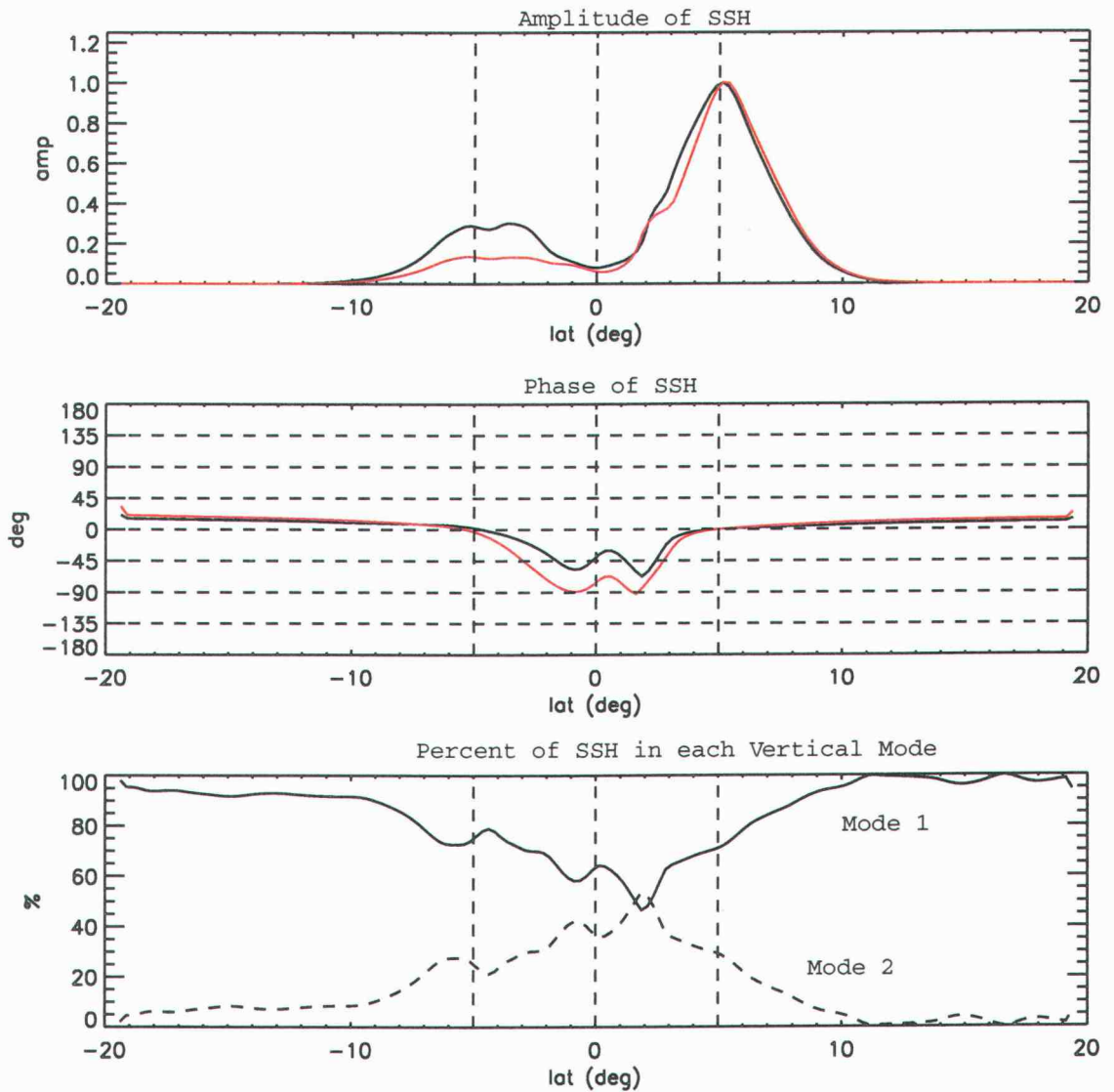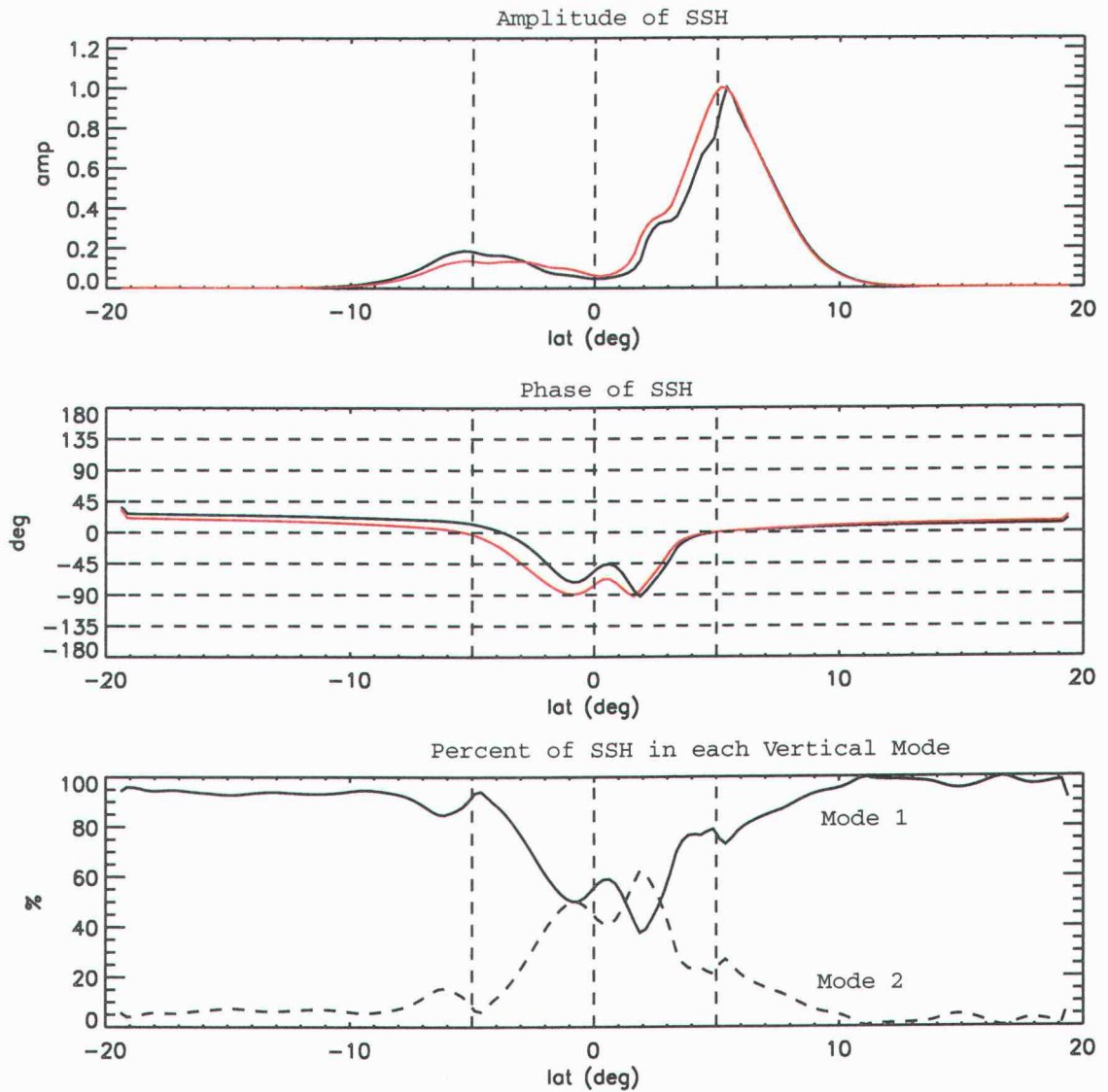
Figure 6.18: The same as Fig. 6.4, except for the latitudinal structure of SSH for the fastest growing solution to the two-mode projection model with the SECN shifted 0.25° to the north. This solution has an e-folding time of 96 days, a period of 33 days and a wavelength of 1480 km.
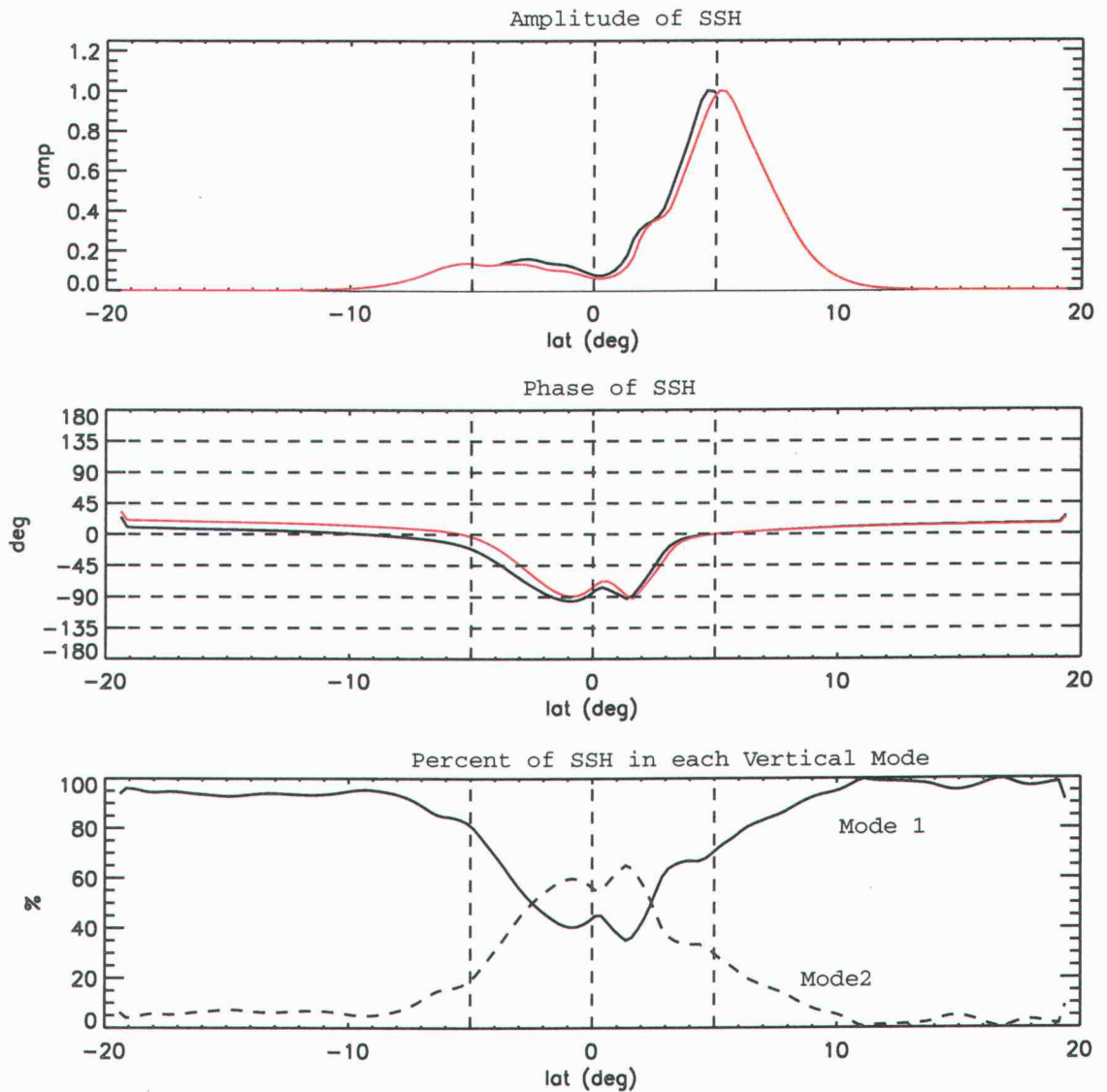
Figure 6.19: The same as Fig. 6.4, except for the latitudinal structure of SSH for the fastest growing solution to the two-mode projection model with the SECN shifted 0.25° to the south. This solution has an e-folding time of 58 days, a period of 30 days and a wavelength of 1336 km.

north and the south ranging from 0° to 65° and e-folding times ranging from 36 to 171 days (Figs. 6.14 and 6.15). These variations in the meridional structure are consistent with the temporal variability of the latitudinal structure of SSH in POCM (section 3.4). Similar changes to all the currents north of the equator produce smaller changes in the e-folding time and the associated variation in the meridional structure of the SSH (Figs. 6.9 and 6.11). In addition, the largest energy transfer occurred on the poleward flank of the SECN (Fig. 5.8).

The stability and meridional structure of the unstable solutions are thus much more sensitive to alterations north of the equator than to alteration south of the equator. Altering only the SECN produces the same types of variations in the solutions as altering all of the currents north of the equator, except with greater sensitivity. This, combined with the source of the energy occurring on both flanks of the SECN, points to the SECN as the most important feature in the Pacific equatorial current system for determining the structure and stability of the solution.

The eigenvalues from all of the altered velocity profiles considered here are summarized in Fig. 6.20. The estimated range of uncertainty of the wavenumber-frequency content of TIWs in POCM is shown by the box. The case in which the SECN was increased by 20% lies near the middle of the box. The scatter of the solutions in wavenumber-frequency space is relatively small, with the cases considered here covering an area only slightly larger than the box that defines the range of uncertainty of the wavenumber-frequency content of TIWs in POCM. However, the stabilities of the solutions vary widely with e-folding times (proportional to the diameters of the circles) ranging from effectively stable solutions (the case where

the SECN was decreased by 20%) to fast growing instabilities (the case where the SECN was increased by 20%).

In a constantly changing mean environment, the solutions to the appropriate eigenvalue problem are also constantly changing. The sensitivity analyses in this chapter have shown that, for reasonable variations in the magnitude and location of the mean currents, significant variation in the meridional structure of the solutions can be expected. This provides for complicated spatial and temporal variations of the structure of SSH over the course of the TIW season.
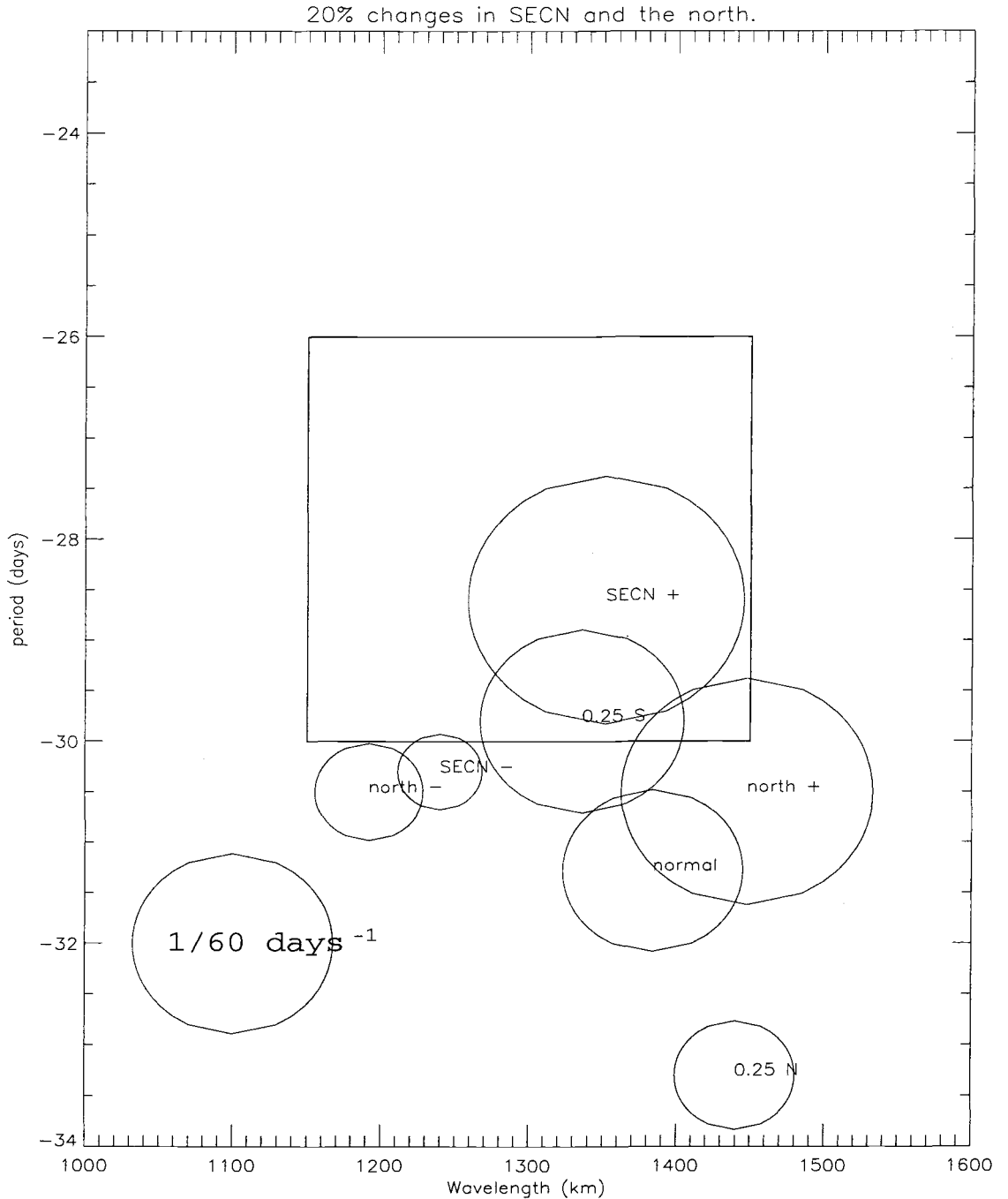
Figure 6.20: Eigenvalues of the solutions from all of the altered current profiles considered here. The box represents the range of uncertainty of the wavenumber-frequency content of TIWs in POCM. The diameters of the circles represent the growth rate of the fastest growing solution. The position of the center of circle represents the wavenumber and period of the fastest growing solution.

7 A CLOSER LOOK AT THE INSTABILITY IN THE TWO-MODE PROJECTION MODEL

It was shown in chapter 5 that the one-mode projection model produced only stable solutions in the wavenumber-frequency regime of the TIW variability in POCM, while the two-mode projection mode produced unstable solutions. In this chapter, a qualitative explanation for this difference is given from consideration of a simplified version of the projection model. Additionally, the latitudinal structure and dispersion characteristics of the solutions in the low-wavenumber limit are examined.

7.1 The Low-Wavenumber Limit

The unstable solutions obtained from the unaltered current profile in the two-mode projection mode were shown to be unstable over a range of wavenumbers (see the top panel Fig. 5.3). The growth rate decreases towards zero as the wavenumber magnitude decreases. The dispersion relation (bottom panel in Fig. 5.3) shows the solution splitting at a wavelength of about 2000 km; at longer wavelengths (smaller wavenumber magnitudes) the solutions are stable.

For the unaltered current profile, the splitting of the dispersion relation occurs at wavelengths far away from those of the TIWs. However, when the westward SECN is reduced (section 6.3), the splitting point in the dispersion relation shifts to higher wavenumber magnitudes as the maximum mean westward velocity is decreases (Fig. 7.1). In this case, the wavenumber splitting occurs close to the wavenumber region of interest for studies of TIWs and the structures of the eigenvectors can be more readily interpreted.
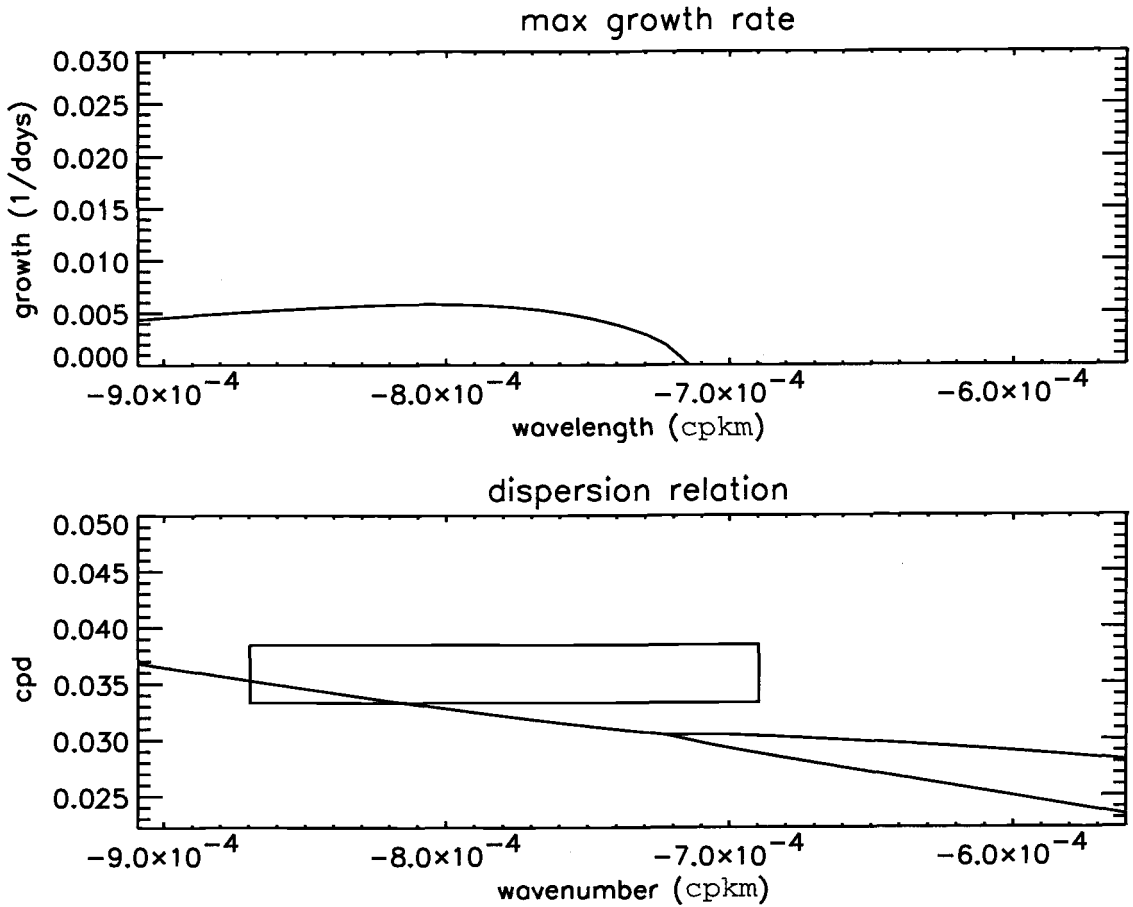
Figure 7.1: The eigenvalues from the stability analysis when the SECN is decreased by 20% (see Fig. 6.15). The upper panel shows the growth rate as a function of wavenumber and the lower panel shows the dispersion relation. The box in the lower panel represents the uncertainty of the wavenumber-frequency range of TIWs in POCM.

The meridional structures of the two free modes, which occur at wavenumbers smaller then -7.2×10^{-4} in Fig. 7.1, resemble the meridional structure of the free mode solutions from the one-mode projection model (Figs. 7.2 and 7.3). The SSH structure for the upper branch of the dispersion curve in Fig. 7.1 is shown in Fig. 7.2. Its amplitude and phase structure are virtually indistinguishable from the altered first meridional mode Rossby wave from the one-mode projection model at the same wavenumber (Fig. 7.2). Although the addition of second vertical mode altered the dispersion relation at higher wavenumber magnitudes, the period of the 1800 km wave remains almost unchanged, as 35.5 days in the one-mode model and 35.6 days in the two-mode projection model. Additionally, the two-mode solution is almost wholly vertical mode one (bottom panel of Fig. ??). Because of these characteristics, the solutions along the upper branch of the dispersion relation for the two-mode projection model can be interpreted as a vertical mode 1, meridional mode 1 Rossby wave (M1 Rossby wave).

The SSH structure of the solutions along the lower branch of the dispersion curve to the right of the split cannot be explained quite as simply as the solutions along the upper branch. The 1800 km wave solution from the upper branch of the dispersion relation (Fig. 7.3) is nearly identical in phase and amplitude to the second meridional mode from the one-mode projection model (Fig. 7.3), with only slight differences in amplitude near 5°S. The 43.2 day period of the 1800 km two-mode solution is nearly identical to the 43.8 day period of the one-mode projection model. The solution of the two-mode projection model thus appears to be the vertical mode 1, meridional mode 2 Rossby wave (M2 Rossby wave). However, the bottom panel in Fig. 7.3 shows that there is an interaction with the

Amplitude

Phase

Fraction of the SSH amplitude in each mode
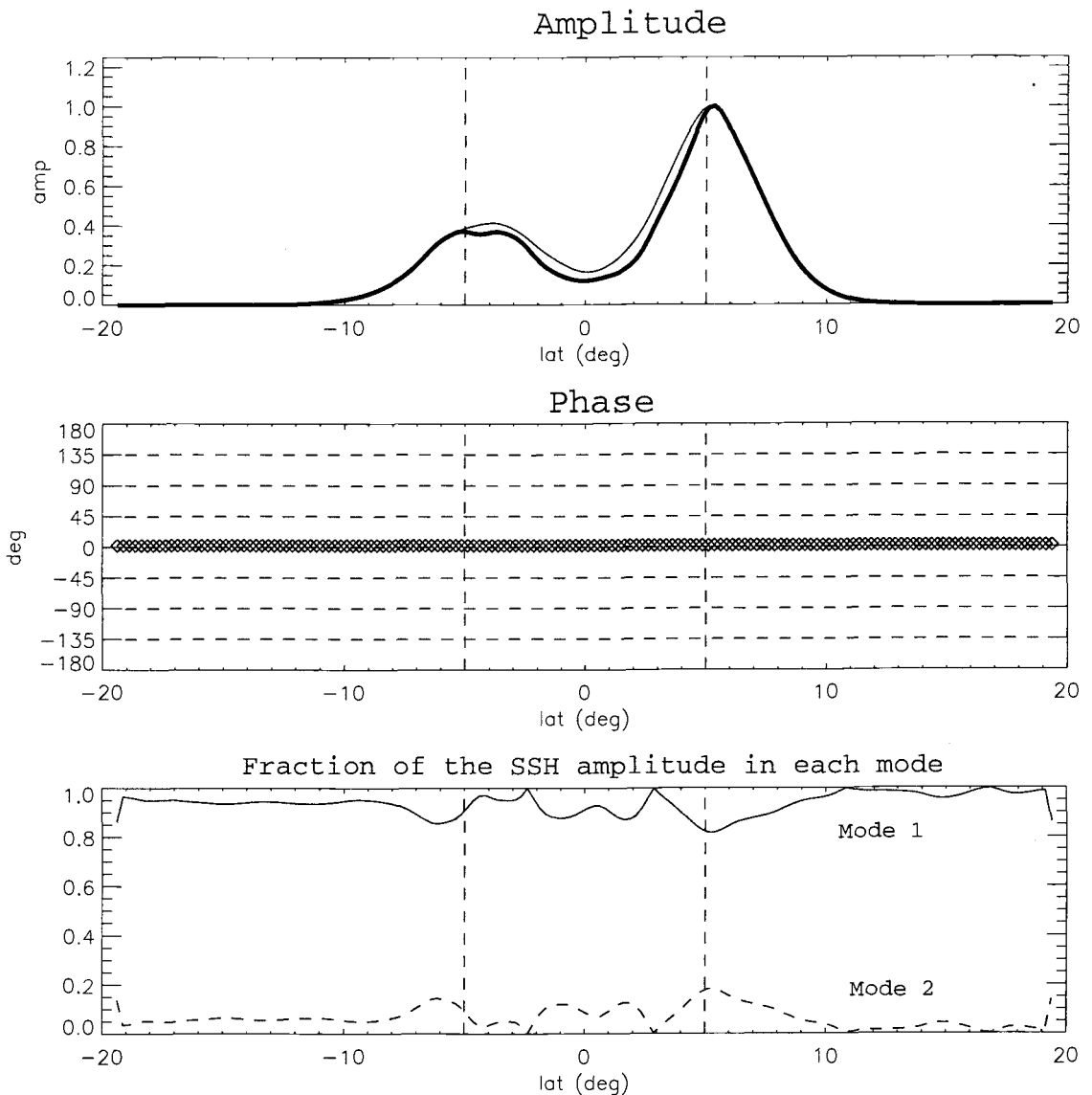
Figure 7.2: The latitudinal structures of the amplitude (top) and phase (middle) of SSH for the 1800 km, 35.5 day wave from the one-mode stability analysis (thin black line in top panel) and the 1800 km, 35.6 day wave from the two-mode stability analysis (thick black line in top panel). In both cases, the SECN was decreased by 20%. The phase of the one- and two-mode solutions are the same. The one-mode solution corresponds to the structure of the altered first meridional Rossby wave. The two-mode solutions corresponds to the upper branch of the stable portion of the dispersion curve to the right of the split in Fig. 7.1. The bottom panel shows the relative contribution of the first and second vertical modes of variability from the two-mode projection model.

second vertical mode near the equator. This solution cannot therefore be solely described as a M2 Rossby wave, and hence will be referred to he! re as an altered M2 Rossby wave.

At the wavenumbers to the right of the splitting point the M2 Rossby wave speeds up and begins to interact with the M1 Rossby wave (Fig. 7.1). At the point where the two solutions coalesce, the M1 Rossby wave resonates with the altered M2 Rossby wave and an instability is formed. For the wavenumber range over which there is a single dispersion curve, there are two distinct eigenvalues that are complex conjugates of each other. These solutions have the same period and wavenumber but one has a positive growth rate and the other has a negative growth rate.

7.2   Why does the Two-Mode Projection Model produce TIWs and the One-Mode Projection Mode does not?

Although the one-mode projection model is stable in the region of dispersion space where TIWs reside, it does yield instabilities in other regions of wavenumber-frequency space (Fig. 7.4). Hence, the mean fields in both the one-mode and two-mode projection models produce unstable solutions and any necessary conditions for instability, such as a change in the sign in the gradient of potential vorticity, are met in both cases.

Compared to the two-mode projection model, the mean currents in the one-mode projection have little effect on the phase speed of the altered M2 Rossby. The slower M2 Rossby wave doesn't interact with the M1 Rossby wave in the TIW wavenumber-frequency range. This can be seen in Fig. 7.4. where the first doted line bellow the rectangle is the M1 Rossby wave and the second dotted

Amplitude

Phase

Fraction of the SSH amplitude in each mode
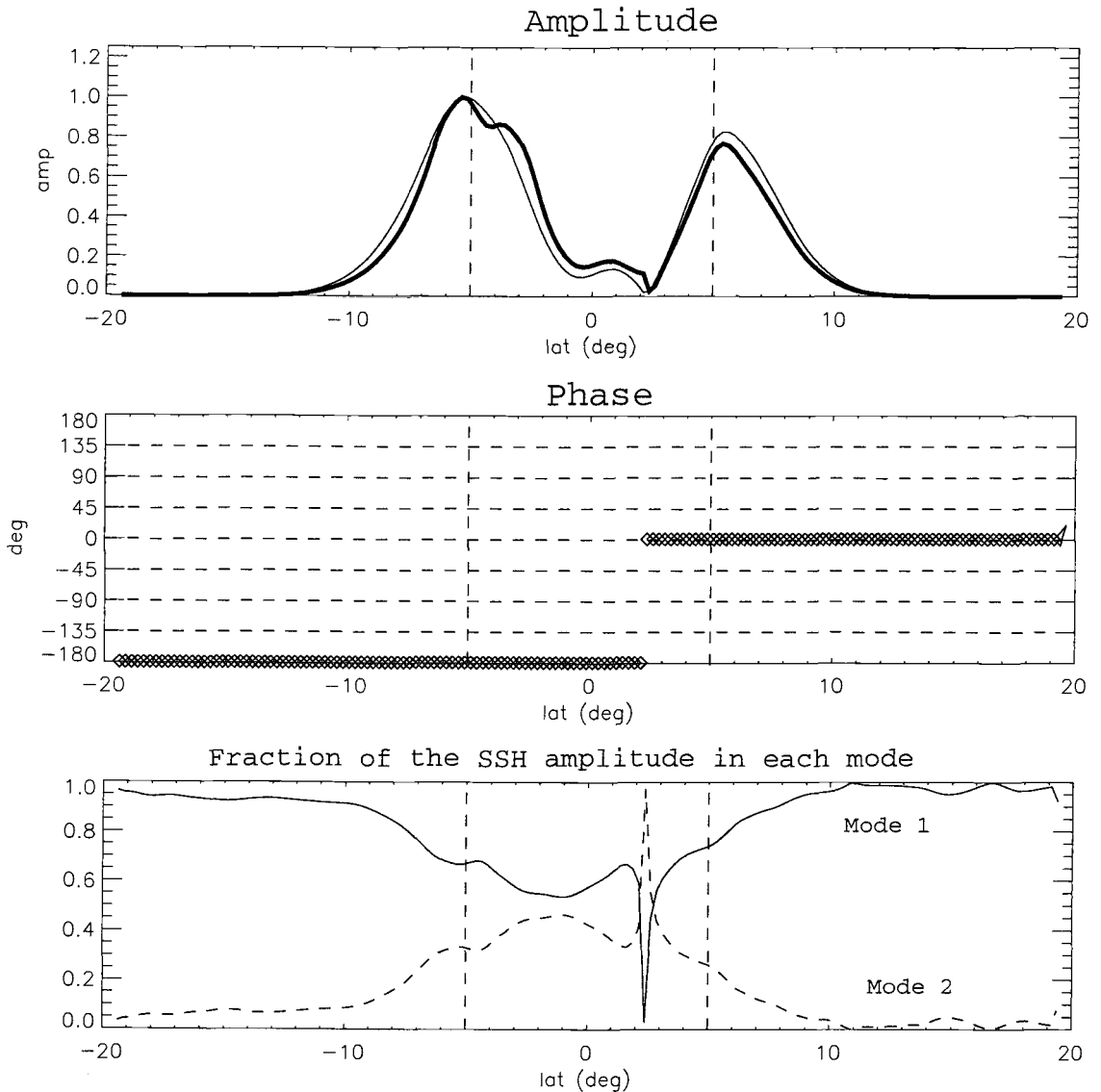
Figure 7.3: The same as Fig. 7.2, except for the 1800 km, 43.8 day wave from the one-mode stability analysis and the 1800 km, 43.2 day wave from the two-mode projection model. The one-mode solution corresponds to the structure of the altered second meridional mode Rossby wave. The two-mode solution corresponds to the structure of the second meridional mode Rossby wave along the lower branch of the dispersion curve to right of the splitting point in Fig. 7.1.

Dispersion Realation for the one-mode projection model

= 1/365 days^{-1}
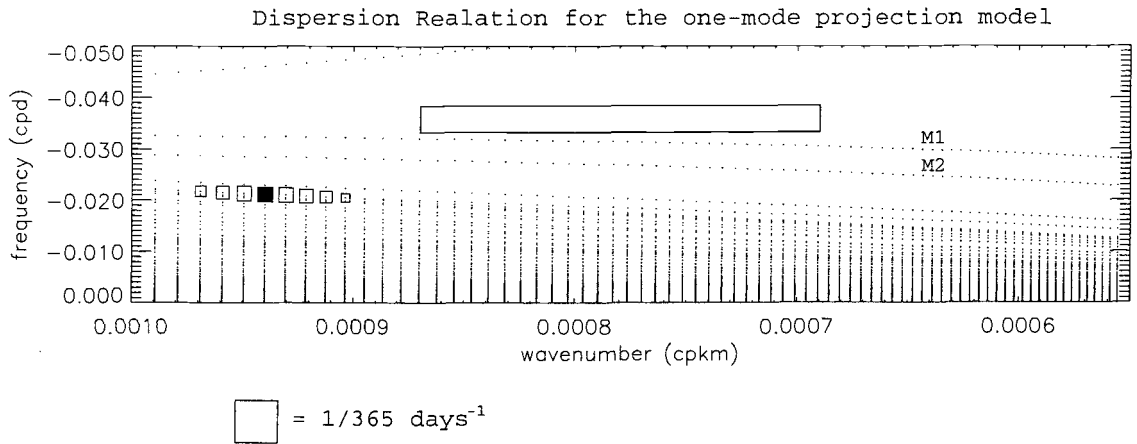
Figure 7.4: The dispersion relation for the unaltered current profile in the one-mode projection model. The rectangle represents an estimate of TIWs in POCM. The dots represent the eigenvalues, with the location corresponding to the frequency and wavenumber. Unstable solutions are plotted as small squares with size corresponding to the growth rate. The square corresponding to the fastest growing unstable wave is filled. Eigenvalues with growth rates less than 1/2000 $days^{-1}$ are plotted as dots.

line bellow the rectangle is the alter M2 Rossby wave. In the one-mode projection model projection model these lines run parallel and the M1 and altered M2 Rossby waves are unable to resonate to form the instability as in the case of the two-mode projection model (see Fig.7.1).

8 SUMMARY AND CONCLUSIONS

TIWs are a dominant feature of monthly SST and SSH variability in the equatorial Pacific and Atlantic oceans. They appear in T/P SSH data as two bands of variability centered on 5°N and 5°S with an approximate period of 34 ± 2 days and a wavelength of 1600 ± 150 km which have both annual and interannual modulations. It has been established that TIWs are generated from instabilities in the meridionally and vertically sheared equatorial current systems. However, direct observations of the equatorial currents have inadequate spatial and temporal resolutions for use in a linear stability analysis of TIWs. This study has therefore investigated the effects of mean currents from the POCM model. The TIW signatures in POCM SSH are similar to those found in T/P; there are two bands of variability centered on 5°N and 5°S, they have an approximate period of 28 ± 2 days and a wavelength of 1300 ± 150 km with both annual and interannual modulations. Although there are quantitative differences between the TIWs in POCM and T/P, they are similar enough that POCM can provide insight into the dynamics of TIWs in the real world.

The cross-equatorial phase and amplitude of the SSH signatures of TIWs in POCM during the period of July 8 to September 6 1995 are reproduced in a linearized model that projects the vertical structure onto the first and second baroclinic modes. Amplitudes north of the equator are 3 to 5 times larger than south of the equator, while the phase lag between 5°N and 5°S ranges between 0° and 45°. These structures, which are similar to those seen in T/P data, have not been reproduced by previous linearized stability analysis.

Perhaps surprisingly, two vertical modes are sufficient to describe the initial stages of TIWs. It was shown in section 5.4 that the addition of higher modes (shown for the five-mode projection model) lead to TIWs with cross-equatorial structure, wavenumber-frequency content and vertical structure very similar to the TIWs produced by the two-mode projection model. The one-mode projection model however, does not produce an unstable solution in the wavenumber-frequency regime of observed TIWs. As shown in section 7.1, this is because the mean currents fail to speed up the M2 Rossby wave when the frist vertical mode is only considered in the projection of the state variables.

Unexpectedly, changes in the SECN in the two-mode projection model were found to have the largest effect on the amplitude of the TIW SSH signal south of the equator. Decreasing the SECN by 20% increases the amplitude south of the equator, which increases the equatorial symmetry. Likewise, increasing the SECN by 20% decreases the equatorial symmetry. These effects are attributed to the SECN because alterations of the mean currents south of the equator do not have a noticeable effect on the latitudinal structure of the TIWs. Reconfirming previous analyses, the SECN is also shown to have the largest effect on the growth rate of TIWs in the two-mode projection model (chapter 6). Increasing the SECN causes the growth rate of the TIWs to increase, while decreasing the SECN has the opposite effect.

Several previous linear stability analyses of TIWs used layer models. Given a mean current, these linearized layer models have either low vertical resolution and an arbitrary vertical averaging scheme [*Philander*, 1978; *McCreary and Yu*, 1992] or very complicated vertical structure [*Proehl*, 1998]. The projection model

avoids these problems. By weighting the vertical average of the mean fields by the vertical eigenfunctions the projection model avoids the need for an arbitrary vertical averaging scheme. The projection model is also relatively simple, requiring only two vertical modes to describe TIWs. An advantage of the simple vertical structure in the two-mode projection model is the easy identification of the two stable solutions (the first and second meridional mode Rossby waves) that form the TIWs in the low-wavenumber limit.

When fully developed, TIWs are non-linear [*Kennan and Flament*, 2000]. As in the case of all linearized models, the assumptions of the projection model are then invalid. The projection model therefore cannot describe the structure of the TIWs across the entire Pacific or during all times. It was shown in Chapter 5, however, that TIWs develop during the beginning of the 1995-1996 TIW season as an asymmetric and almost completely barotropic instability. Another shared deficiency of linearized stability analyses is the need for a prescribed mean current profile. In practice, the mean current is not known or even well defined since the background currents evolve considerably over the curse of a TIW season. The mean change temporally and spatially due to external forcing and are altered by the TIWs. The sensitivity of TIWs to moderate changes in the background currents makes it difficult to identify a dominant cross-equatorial structure in the SSH signatures of TIWs (see chapter 6).

The projection model was only applied here to study TIWs in the Pacific from POCM. Other regions, such as the equatorial Atlantic, have yet to be explored. Ultimately, the mean current profiles used in the projection model will be obtained from in situ data, rather than from POCM. The eigenfunctions can then be com-

pared to T/P SSH data. The projection model can also be applied to investigate the effects of mean currents on stable low-frequency Rossby waves.

BIBLIOGRAPHY

Allen, M. R., S. P. Lawrence, M. J. Murray, C. T. Mutlow, T. N. Stockdale, D. T. Llewellyn-Jones, and D. L. T. Anderson, Control of tropical instability waves in the Pacific, *J. Phys. Oceanogr.*, *22*, 2581–2584, 1995.

Barnett, T. P., and W. C. Patzert, Scales of thermal variability in the tropical Pacific, *J. Phys. Oceanogr.*, *10*, 529–540, 1980.

Baturin, N. G., and P. P. Niiler, Effects of instability waves in the mixed layer of the equatorial Pacific, *J. Geophys. Res.*, *102*, 21,771–21,793, 1997.

Bryden, H. L., and E. C. Brady, Eddy momentum and heat fluxes and their effects on the circulation of the equatorial Pacific ocean, *J. Mar. Res.*, *47*, 55–79, 1989.

Carton, J. A., B. S. Giese, X. Cao, and L. Miller, Impact of altimeter, thermistor, and expendable bathythermograph data on retrospective analysis of the tropical Pacific ocean, *J. Geophys. Res.*, *101*, 14,147–14,159, 1996.

Chang, P., and S. G. H. Philander, Rossby wave packets in baroclinic mean currents, *Deep-Sea Res.*, *36*, 17–37, 1989.

Chelton, D. B., F. J. Wentz, C. L. Gentemann, R. A. deSzoeke, and M. G. Schlax, Satellite microwave sst observation of transequatorail Tropical Instability Waves, *Geophys. Res. Lett.*, *27*, 1239–1242, 2000.

Chelton, D. B., M. G. Schlax, S. K. Esbensen, N. Thum, M. H. Freilich, F. J. Wents, C. L. Gentemann, and M. J. McPhaden, Observations of coupling between surface wind stress and sea surface temperature in the eastern tropical Pacific, *J. of Climate*, *14*, 1479–1498, 2001.

Chelton, D. B., M. G. Schlax, J. M. Lyman, and R. A. deSzoeke, The latitudinal structure of monthly variability in the tropical Pacific, *J. Phys. Oceanogr.*, *in prep*, 2003.

Contreras, R. F., Long-term observation of Tropical Instability Waves, *unknown*, *in prep*, 2001.

Cox, M. D., Generation and propagation of 30-day waves in a numerical model of the Pacific, *J. Phys. Oceanogr.*, *10*, 1168–1186, 1980.

Donohue, K. A., and M. Wimbush, Model results of flow instabilities in the tropical Pacific Ocean, *J. Geophys. Res.*, *103*, 21,401–21,412, 1998.

Eriksen, C. C., Moored observation of deep low-frequency motions in the central Pacific ocean: Vertical structure and interpretation as equatorial waves, *J. Phys. Oceanogr.*, *15*, 1,085–1,113, 1985.

Eriksen, C. C., and J. G. Richman, An estimate of equatorial wave energy flux at 9- to 90- day periods in the central Pacific, *J. Geophys. Res.*, *93*, 15,455–15,466, 1988.

Flament, P. J., S. C. Kennan, R. A. Knox, P. P. Niiler, and R. L. Bernstein, The three-dimensional structure of an upper ocean vortex in the tropical Pacific Ocean, *Nature*, *383*, 610–613, 1996.

Foley, D. G., et al., Longwaves and primary productivity variations in the equatorial Pacific at 0°,140°W, *Deep-Sea Res. II*, *44*, 1,801–1,826, 1997.

Giese, B. S., J. A. Carton, and L. J. Holl, Sea level variability in the eastern tropical Pacific as observed by TOPEX and Tropical Ocean-Global Atmosphere Tropical Atmosphere-Ocean Experiment, *J. Geophys. Res.*, *99*, 24,739–24,748, 1994.

Gill, A. E., *Atmosphere-Ocean Dynamics*, Academic Press, 1982.

Halpern, D., and R. H. Weisberg, Upper ocean thermal and flow fields at 0°,28°W (Atlantic) and 0°,140°W (Pacific) durring 1983-1985, *Deep-Sea Res.*, *36*, 407–418, 1989.

Halpern, D., R. A. Knox, and D. S. Luther, Observations of 20-day meridional current oscillations in the upper ocean along the Pacific equator, *J. Phys. Oceanogr.*, *18*, 1514–1534, 1988.

Hansen, D. V., and C. A. Paul, Genesis and effects of long waves in the equatorila Pacific, *J. Geophys. Res.*, *89*, 10,431–10,440, 1984.

Harvey, R. R., and W. C. Patzert, Deep current measurements suggest long waves in the eastern equatorial Pacific, *Science*, *193*, 883–885, 1976.

Hashizume, H., S.-P. Xie, W. T. Liu, and K. Takeuchi, Local and remote atmospheric response to tropical instability waves: A global view from space, *J. Geophys. Res.*, *106*, 10,173–10,185, 2001.

Hayes, S. P., M. J. McPhaden, and J. M. Wallace, The influence of sea-surface temperature on surface wind in the east equatorial Pacific: weekly to monthly variability, *J. Clim*, *2*, 1500–1506, 1989.

Johnson, E. S., and D. S. Luther, Mean zonal momentum balance in the upper and central equatorial Pacific Ocean, *J. Geophys. Res.*, *99*, 7689–7705, 1994.

Johnson, G. C., B. M. Sloyan, W. S. Kessler, and K. E. McTaggart, Direct measurements of upper ocean currents and water properties across the Tropical Pacific Ocean during the 1990s, *Prog. Oceanogr.*, *in prep*, 2002.

Kennan, S. C., and P. J. Flament, Observations of a tropical instability vortex, *J. Phys. Oceanogr.*, *30*, 2277–2301, 2000.

Kessler, W. S., personal communications, 2001.

Lawrence, S. P., and J. P. Angell, Evidence for Rossby wave control of Tropical Instability Waves in the Pacific ocean, *Geophys. Res. Lett.*, *27*, 2,257–2,260, 2000.

Lawrence, S. P., M. R. Allen, D. L. T. Anderson, and D. T. Llewellyn-Jones, Effects of subsurface ocean dynamics on instability waves in the tropical Pacific, *J. Geophys. Res.*, *103*, 18,649–18,663, 1998.

Legeckis, R., Long waves in the eastern equatorial Pacific Ocean: A view from a geostationary satellite, *Science*, *197*, 1179–1181, 1977.

Legeckis, R., Long waves in the equatorial Pacific and Atlantic oceans durring 1983, *Ocean-Air Interactions*, *1*, 1–10, 1986.

Legeckis, R., E. Pichel, and G. Nesterczuk, Equatorial long waves in geostationary satellite observation and in a multichannel sea surface temperature analysis, *Bull. Am. Meteorol. Soc.*, *64*, 133–139, 1983.

Liu, W. T., X. Xie, P. S. Polito, S.-P. Xie, and H. Hashizume, Atmospheric manifestation of tropical instability wave observed by QuikSCAT and Tropical Rain Measuring Mission, *Geophys. Res. Lett.*, *27*, 2,545–2,548, 2000.

Lukas, R., Horizontal Reynolds Stresses in the central equatorial Pacific, *J. Geophys. Res.*, *92*, 9453–9463, 1987.

Luther, D. S., and E. S. Johnson, Eddy energetics in the upper equatorial Pacific during Hawaii-to-Tahiti Shuttle Experiment, *J. Phys. Oceanogr.*, *20*, 913–944, 1990.

Malardé, J. P., P. D. Mey, C. Périgaud, and J. F. Minster, Observations of long equatorial waves in the Pacific ocean by Seasat altimetry, *J. Phys. Oceanogr.*, *17*, 2273–2279, 1987.

Mallat, S., *a Wavelet tour of signal processing*, Academic Press, 1999.

Masina, S., G. Philander, and A. Bush, An analysis of tropical instability waves in a numerical model of the Pacific ocean. Part I: Spatial variability, *J. Geophys. Res.*, *104*, 29,613–29,636, 1999a.

Masina, S., G. Philander, and A. Bush, An analysis of tropical instability waves in a numerical model of the Pacific ocean. Part II: Generation and energetics, *J. Geophys. Res.*, *104*, 29,637–29,662, 1999b.

McClean, J. L., A. J. Semtner, and V. Zlotnicki, Comparisons of mesoscale variability in the semtner-chervin 1/4° model, the Los Alamos Parallel Ocean Program 1/6° model, and TOPEX/POSEIDON data, *J. Geophys. Res.*, *102*, 25,203–25,226, 1997.

McCreary, J. P., and Z. Yu, Equatorial dynamics in a 2.5-layer model, *Prog. Oceanogr.*, *29*, 61–132, 1992.

McPhaden, M. J., Monthly period oscillations in the Pacific North Equatorial Countercurrent, *J. Geophys. Res.*, *16*, 6337–6359, 1996.

Menkes, C., J.-P. Boulanger, and A. J. Busalacchi, Evaluation of TOPEX and basin-wide Tropical Ocean and Global Atmosphere-Tropical Atmosphere Ocean sea surface topographies and derived geostropic currents, *J. Geophys. Res.*, *101*, 25,087–25,099, 1996.

Miller, L., D. R. Watts, and M. Wimbush, Oscillations of dynamic topography in the eastern equatorial Pacific, *J. Phys. Oceanogr.*, *15*, 1759–1770, 1985.

Mitchum, G. T., and R. Lukas, The latitude-frequency structure of the Pacific sea level variance, *J. Phys. Oceanogr.*, *17*, 2362–2365, 1987.

Musman, S., Sea height wave form in equatorial waves and its interpretation, *J. Geophys. Res.*, *94*, 3303–3309, 1989.

Pedlosky, J., *Geophysical Fluid Dynamics*, Springer, 1987.

Périgaud, C., Sea level oscillations observed with Geosat along the two shear fronts of the Pacific North Equatorial Countercurrent, *J. Geophys. Res.*, *95*, 7239–7248, 1990.

Philander, S. G. H., Instabilities of zonal equatorial currents, *J. Geophys. Res.*, *81*, 3725–3735, 1976.

Philander, S. G. H., Instabilities of zonal equatorial currents, 2, *J. Geophys. Res.*, *83*, 3679–3682, 1978.

Philander, S. G. H., D. Halpern, D. Hansen, R. Legeckis, L. miller, C. Paul, R. Watts, R. Weisberg, and M. Wimbush, Long waves in the equatorial Pacific Ocean, *EOS Trans. AGU*, *66*, 154, 1985.

Philander, S. G. H., W. J. Hurlin, and R. C. Pacanowski, Properties of long equatorial waves in models of the seasonal cycle in the tropical Atlantic and Pacific oceans, *J. Geophys. Res.*, *91*, 14,207–14,211, 1986.

Proehl, J. A., Equatorial wave-mean flow interactions: The long Rossby waves, *J. Phys. Oceanogr.*, *20*, 274–294, 1990.

Proehl, J. A., On the numerical dispersion relation of equatorial waves, *J. Geophys. Res.*, *96*, 16,929–16,934, 1991.

Proehl, J. A., The role of meridional flow asymmetry in the dynamics of tropical instability, *J. Geophys. Res.*, *103*, 24,597–24,618, 1998.

Pullen, P. E., R. L. Bernstein, and D. Halpern, Equatorial long-wave characteristics determined from satellite Sea Surface Temperature and in situ data, *J. Geophys. Res.*, *92*, 742–748, 1987.

Qiao, L., and R. H. Weisberg, Tropical instability wave kinematics: Observations from the Tropical Instability Wave Experiment, *J. Geophys. Res.*, *100*, 8677–8693, 1995.

Qiao, L., and R. H. Weisberg, Tropical instability wave energetics: Observations from the Tropical Instability Wave Experiment, *J. Phys. Oceanogr.*, *28*, 345–360, 1998.

Reynolds, R. W., and T. M. Smith, Improved global sea surface temperature analysis using optimum interpolation, *J. Phys. Oceanogr.*, *24*, 929–948, 1994.

Schopf, P. S., and M. A. Cane, On equatorial dynamics, mixed layer physics and sea surface temperature, *J. Phys. Oceanogr.*, *13*, 917–935, 1983.

Seidel, H. F., and B. S. Giese, Equatorial currents in the Pacific ocean 1992-1997, *J. Geophys. Res.*, *104*, 7849–7863, 1999.

Seigel, A. D., A comment on long waves in the Pacific ocean, *J. Phys. Oceanogr.*, *10*, 1881–1883, 1985.

Semtner, A. J. J., and R. M. Chervin, Ocean general circulation from a global eddy-resolving model, *J. Geophys. Res.*, *97*, 5493–5550, 1992.

Semtner, A. J. J., and W. Holland, Numerical simulation of equatorial ocean circulation. part i: A basic case in turbulent equilibrium, *J. Phys. Oceanogr.*, *10*, 667–693, 1980.

Stammer, D., Steric and wind-induced changes in TOPEX/POSEIDON large-scale sea surface topography observations, *J. Geophys. Res.*, *102*, 20,987–21,009, 1997.

Strutton, P. G., J. P. Ryan, and F. P. Chavez, Enhanced chlorophyll associated with tropical instability waves in the equatorial Pacific, *Geophys. Res. Lett.*, *28*, 2005–2008, 2001.

Swenson, M. S., and D. V. Hansen, Tropical Pacific ocean mixed layer heat budget: the Pacific Cold Tongue, *J. Phys. Oceanogr.*, *29*, 69–81, 1999.

Vialard, J., C. Menkes, and D. L. T. Anderson, Phase locking of Pacific ocean tropical instability waves, *J. Geophys. Res., in press*, 2001.

Weidman, P. D., D. L. Mickler, B. Dayyani, and G. H. Born, Analysis of legeckis eddies in the near-equatiorial Pacific, *J. Geophys. Res.*, *104*, 7865–7887, 1999.

Weisberg, R. H., and S. P. Hayes, Upper ocean variability on the equator in the Pacific at 170°W, *J. Geophys. Res.*, *100*, 20,485–20,498, 1995.

Wilson, D., and A. Leetmaa, Acoustic doppler current profiling in the equatorial Pacific in 1984, *J. Geophys. Res.*, *93*, 13,947–13,966, 1988.

Wyrtki, K., Sea level variations: Monitoring the breath of the Pacific, *EOS Trans. AGU*, *60*, 25–27, 1979.

Wyrtki, K., E. Firing, D. Halpern, R. Knox, G. J. McNally, W. C. Patzert, E. D. Stroup, B. A. Taft, and R. Williams, The Hawwaii to Tahiti shuttle experiment, *Science*, *211*, 22–28, 1981.

Xie, S.-P., M. Ishiwatari, H. Hashizume, and K. Takeuchi, Coupled ocean-atmospheric waves on the equatorial front, *Geophys. Res. Lett.*, *25*, 3863–3866, 1998.

Yu, Z., J. P. McCreary, and J. A. Proehl, On the meridional asymmetry and energetics of tropical instability waves, *J. Phys. Oceanogr.*, *25*, 1680–1686, 1995.

Zheng, Q., X. H. Yan, C. R. Ho, and C. K. Tai, The effects of shear flow on propagation of Rossby waves in the equatorial oceans, *J. Phys. Oceanogr.*, *24*, 1680–1686, 1994.

APPENDICES

A VERTICAL EIGENFUNCTIONS

A set of vertical eigenfunctions can easily be obtained that span the space of the mean fields and state variables, are orthogonal, and are physically representative of the vertical structure of the ocean. These eigenfunctions are the solutions to the general equations of motion, (4.10)-(4.12), with $U_o(y, z) = 0$. Physically, they define the vertical structure of the baroclinic modes in the absence of a mean flow.

The equation that defines the vertical eigenvalue problem can be obtained when equations (4.1)-(4.5) are written in terms of p with $U_o = 0$ and $\rho_o = \rho_o(z)$. If it is then assumed that $p = \psi(z)p(x, y, t)$, an equation for the vertical dependence of $\psi(z)$ can be separated, resulting in

$$\frac{\partial}{\partial z}\left(\frac{1}{N^2}\frac{\partial \psi_n}{\partial z}\right) = \frac{-1}{c_n^2}\psi_n \tag{A.1}$$

where,

$$-\frac{1}{c_n} = \text{the eigenvalue for mode } n$$

$$\psi_n = \text{the eigenfunction for mode } n$$

The associated equation for $p(x, y, t)$ reveals that c_n is the baroclinic phase speed for mode n [*Pedlosky*, 1987]. The eigenfunctions ψ_n are defined by a representative mean density profile $\rho_o(z)$ which is consistent with the density decomposition eq. (4.9). In order to solve eq. (A.1), boundary conditions eq. (4.7)

must be satisfied. Applying (4.5), (4.3) and the assumption that $\rho_o(y,z)$ is a weakly varying function of y, boundary condition (4.7) can be rewritten as,

$$\frac{\partial \psi_n}{\partial z} = 0 \text{ at } z = 0 \text{ } and \text{ } z = -H, \tag{A.2}$$

where H is the depth of the water column.

The solutions ψ_n of the Sturm-Liouville eigenvalue problem eqs. (A.1) and (A.2) are orthogonal and span the space subject to their boundary conditions. Examples of the structure of the first two modes are shown in Figs. A.1 and A.2.
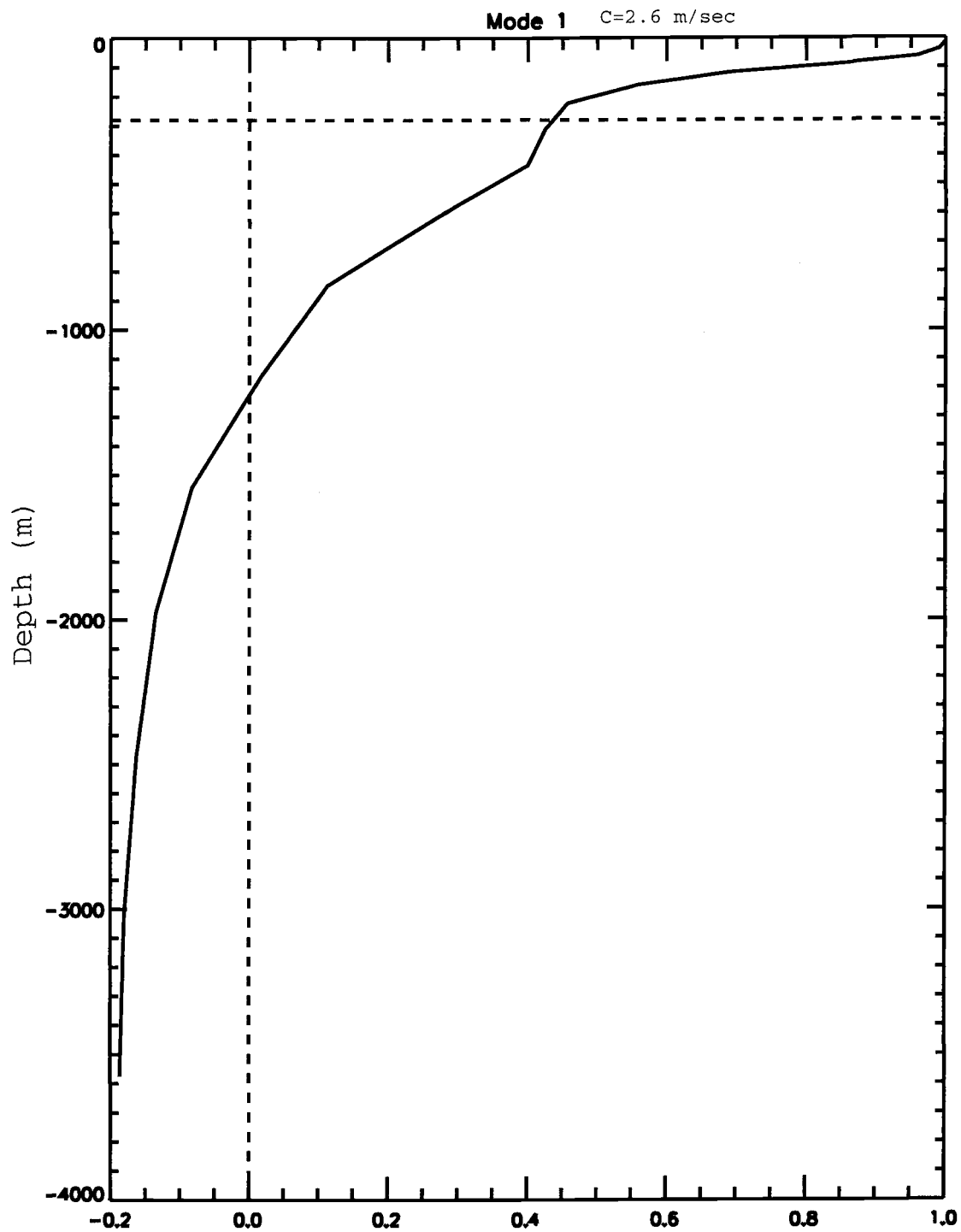
Figure A.1: The first baroclinic vertical eigenfunction used in the projection model. The phase speed of this mode is 2.6 m/sec.
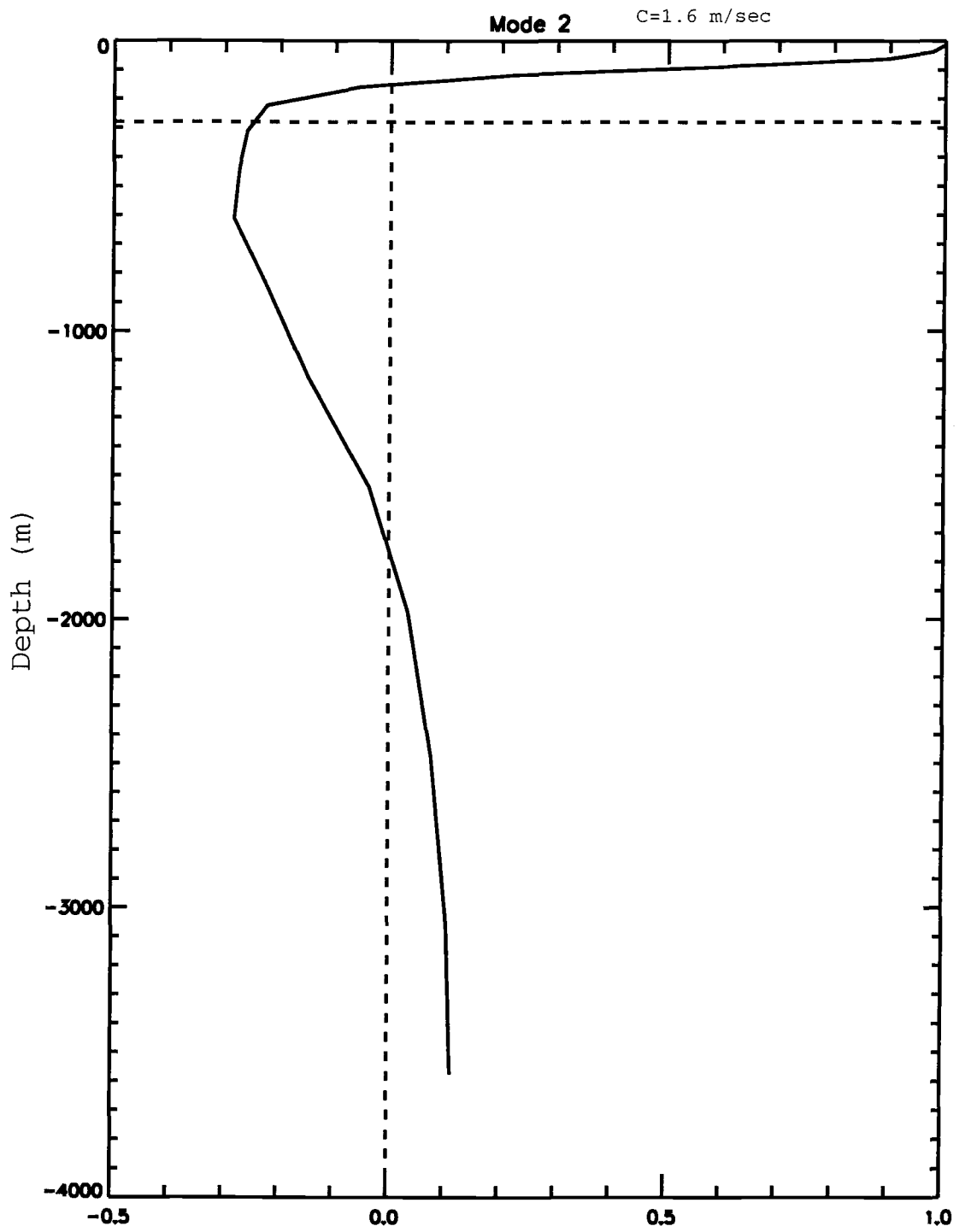
Figure A.2: The second baroclinic vertical eigenfunction used in the projection model. The phase speed of this mode is 1.6 m/sec.

B THE 2-LAYER REDUCED GRAVITY MODEL

A 2-layer, reduced-gravity model is one of the simplest representations of equatorial dynamics [*Gill*, 1982]. The model can be expressed by the three equations,

$$\left(\frac{\partial}{\partial t} + U_o(y)\frac{\partial}{\partial x}\right)u + \left(\frac{\partial U_o}{\partial y} - \beta y\right)v + g'\frac{\partial}{\partial x}\eta = 0 \qquad (B.1)$$

$$\left(\frac{\partial}{\partial t} + U_o(y)\frac{\partial}{\partial x}\right)v + \beta y u + g'\frac{\partial}{\partial y}\eta = 0 \qquad (B.2)$$

$$\left(\frac{\partial}{\partial t} + U_o(y)\frac{\partial}{\partial x}\right)\eta + \left(\frac{\partial H}{\partial y} + H(y)\frac{\partial}{\partial y}\right)v + H(y)\frac{\partial}{\partial x}u = 0 \qquad (B.3)$$

where,

$$\eta = \text{the perturbation sea surface height}$$

$$g' = \text{the reduced gravity}$$

$$U_o(y) = \text{the mean flow in the upper layer}$$

$$H(y) = \text{the upper layer thickness}$$

The equations (B.1)-(B.3) have been linearized about $U_o(y)$ which is in geostrophic equilibrium with mean layer thickness $H(y)$ and are subject to a rigid lid approximation and the Boussinesq approximation. These equations are further subject to the boundary conditions:

$$v = 0, \text{ at the northern and southern boundaries} \qquad (B.4)$$

If the state variables, u, v and η are assumed to be a traveling wave solutions of the form $e^{i(kx-\omega t)}$, then equations (B.1)-(B.3) can be rewritten in matrix form as:

$$
\begin{bmatrix}
U_o(y)k & i\left(\beta y - \frac{\partial U_o}{\partial y}\right) & \frac{1}{\rho_*}k \\
-i\beta y & U_o(y)k & -\frac{i}{\rho_*}\frac{\partial}{\partial y} \\
g'\rho_\times H(y)k & -ig'\rho_\times\left(\frac{\partial H}{\partial y} + H(y)\frac{\partial}{\partial y}\right) & U(y)_o k
\end{bmatrix}
\begin{bmatrix}
u \\
v \\
p
\end{bmatrix}
= \omega
\begin{bmatrix}
u \\
v \\
p
\end{bmatrix}
\tag{B.5}
$$

The quantities $U_o(y), g'$ and $H(y)$ must be specified in the matrix equation (B.5). Even if sufficient information is available about the vertical and horizontal structure of the velocity and density fields, the definition of $U_o(y), g'$ and $H(y)$ are inevitably subject to arbitrary vertical averaging.

C HIGHER ORDER PROJECTION MODEL

Matrix equation (4.28) can be expanded to contain higher order vertical modes. The method is similar to that for one mode described in section 4.2.

The set of equations for mode j are obtained by expanding the state variables in equations (4.10)-(4.12) in terms of ψ_i, according to (4.14)-(4.16). The results are multiplied by ψ_j and vertically integrated. Modes higher then j are truncated. The mean fields in turn become:

$$\overline{U_{ij}^{(1)}}(y) \quad \equiv \quad \int_{-H}^{0} U_o \psi_i \psi_j \, dz \tag{C.1}$$

$$\overline{U_{yij}^{(1)}}(y) \quad \equiv \quad \int_{-H}^{0} \frac{\partial U_o}{\partial y} \psi_i \psi_j \, dz \tag{C.2}$$

$$\overline{U_{ij}^{(2)}}(y) \quad \equiv \quad \int_{-H}^{0} \frac{-c_j^2}{N^2} \frac{\partial U_o}{\partial z} \psi_i' \psi_j \, dz \tag{C.3}$$

$$\overline{f_{ij}^{\sim}}(y) \quad \equiv \quad \int_{-H}^{0} \frac{g}{\rho_\star N^2} \frac{\partial U_o}{\partial z} \frac{\partial \rho_o}{\partial y} \psi_i \psi_j \, dz \tag{C.4}$$

$$\overline{H_{yij}^{(1)}}(y) \quad \equiv \quad c_j^2 \int_{-H}^{0} \frac{1}{\rho_\star} \frac{\partial}{\partial z} \left(\frac{1}{N^2} \frac{\partial \rho_o}{\partial y} \right) \psi_i \psi_j \, dz \tag{C.5}$$

$$\overline{H_{yij}^{(2)}}(y) \quad \equiv \quad c_j^2 \int_{-H}^{0} \frac{1}{\rho_\star} \left(\frac{1}{N^2} \frac{\partial \rho_o}{\partial y} \right) \psi_i' \psi_j \, dz \tag{C.6}$$

After applying the assumptions (4.25), (4.26) and (4.27), the equations of motion can be rewritten in terms of these mean fields for an arbitrary number of vertical modes. The matrix representing the equations for the first two vertical modes is:

$$
\begin{bmatrix}
A_{11} & A_{12} & A_{13} & A_{14} & A_{15} & 0 \\
A_{21} & A_{22} & A_{23} & 0 & A_{25} & 0 \\
A_{31} & A_{32} & A_{33} & 0 & A_{35} & A_{36} \\
A_{41} & A_{42} & 0 & A_{44} & A_{45} & A_{46} \\
0 & A_{52} & 0 & A_{54} & A_{55} & A_{56} \\
0 & A_{62} & A_{63} & A_{64} & A_{65} & A_{66}
\end{bmatrix}
\begin{bmatrix}
u_1 \\ v_1 \\ p_1 \\ u_2 \\ v_2 \\ p_2
\end{bmatrix}
= \omega
\begin{bmatrix}
u_1 \\ v_1 \\ p_1 \\ u_2 \\ v_2 \\ p_2
\end{bmatrix}
$$

where,

$$A_{11} = \overline{U_{11}^{(1)}}k \tag{C.7}$$

$$A_{12} = i\left(\beta y - \left(\overline{U_{y11}^{(1)}} + \overline{f_{11}^{\times}}\right)\right) \tag{C.8}$$

$$A_{13} = \frac{1}{\rho_{\times}}k \tag{C.9}$$

$$A_{14} = \overline{U_{21}^{(1)}}k \tag{C.10}$$

$$A_{15} = -i\left(\overline{U_{y21}^{(1)}} + \overline{f_{21}^{\times}}\right) \tag{C.11}$$

$$A_{21} = -i\beta y \tag{C.12}$$

$$A_{22} = \overline{U_{11}^{(1)}}k \tag{C.13}$$

$$A_{23} = -\frac{i}{\rho_{\times}}\frac{\partial}{\partial y} \tag{C.14}$$

$$A_{25} = \overline{U_{21}^{(1)}}k \tag{C.15}$$

$$A_{31} = c_1^2 \rho_{\times} k \tag{C.16}$$

$$A_{32} = -i\rho_{\times}\left(g\left(\overline{H_{y11}^{(1)}} + \overline{H_{y11}^{(2)}}\right) + c_1^2\frac{\partial}{\partial y}\right) \tag{C.17}$$

$$A_{33} = \left(\overline{U_{11}^{(1)}} + \overline{U_{11}^{(2)}}\right)k \tag{C.18}$$

$$A_{35} = -ig\rho_{\times}\left(\overline{H_{y21}^{(1)}} + \overline{H_{y21}^{(2)}}\right) \tag{C.19}$$

$$A_{36} = (\overline{U_{21}^{(1)}} - \overline{U_{21}^{(2)}})k \tag{C.20}$$

$$A_{41} = \overline{U_{12}^{(1)}}k \tag{C.21}$$

$$A_{42} = -i(\overline{U_{y12}^{(1)}} + \overline{f_{12}^{\sim}}) \tag{C.22}$$

$$A_{44} = \overline{U_{22}^{(1)}}k \tag{C.23}$$

$$A_{45} = i(\beta y - (\overline{U_{y22}^{(1)}} + \overline{f_{22}^{\sim}})) \tag{C.24}$$

$$A_{46} = \frac{1}{\rho_\times}k \tag{C.25}$$

$$A_{52} = \overline{U_{12}^{(1)}}k \tag{C.26}$$

$$A_{54} = -i\beta y \tag{C.27}$$

$$A_{55} = \overline{U_{22}^{(1)}}k \tag{C.28}$$

$$A_{56} = -\frac{i}{\rho_\times}\frac{\partial}{\partial y} \tag{C.29}$$

$$A_{62} = -ig\rho_\times\left(\overline{H_{y12}^{(1)}} + \overline{H_{y12}^{(2)}}\right) \tag{C.30}$$

$$A_{63} = (\overline{U_{12}^{(1)}} + \overline{U_{12}^{(2)}})k \tag{C.31}$$

$$A_{64} = c_2^2\rho_\times k \tag{C.32}$$

$$A_{65} = -i\rho_\times\left(g\left(\overline{H_{y22}^{(1)}} + \overline{H_{y22}^{(2)}}\right) + c_2^2(y)\frac{\partial}{\partial y}\right) \tag{C.33}$$

$$A_{66} = (\overline{U_{22}^{(1)}} + \overline{U_{22}^{(2)}})k \tag{C.34}$$

D N^2 FORMULATION

The buoyancy frequency $N^2(y, z)$ in equation (A.1) is computed from the integrating the thermal wind equation:

$$N_G^2(y, z) = N_o^2(z) - \int_{Y_S}^{Y_N} U_{zz}(y, z) dy \qquad (\text{D.1})$$

where N_G is the geostrophically balanced buoyancy frequency, Y_S is the southern boundary, Y_N is the northern boundary, $U(y, z)$ is the mean background zonal velocity and N_o is some initial buoyancy frequency. N_o^2 is determined such that the square of the differences between N_G^2 and the square of the buoyancy frequency determined from the model salinity and temperature, N^2, are minimized. The integral

$$\int_{Y_S}^{Y_N} \left(N_G^2 - N^2 \right)^2 dy \qquad (\text{D.2})$$

is thus minimized with respect to N_o^2 to obtain a least-squares estimate of N_o^2.

E QUASI-GEOSTROPHIC PROJECTION MODEL

Although the quasi-geostrophic (QG) assumptions do not apply at the equator, they do provide useful description of the critical surfaces at low latitudes. In this appendix, the QG equations are linearized about a mean background current and then projected on to the baroclinic eigenfunction in a manner similar to that described in section 4.2. Here we examine the two-mode projection model.

The QG equations in a continuously stratified fluid are:

$$\left(\frac{\partial}{\partial t} + \frac{\partial \phi}{\partial x}\frac{\partial}{\partial y} - \frac{\partial \phi}{\partial y}\frac{\partial}{\partial x}\right)\left[\left(\frac{\partial^2}{\partial x^2} + \frac{\partial^2}{\partial y^2}\right)\phi + \frac{\partial}{\partial z}\left(\frac{f_0^2}{N^2}\frac{\partial \phi}{\partial z}\right) + \beta y\right] = 0 \qquad \text{(E.1)}$$

where,

$$u = -\frac{\partial \phi}{\partial y} \qquad \text{(E.2)}$$

$$v = \frac{\partial \phi}{\partial x} \qquad \text{(E.3)}$$

$$p = \rho_0 f_0 \phi \qquad \text{(E.4)}$$

If the form of ϕ is linearized about a mean $\Phi(y)$ and assumed to have a dependance on x and t of the form $e^{I(kx-\omega t)}$, then equation (E.1) becomes:

$$(U_0(y) - c)\left[\frac{\partial^2}{\partial y^2} - k^2 + \frac{\partial}{\partial z}\left(\frac{f_0^2}{N^2}\frac{\partial}{\partial z}\right)\right]\phi(y, z) +$$

$$\left[\beta - \frac{\partial^2}{\partial y^2}U_0(y, z) - \frac{\partial}{\partial z}\left(\frac{f_0^2}{N^2}\frac{\partial U_0(y, z)}{\partial z}\right)\right]\phi(y, z) = 0 \qquad \text{(E.5)}$$

where ϕ is now dependent only on y and z with $U_0(y) = -\frac{\partial \Phi}{\partial y}$ and $c = \frac{\omega}{k}$.

$$\left(\overline{U_{11}^{(1)}} + \overline{U_{21}^{(1)}} - c \right) \left(\frac{\partial^2}{\partial y^2} - k^2 - \frac{f_0^2}{c_1^2} \right) \phi_1 +$$

$$\left[\beta - \frac{f_0 g}{c_1^2} \left(\overline{H_{y11}^{(1)}} + \overline{H_{y21}^{(1)}} \right) - \frac{\partial^2}{\partial y^2} \left(\overline{U_{11}^{(1)}} + \overline{U_{21}^{(1)}} \right) \right] \phi_1 = 0 \qquad (E.9)$$

In regions where there are critical layers, $\overline{U_{11}^{(1)}} + \overline{U_{21}^{(1)}} = c$. Similarly, the coupled equations representing the second vertical mode produce a critical layer defined by, $\overline{U_{22}^{(1)}} + \overline{U_{12}^{(1)}} = c$. This simplified description of the critical layers in the fluid provides useful insight into the maximum phase speed of the instabilities in a two-mode projection model.